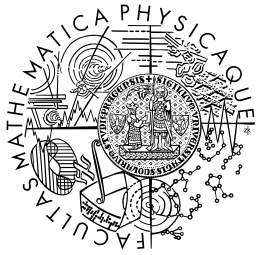

FACULTY
OF MATHEMATICS
AND PHYSICS
Charles University

MASTER THESIS

Zuzana Gruberová

Study of the τ lepton decays at the Belle II experiment

Institute of Particle and Nuclear Physics

Supervisor of the master thesis: prof. RNDr. Zdeněk Doležal, Dr.
Study programme: Physics
Study branch: Nuclear and Subnuclear Physics

Prague 2021

I declare that I carried out this master thesis independently, and only with the cited sources, literature and other professional sources. It has not been used to obtain another or the same degree.

I understand that my work relates to the rights and obligations under the Act No. 121/2000 Sb., the Copyright Act, as amended, in particular the fact that the Charles University has the right to conclude a license agreement on the use of this work as a school work pursuant to Section 60 subsection 1 of the Copyright Act.

In ..... date ....

Author's signature

I wish to express my greatest thanks to Petar Radoš and Ami Rostomyan who supervised my work, for motivating and guiding my study, for their support and patience during our discussions, and for thoroughly checking this thesis. I am sincerely grateful for the opportunity to work with them.

I would like to thank the DESY Tau Group, the Belle II Tau Physics Group and the Belle II Neutrals Performance Group for their collaboration and feedback.

I thank Zdeněk Doležal for introducing me to the Belle II experiment and for enabling my collaboration with DESY, and I thank the Prague Belle II group for supporting me during my master studies.

I take this opportunity to thank my family for their invaluable influence on my personality, for their patience during my studies and for supporting me in my decisions.

I would like to thank my friends Lucka and Pavel with whom I shared the master studies' struggles and who helped me with managing the organizational necessities.

Last but not least, my thanks go to Ni who made sure I made the most of my time.

Title: Study of the τ lepton decays at the Belle II experiment

Author: Zuzana Gruberová

Institute: Institute of Particle and Nuclear Physics

Supervisor: prof. RNDr. Zdeněk Doležal, Dr., Institute of Particle and Nuclear Physics

Consultant: Dr. Petar Radoš, DESY, Hamburg

Abstract: This master thesis describes the measurement of the π^0 reconstruction efficiency correction using τ-pair events from the Belle II experiment. The review part of the thesis begins with an overview of the Standard Model and the Belle II experiment, its detector system and the simulation software. This is followed by the description the τ-pair events and the method used for measuring the π^0 reconstruction efficiency correction. The central part focuses on the event selection and the extraction of the signal yields. The results present the measured values of the average and momentum dependent π^0 reconstruction efficiency correction, an improved π^0 selection optimized for τ-lepton analyses, and a dedicated study on photon timing selection requirements.

Keywords: particle physics, Belle II, data analysis, τ leptons, π^0 reconstruction efficiency, π^0 selection

Contents

Introduction

Particle physics studies the fundamental constituents of the world around us — the elementary particles, their properties and their interactions. The current theory describing elementary particles and fundamental forces — the Standard Model — has predicted various properties and relations that have been confirmed, yet many observed phenomena remain unexplained and improving our knowledge about the laws that rule the processes on the fundamental scale is what intrigues physicists all over the world.

Particle interactions are predominantly studied in particle accelerator experiments. Accelerated particles collide at high energies and produce new particles that can exhibit rare decays. In order to observe rare processes and measure particle properties with high precision, large amounts of data need to be collected.

Particle physics experiments are currently being conducted by various institutions in different countries. Belle II is one such experiment, built at the High Energy Accelerator Research Organisation (KEK) in Tsukuba, Japan. Its predecessor experiment, Belle, contributed to many important discoveries, the greatest of which was the confirmation of the CP asymmetries predicted in B meson decays. This experimental result was explicitly recognized in the 2008 Physics Nobel Prize [1, 2].

Belle II was designed to search for physics beyond the Standard Model in decays of B, D mesons and τ leptons. The Belle II detector collects a great amount of data from the particle collisions which is subsequently processed and analyzed.

Most of such data analyses rely on computer simulations which are designed to reproduce the known or predicted particles' behaviour as well as the detector performance. Real measured data is then compared with simulated data and the resultant information is used to examine the theory behind the particle decays and interactions, or to better understand and improve the detector behaviour and analytical methods.

The finite resolution of the detectors as well as the limits of the computer simulations introduce various systematic errors and biases which then impact the final physics results. In order to obtain measurements with the highest possible accuracy, these effects need to be studied and appropriate corrections must be applied during the physics analyses.

One such effect is the particle reconstruction efficiency, which describes the difference between the number of produced and reconstructed particles. This efficiency can be different in real data and in simulation, and the difference must be compensated for by using an appropriate correction factor.

The subject of this master thesis was the study of τ lepton decays at the Belle II experiment, in particular the decays involving π^0 mesons. The main goal of the study was to determine the π^0 reconstruction efficiency correction factor between the data and Monte Carlo simulation for the Belle II physics analyses. The correction factor was determined using the double ratio method described

further in this thesis, and this approach was inspired by a similar study done at the BaBar experiment [3].

The review part of this thesis summarizes the basic properties of the studied particles, gives an overview of the Belle II experiment and its physics goals and describes the Belle II detector systems, as well as the simulation software.

The next sections focus on τ physics at Belle II, first describe the τ event characteristics and then explain the idea behind the method used for measuring the π^0 efficiency correction.

The central part of this thesis describes in detail the analysis setup, the selection of the signal sample and the extraction of the signal yields.

The results on the measurement of the π^0 efficiency corrections and the associated uncertainties are then presented. The results also contain an optimization of an improved π^0 selection, and a dedicated study on photon timing selection requirements.

The discussion gives a wider context to the obtained results and proposes the next steps for this study.

The attachments contain references to physics studies relevant to this analysis, as well as additional materials.

The central and results sections of this thesis (from Chapter 6 onwards) contain several studies for which the author of this thesis was the lead analyser.

1. Physics overview

The Standard Model (SM) [4, 5, 6, 7] is a theoretical model which describes the elementary particles and their interactions. It has been successful in explaining various observed phenomena and it is currently the best description of our world at the most fundamental level. However, it is known that the SM is incomplete. From the four fundamental forces it accounts for only three of them — it does not include any description of gravity. The SM is also unable to fully explain CP violation, which is believed to be responsible for the observed asymmetry between matter and anti-matter in our present universe, and there are even more yet unexplained phenomena such as dark matter or dark energy. Many approaches tried to extend the SM and build one complete theory which would describe every physical aspect of our universe but no successful model has so far been developed.

The first section of this chapter reviews the SM of particles and interactions, while the second section focuses on the properties of τ leptons.

1.1 The Standard Model

The SM is a quantum theory and it describes particles as excitations of quantum fields. These particles can be divided into two groups, fermions and bosons. Fermions are the matter constituents, they carry half-integer spin and obey Fermi-Dirac statistics. Bosons have integer spin, follow Bose-Einstein statistics and are responsible for the interactions between fermions. The three interactions embedded within the SM are the electromagnetic force mediated by photons (γ), the weak force carried by Z, W^+ and W^- bosons, and the strong force represented by gluons. The SM contains also the Higgs boson, which is responsible for giving masses to the elementary particles through the so called Higgs mechanism.

The fermions can be further classified as quarks (q) and leptons (ℓ). Quarks are charged particles with non-integer charges which can only exist in bound states called hadrons (h). Known bound states of quarks are of two types: mesons, confined states of one quark and one anti-quark, and baryons, bound states of three quarks. There are six distinct flavours of quarks (up (u), down (d), charm (c), strange (s), top (t), bottom (b)) and they differ e.g. by mass. Quarks can interact via all the fundamental forces unlike leptons, which do not experience the strong force. Leptons are present in three different flavours; there are three negatively charged leptons (electron (e), muon (μ), tau (τ)) and three neutral leptons, each paired with a charged lepton, called neutrinos (ν).

Fig. 1.1 summarizes the SM particles and their fundamental properties, and visualizes the possible interactions between them.

Fermions can be grouped into three generations. The first generation particles are up and down quarks, electron and electron neutrino. These particles are stable and build the vast majority of all the visible matter. The second and third generation charged fermions are heavier and can decay into lighter particles via the weak force.

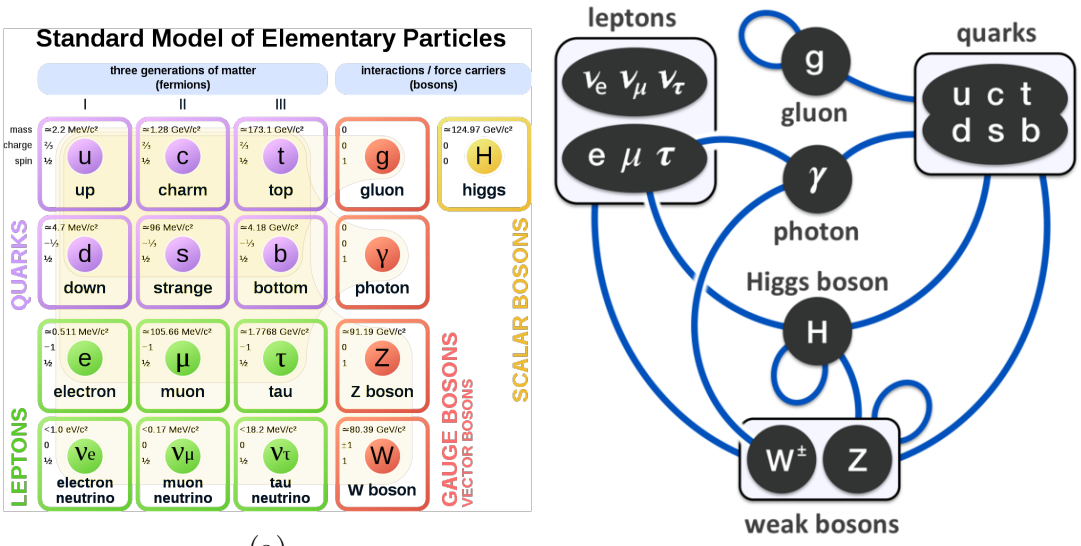

Figure 1.1: *The Standard Model.* The SM consists of 12 fermions and 5 bosons. Picture (a) shows the elementary particles grouped by their fundamental physical properties. The lines in the picture (b) represent possible interactions between the SM particles.[8, 9]

The SM gives rules for allowed decays and conversion between the particles. Apart from kinematic restrictions, some decays are forbidden or heavily suppressed by conservation laws for quantum numbers. The probability of a certain decay process is called a branching ratio (BR). Decays of elementary particles are of great interest and precise measurements of BRs and particle lifetimes are valuable checks of theoretical models.

1.2 τ leptons

The τ leptons are third-generation charged leptons which makes them the heaviest known leptons with mass (1776.86 ± 0.12) MeV [10]. The lifetimes of τ leptons is $(2.903 \pm 0.005) \times 10^{-13}$ s [10] and they can decay not only into lighter leptons, e and μ, but also into light mesons such as pions (π) and kaons (K).

The chart in Fig. 1.3 shows the most dominant decay modes, with all possible decay modes listed in Fig. 1.2. In total, τ lepton decays are mostly semileptonic, the purely leptonic decays account for only around 35 % of the total decay modes. The semileptonic τ decays contain one neutrino in the final state (e.g. $\tau \to \pi\nu_\tau$, etc.), while the leptonic decays contain two neutrinos ($\tau^- \to e^-\bar{\nu}_e\nu_\tau$ or $\tau^- \to \mu\bar{\nu}_\mu\nu_\tau$). The decay of a τ lepton yields from one to five charged tracks. Depending on the number of charged tracks τ decays are thus also called 1-prong, 3-prong or 5-prong decays. τ lepton decay modes can also involve neutral pions (π^0), the most dominant one being $\tau \to \pi\pi^0\nu_\tau$ with a BR of around 25 %.

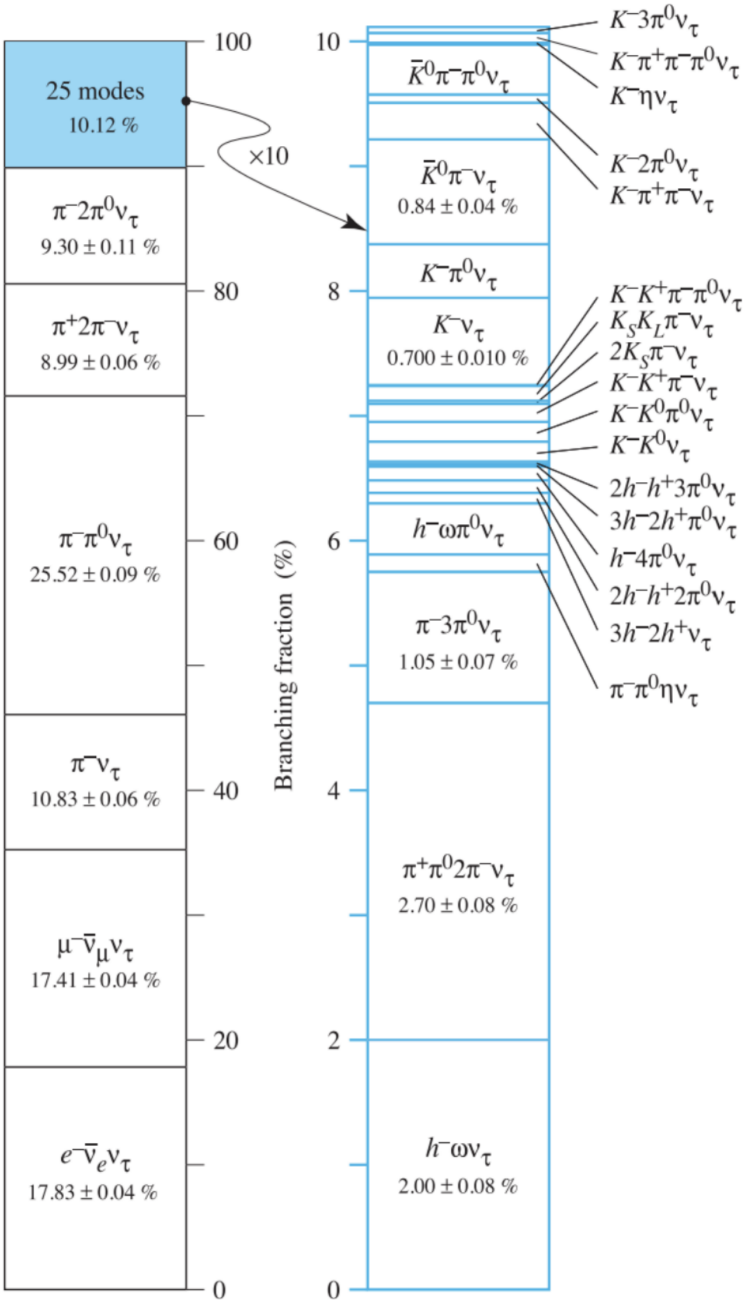

Figure 1.2: *τ decay modes.* This picture lists all τ lepton decay modes with their respective branching fractions. [10]

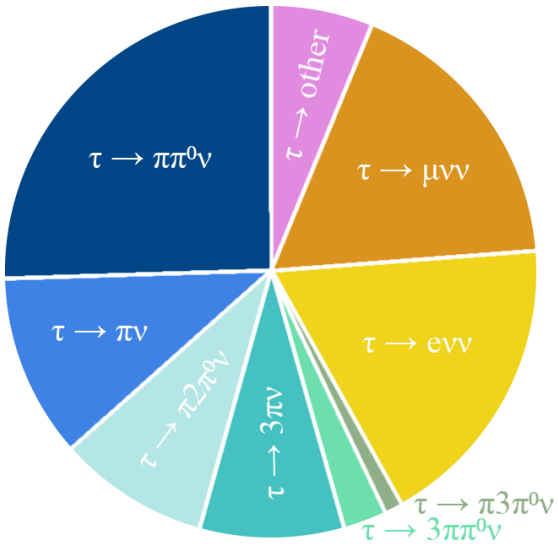

Figure 1.3: *Common τ lepton decay modes.* The main interest for this study is the decay mode $\tau \to 3\pi\pi^0\nu_\tau$ with BR $(2.74 \pm 0.07)\%$. [11]

1.2.1 Decays involving π^0

The study presented in this thesis focuses on 3-prong τ decay with a neutral pion in the final state, $\tau \to 3\pi\pi^0\nu_\tau$ that has a BR of $(2.74 \pm 0.07)\%$.

This decay mode is analysed using the e^+e^- annihilation data from Belle II where the τ leptons are produced in pairs, $e^+e^- \to \tau^+\tau^-$. The process is shown in Fig. 1.4.

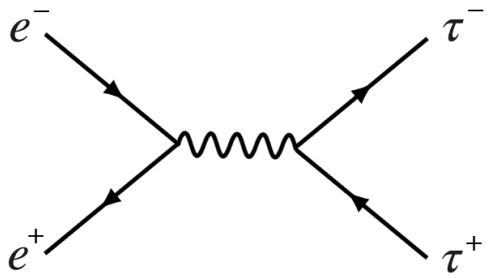

Figure 1.4: *τ-pair production.* Feynman diagram of the annihilation process $e^+e^- \to \tau^+\tau^-$. [11]

In order to correctly classify an observed process it is essential to measure, reconstruct and identify all detectable final state particles. Missing a π^0, or reconstructing a fake π^0 can cause mixing of different decay modes and thus lead to incorrect estimates of measured signal yields. In addition, π^0s are light mesons and they are created in many different processes, therefore, understanding their behaviour is of great importance in particle physics data analyses.

The main goal of this study is to measure the π^0 reconstruction efficiency and provide the π^0 efficiency correction to compensate the difference in π^0 reconstruction in data and simulation. This correction factor is applicable not only in τ physics studies, but also in B- and D-meson-decay (heavy particles containing

a charm and bottom quark, respectively) analyses whose final states involve π^0 mesons. Another aim of this study is to improve π^0 and photon selections to achieve high purity for τ decays.

Detailed description of π^0 reconstruction efficiency is given in Chapter 5, the optimization of the π^0 and photon selection is presented in Chapter 9.

2. Belle II experiment

Belle II is a particle physics experiment designed to search for physics beyond the SM, so-called New Physcis (NP), in decays of B, D mesons and τ leptons. In spring 2018 Belle II observed its first collisions at SuperKEKB, an energy asymmetric e^+e^- collider. Belle II is an upgrade of the previous programme, the Belle experiment [14], which ran from 1999 to 2010. Its main goal is to continue measurements with high precision and also to search for NP phenomena.

The aim of this chapter is to provide more details about the Belle II experiment and its detector systems. The first two sections provide an overview of the SuperKEKB collider and Belle II detector. The last section summarises the status of data taking at Belle II.

2.1 SuperKEKB

The SuperKEKB collider is located in Tsukuba, Japan, and is operated by the High Energy Accelerator Research Organization (KEK). It accelerates e^+ and e^- beams along its 3 km circumference ring, collides them at $\sqrt{s} = 10.58$ GeV and the collisions are then recorded by the Belle II detector. The collider is asymmetric in beam energies, the energy is 7 GeV for electrons and 4 GeV for positrons, which leads to a boost of the collisions' center-of-mass system with respect to the laboratory system.

A layout of the SuperKEKB accelerator is shown in Fig. 2.1. It consists of a linear accelerator which produces the e^+ and e^- beams and injects them into the high energy storage ring (HER) and low energy storage ring (LER).

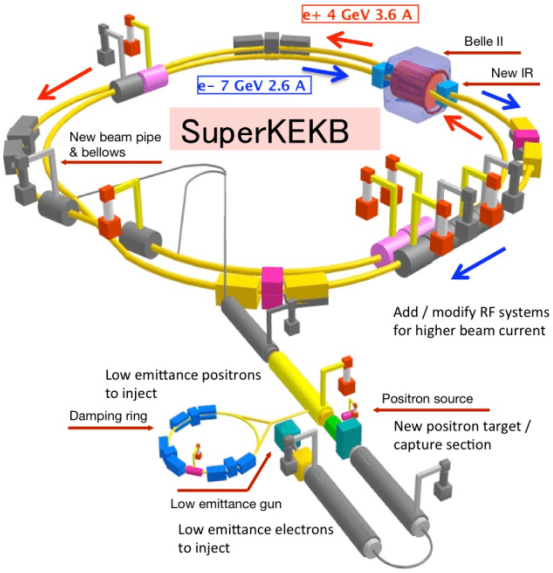

Figure 2.1: *The SuperKEKB accelerator.* This picture shows the SuperKEKB accelerator and its main components, including the Belle II detector.[13]

Compared to KEKB, the predecessor collider, the beam current in the SuperKEKB storage rings is about twice higher, and an improved nano-beam scheme [15] of bunch crossing at the interaction region inside Belle II is employed. Thanks to these two factors SuperKEKB is expected to provide very high luminosity and currently holds the world record for the highest instantaneous luminosity measured at a particle collider, $2.4 \times 10^{34}\text{cm}^{-2}\text{s}^{-1}$ [16]. The design luminosity of $8 \times 10^{35}\text{cm}^{-2}\text{s}^{-1}$, which is 40 times higher than what was achieved with KEKB, is expected to be reached in a few years.

2.2 Belle II detector

The main concept of the Belle II detector remains the same as in the Belle experiment. When two particle bunches with asymmetric energies collide, the centre of mass moves in the direction of the higher energy electron beam. Therefore, most of the interaction products fly in the same forward direction and thus the layout of the detector is asymmetric as well.

Along with the upgrade of the accelerator, the Belle II detector also features many adjustments and improvements compared to the Belle detector. The following subsection briefly describes each of the individual subdetectors of the Belle II detector system.

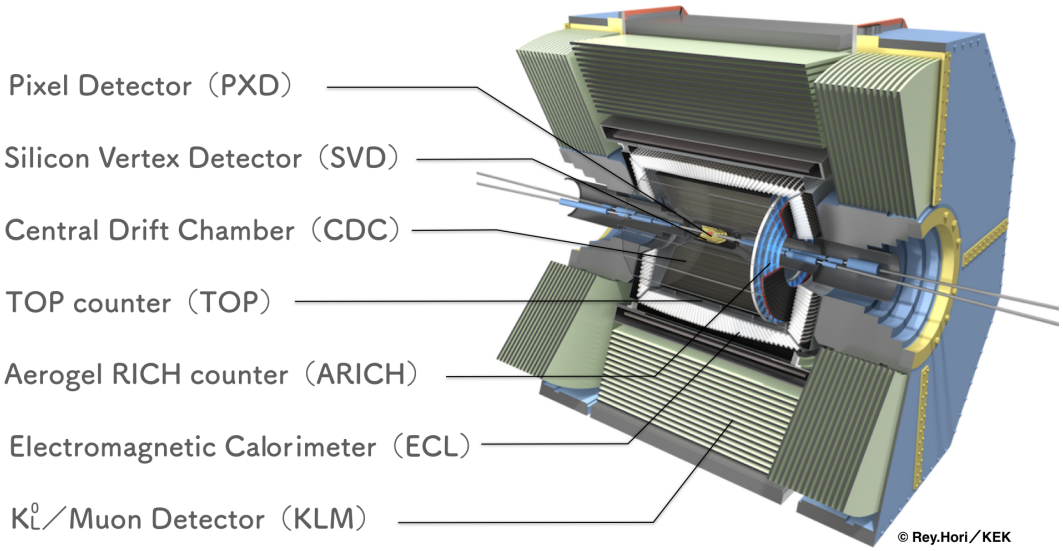

Figure 2.2: *3D model of the Belle II detector.* This figure shows the major Belle II subdetectors. The tracking system is comprised of the PXD, SVD, and CDC; TOP and ARICH are responsible for particle identification. The crystals of the ECL detect neutral particles and measure the energy of electromagnetic particles. The KLM surrounds the whole system and detects muons and kaons. The forward side of Belle II is to the right in the picture. [18]

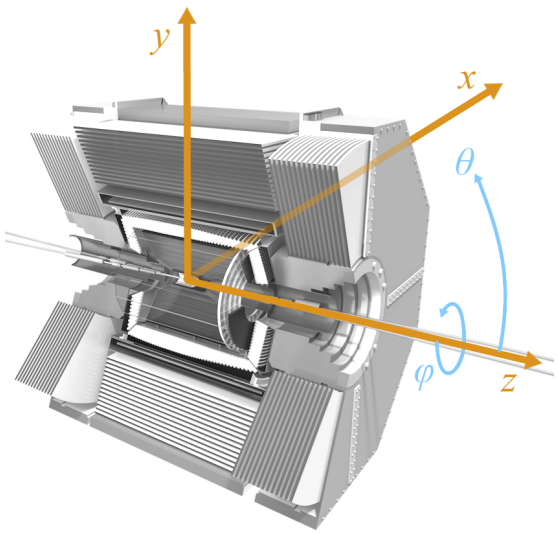

Figure 2.3: *Coordinate system of Belle II.* The x-axis is horizontal and points outside of the accelerator tunnel, the y-axis is vertical pointing upward, the z-axis is the Belle II solenoid axis, which is a bisector of the two beams; poitning roughly in the direction of electron beam. The φ angle is the azimuthal angle around the z-axis, $\varphi = 0$ is defined for $(x, y, z) = (1, 0, 0)$. The θ angle is the polar angle with respect to the z-axis, $\theta = 0$ is defined for $(x, y, z) = (0, 0, 1)$. [11]

2.2.1 Subdetectors

The Belle II detector consists of various detector subsystems layered around the interaction region. A 3D model of the Belle II detector is shown in Fig. 2.2. Fig. 2.3 describes the coordinate system of the Belle II detector.

Each of the subdetectors has a different structure and the combined information from all of them is used to reconstruct the measured events. A scheme of a typical particle detector layers is shown in Fig.2.4, including also the characteristic signatures of the most commonly detected particles. Belle II has its own specific detector system and its components are described in this subsection. [12, 18]

PXD: The innermost part of the Belle II detector is placed 14 mm from the interaction point and allows for detecting low transverse momentum particles, from p_T as low as 6 MeV. Because of the extreme luminosity, large beam background is expected, therefore, high-granularity pixel detectors (PXD) are required in the innermost layers. The PXD sensors are based on the depleted field effect transistor (DEPFET) technology and surround the beam pipe at 14 and 22 mm radii.

SVD: The next tracking detector subsystem consists of four layers of the strip vertex detectors (SVD) which are placed between 38 and 140 mm from the beam pipe. The SVD is built from double-sided silicon strip sensors. The barrel part consists of rectangular sensors in a windmill structure while the forward region is covered by trapezoidal-shaped sensors slated to form a lantern-shaped cap.

CDC: The central drift chamber (CDC) is the largest tracking detector - it occupies the volume between 160 and 1130 mm from the beampipe and its length is 2.4 m. CDC provides high precision track and momentum measurements that,

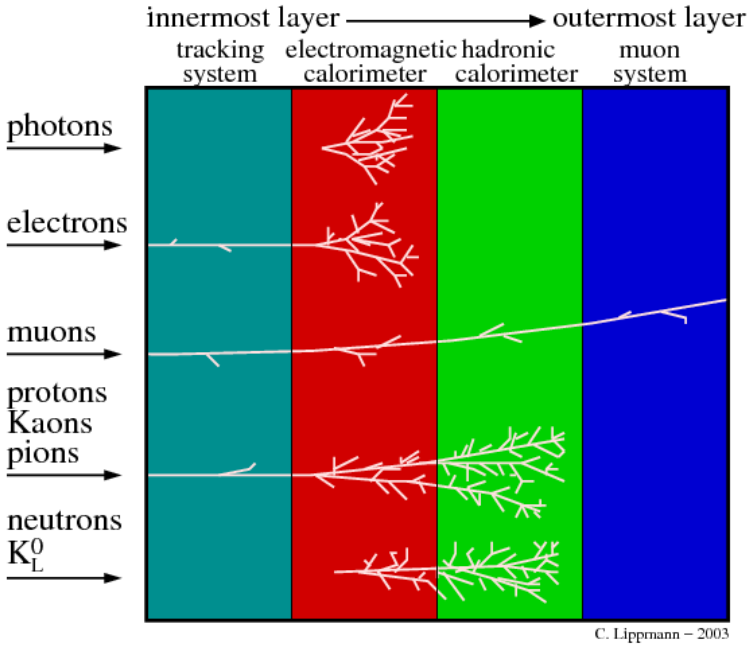

Figure 2.4: *Particle signatures in a detector.* The scheme shows components of a "traditional" particle physics detector. Each particle type has its own unique signature in the detector. [19]

combined with the data from the PXD and SVD detectors, allows for precise reconstruction of charged particle tracks. The CDC is also able to measure particles' energy losses and therefore contributes to particle identification. The CDC consists of sense and field wires parallel to the beam direction. The sense wires are made of tungsten and collect the signal from passing particles, the field wires are made of aluminium, surround the sense wires and create an accelerating electric field. The whole detector chamber is filled with He-H_2C_6 gas. The CDC is also important for the triggering system.

TOP and ARICH: The particle identification (PID) subsystem comprises the time of propagation counters (TOP) in the barrel part and aerogel ring-imaging Cherenkov detector counters (ARICH) covering the endcap. Cherenkov photons are created in aerogel inside the TOP by incoming charged particle and are guided into the quartz radiator and subsequently detected by photomultipliers at the end of crystal bars. Cherenkov ring imagess are then reconstructed using two spatial coordinates and very precise timing. The ARICH counter is formed by aerogel layer, where the Cherenkov photons are created, an expansion volume to allow photons to form rings on the detector surface, and an array of position-sensitive photon detectors. These two particle identification detectors are designed to distinguish between pions and kaons, and low energy pions, muons and electrons.

ECL: The electromagnetic calorimeter (ECL) is used to measure the energy of electromagnetic particles, detect neutral particles and measure the luminosity. It consists of a 3 m long barrel section and annular endcaps, formed by CsI(Tl) crystals. Energy deposited by incoming particles is then converted into photons and collected by photodiodes at the end of each crystal. The ECL detector also plays an important role in the triggering system.

KLM: The outermost detector subsystem of Belle II is the K_L and muon detector (KLM). It consists of alternating layers of iron plates and sensitive detector elements and is located outside the superconducting solenoid. Charged particles are detected in the KLM by glass electrode resistive plate chambers (RPC), which are interleaved between iron plates. RPCs collect the products of particle showers created in iron by kaons and muons.

2.2.2 Beam background

The high design luminosity of SuperKEKB results in challenging levels of beam-induced backgrounds around the interaction area. The five main beam background sources that are present at SuperKEKB are listed below and pictured in Fig. 2.5.

- The Touschek effect is a scattering process inside the bunch where energies of individual particles depart from the nominal energy of the bunch due to Coulomb scattering. This effect is enhanced because of the high compression of bunches in the nano-beam scheme.
- Beam-gas scattering is the scattering of beam particles on residual gas molecules inside the beam pipe. It can occur either due to the change of direction of the beam particle caused by Coulomb scattering, or via bremsstrahlung scattering, which reduces particles' energy. The rate of beam-gas scattering is proportional to the beam current, which is nearly two times higher than at KEKB, and to vacuum pressure, which is the same at SuperKEKB as it was for KEKB.
- Synchrotron radiation (SR) is emitted from the beam and its power is proportional to beam energy squared and magnetic field strength squared. Therefore, most of this background originates in the HER.
- The radiative Bhabha process produces photons which interact with the iron of the accelerator magnets and create gamma rays and neutrons. The number of these neutrons is proportional to luminosity. Neutrons create the main background of KLM measurements, while low energy gamma rays are a significant source of background in the CDC.
- Low momentum e^-e^+ pairs produced via the two-photon process $e^-e^+ \to e^-e^-e^+e^+$ are an important luminosity-related background radiation. These pairs can spiral around the magnetic field lines and leave multiple hits in the inner (vertex) detectors. In addition, the primary particles can lose a large amount of energy or scatter at large angles and can be subsequently lost inside the inner detector.

Injection background appears when more particles are injected into the accelerator ring: circulating bunches get perturbed and a higher background rate is observed for a few milliseconds. A trigger veto is applied after each injection to avoid PXD readout saturation. [12]

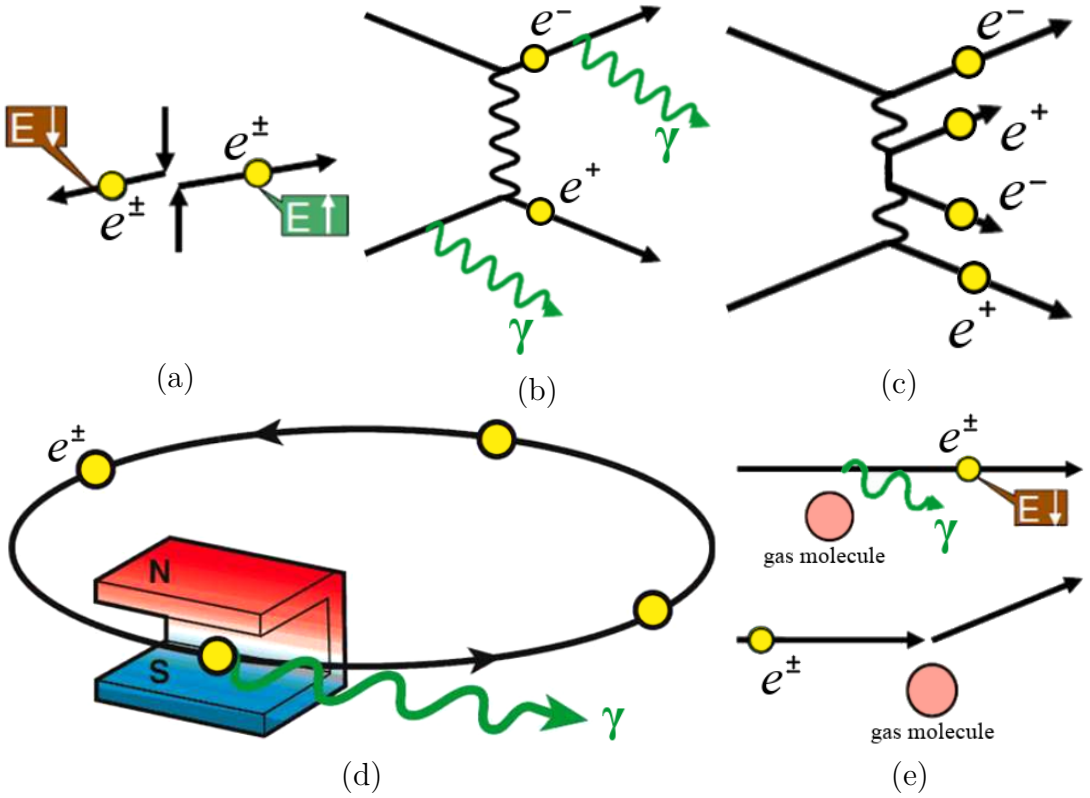

Figure 2.5: *Belle II background processes.* The pictures in this figure illustrate the five main background processes present at SuperKEKB: (a) the Touschek effect, (b) radiative Bhabha scattering, (c) two-photon process, (d) synchrotron radiation and (e) beam-gas scattering. [11]

2.2.3 Trigger system

The event rate at Belle II exceeds the capacities of the data collection network and data storage system of the Belle II experiment. The trigger system is responsible for identifying the subset of events that contain the most interesting physics processes for further analysis, the decision about keeping an event is made in less than 5µs. This is necessary because the data acquisition (DAQ) system has a limit rate around 30 kHz and therefore is not able to process all of the events. The requirements for the trigger is high efficiency for physics processes, timing precision better than 10 ns, and minimum two-event separation of 200 ns.

The Belle II trigger consists of two levels: the hardware based Level 1 trigger (L1) [20] and software based high level trigger (HLT) [21].

The L1 trigger menu was designed to cover a broad range of detector signatures and is comprised of two primary components: a CDC track trigger and an ECL trigger.

Track reconstruction by the CDC trigger is based on so-called track segments, which are produced by the track segment finder in each of the nine super layers (SLs) of the CDC. 2D tracks are searched for in (r, φ) space by combining the track segments from a subset of the SLs. Tracks that pass through all axial SLs and reach the barrel region are referred to as "full tracks".

The ECL can generate fast trigger signals that can provide a highly efficient trigger for detector signatures containing both neutral and charged particles. The trigger cell, which is composed of 4x4 CsI(Tl) scintillation crystals, is a basic unit of the ECL trigger system. Two complimentary trigger schemes are taken into account: a total energy trigger and an isolated cluster counting trigger. In addition, dedicated triggers have been developed to specifically target low-multiplicity signatures, and these triggers are also efficient for detecting τ-pair events. The ECL trigger system can also identify Bhabha scattering events.

The CDC and ECL information and sub-trigger results are sent to global reconstruction logic (GRL) where a low-level reconstruction is performed by combining this information. The reconstruction results are then sent to global decision logic (GDL) system, where the final decision is made. Events which pass the L1 trigger are evaluated again by HLT which uses more advanced decision algorithms based on the information from the Belle II subdetectors, and its aim is to reduce the online event rates to 10 kHz so that the data can be stored offline. [12] [17]

Many trigger lines exist and there are several new information paths that were not present in the previous Belle trigger system. Triggers are defined in terms of trigger bits which comprise a set of conditions that must be fulfilled to fire the trigger. In the analysis presented in this thesis the following trigger bits were used, because they perform with high efficiency with respect to τ-pair events:

- *fff* – Number of full 2D tracks ≥ 3 *and* no injection veto.
- *ffo* – Number of full 2D tracks ≥ 2 *and* CDC opening angle $> 90°$ *and* no Bhabha veto *and* no injection veto.
- *lml0* – Number of ECL clusters ≥ 3 *and* at least one ECL cluster energy ≥ 300 MeV *and* no Bhabha veto *and* no injection veto.

fff and *ffo* are CDC based triggers, while *lml0* is ECL based and was designed to have high efficiency for low-multiplicity events such as tau-pair events. CDC opening angle is the angle between two tracks and the condition requires the angle to be $> 90°$ for at least one pair of tracks. Bhabha veto is a set of conditions that characterize the Bhabha scattering, which is a background process with high cross section and such events are being rejected.

2.3 Data taking

The first data taken with Belle II were recorded in the first half of 2018 during the detector commissioning period (Phase 2). Collisions with the full Belle II detector started in March 2019 (Phase 3). The data taking in Phase 3 is divided into shorter periods called experiments (Exp) which are numbered consecutively and sometimes further divided into so called buckets.

In 2020, the world record for the highest instantaneous luminosity was set by SuperKEKB at $2.4 \times 10^{34}\text{cm}^{-2}\text{s}^{-1}$ [16]. Fig. 2.6 displays the total recorded luminosity from early 2019 to May 2021. The goal of the Belle II experiment is

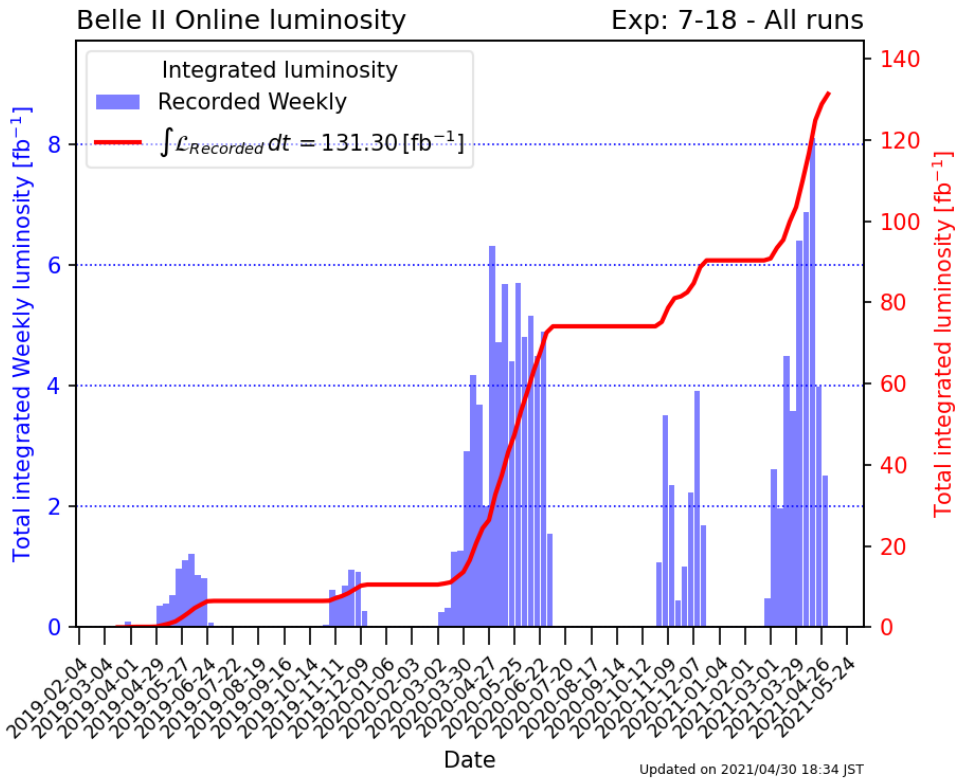

Figure 2.6: *Belle II luminosity.* The plot shows total luminosity recorded at Belle II from early 2019. [22]

to collect a large data set at the $\Upsilon(4S)$ resonance corresponding to an integrated luminosity of $500 - 700$ fb^{-1} by summer 2022 and 50ab^{-1} by 2031. Apart from this data Belle II also records off-resonance collisions.

In this analysis, data from Exp 7, 8, 10 and 12 were studied, with their respective integrated luminosities listed in Tab. 2.1. The total integrated luminosity for the used data is 62.79 fb^{-1}, unless stated otherwise.

Table 2.1: Used data samples.

Experiment	Bucket	$\int \mathcal{L}$ dt [pb^{-1}]
Exp7		425.5
Exp8		4597.4
Exp10		3741.3
Exp12	9	2768.7
	10	10361.1
	11	12687.1
	13	5055.1
	14	9986.9
	15	13171.6

3. Monte Carlo simulation

Monte Carlo (MC) simulation is essential in particle physics analyses to understand the detector response for different physics processes. The goal is to comprehend the particle properties and behaviour as well as the detector performance and produce simulated data which can be analysed and processed in the same way as real data. One difference is that the MC samples not only have available the reconstructed objects but also the "truth" information of the original generated events.

However, the simulation will never be perfect and the resultant discrepancies between real data and simulated data need to be carefully evaluated and compensated for. Among such corrections there is for example the trigger efficiency correction, or the π^0 reconstruction efficiency correction which is the main topic of this study. The MC corrections used in this analysis are described in Chapter 6, while the measurement of the π^0 reconstruction efficiency is discussed in Chapter 5.

The following chapter provides a brief overview of the simulation process within the Belle II experiment and summarizes the MC samples used in this study.

3.1 Simulated data at Belle II

The core of the whole Belle II software is the Belle II analysis software framework (basf2) [24]. Basf2 works by processing modules in sequential order. The modules contain the reconstruction algorithms which are used to process the data. Initially, the raw data with detector information such as track hits and calorimeter energy clusters are used to reconstruct higher-level objects, like charged tracks. On the next level, these objects can be used to calculate properties of the particles, such as their four-momenta, and information about the full event, such as the total visible energy. The final objects are stored and subsequently used in the data analysis.

Simulated data are usually created in three steps. The first step is to generate the events, where the particles are created and their decays are generated based on the SM (or other models in case of searches for BSM physics) predictions. Various processes are generated by different generators. For example τ-pair events are generated with `KKMC` generator and the subsequent decay of the τ leptons is handled by `TAUOLA`. For more information about Belle II MC generators please refer to [17].

The next step is the simulation of the particle interaction with the detector. The simulation is based on the `Geant4` [23] software and it uses MC method to generate particle trajectories and energy deposits in the detector as well as the secondary particles. The geometry of the simulated detector matches exactly the real Belle II detector composition.

The simulation also comprises the detector response to the generated physical signal. This is done by simulating the physics processes in the detectors with

respect to their geometry, used electronics and also including random noise.

The output of this MC simulation chain is taken as the detector signal which is to be compared with real measured data from Belle II.

Table 3.1: MC13a samples with the corresponding cross sections and luminosities.

Processes	Cross section [nb]	Name of the production	$\int Ldt$ [fb^{-1}]
generic			
$e^+e^- \to \tau^+\tau^-$	0.919	`'taupair'`	100
$e^+e^- \to u\bar{u}$	1.61	`'uubar'`	100
$e^+e^- \to d\bar{d}$	0.4	`'ddar'`	100
$e^+e^- \to s\bar{s}$	0.38	`'ssbar'`	100
$e^+e^- \to c\bar{c}$	1.3	`'ccbar'`	100
$e^+e^- \to B\bar{B}$	1.05	`'mixed','charged'`	100
low multiplicity			
$e^+e^- \to e^+e^-\gamma$	300	`'ee', 'ee1trk'`	10
$e^+e^- \to \mu^+\mu^-\gamma$	1.148	`'mumu'`	100
$e^+e^- \to e^+e^-e^+e^-$	39.7	`'eeee'`	100
$e^+e^- \to e^+e^-\mu^+\mu^-$	18.9	`'eemumu'`	100

The MC samples were produced in an official Belle II MC campaign and they are periodically reproduced with new software releases. The MC samples used in this study are the Phase 3 run-independent MC from the 13th official production campaign (MC13a) with nominal beam background conditions (BGx1) including all decay modes (generic) and low-multiplicity processes. These MC samples produced with basf2 release 04-00-03. Tab. 3.1 lists the MC luminosity of each of the used samples together with the cross sections of the processes.

4. τ-pair events

The analysis presented in this thesis focuses on τ-pair events. The following chapter describes the production of τ leptons as they are measured by Belle II and introduces the main characteristics of τ-pair events.

Belle II is often called a "B-factory" because its designed collision energy corresponds to a high production cross section for the $\Upsilon(4S)$ resonance, which subsequently decays into B mesons. But Belle II can be called a "τ-factory" just as well because the cross section for producing a pair of τ leptons is comparable with the cross section for $\Upsilon(4S)$.

As was mentioned in the previous chapter, τ leptons can decay to one, three, or five charged particles. Events studied in the analysis presented in this thesis are 3x1-prong events, with the topology of such events in the Belle II detector depicted in Fig. 4.2.

Fig. 4.1 shows the diagram of a signal event for out analysis. We are interested in the 3-prong side, the hemisphere corresponding to this τ decay is called signal hemisphere, the other side, 1-prong decay, is tag hemisphere. In order to keep the events cleaner, we allow only purely leptonic decays on the 1-prong side.

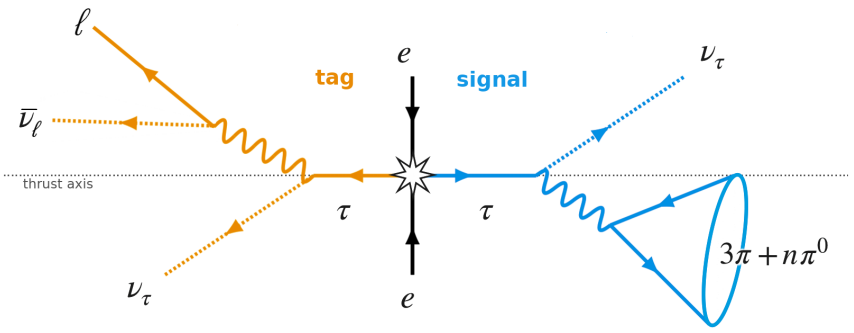

Figure 4.1: *Signal event diagram.* τ-pair events can be described in terms of the signal and tag hemispheres with respect to the two τ leptons. The signal decay mode is $\tau \to n\pi\pi^0\nu_\tau$, while the tag τ decays either into an electron or a muon. The thrust axis maximizes the momentum projection of all visible particles in the event. [11]

4.1 τ-pair production in e^+e^- annihilation process

In e^+e^- annihilation, in the center of mass system (CMS) the τ-pair events are produced back-to-back. This allows for dividing the space into two hemispheres with respect to the thust axis which corresponds to the maximal momentum projection of all visible particles. We then define the thrust value V_{thrust} as follows

$$V_{\text{thrust}} \overset{\text{max}}{=} \sum_i \frac{|\vec{p}_i^{\,\text{CMS}} \cdot \hat{n}_{\text{thrust}}|}{\sum |\vec{p}_i^{\,\text{CMS}}|}, \tag{4.1}$$

where $\vec{p}_i^{\,\mathrm{CMS}}$ is the CMS momentum of the particle and $\hat{n}_{\mathrm{thrust}}$ is the unit vector in the direction of the thrust axis. Because of the back-to-back property, thrust value is going to be high, close to 1. However, unlike in for example $e^+e^- \to e^+e^-\gamma$ process where all final state particles are reconstructed, the thrust value will not peak exactly at 1 for τ-pair events because of the neutrinos which escape the detector and which need to be taken into account as missing energy and momentum in the event.

On the other hand, the total visible energy of the event, defined as

$$\text{visible energy} = \sum_i E_i, \tag{4.2}$$

where E_i is the energy of a visible particle, is going to be less than $E_{\mathrm{CMS}}/2 = 5.28$ GeV due to missing neutrinos.

We do not expect any π^0s on the tag side since we select only purely leptonic 1-prong decay modes.

We also do not expect many additional photons in our signal events, except for those coming from initial state radiation (ISR) or final state radiation (FSR).

These characteristics will help us separate signal from background in the event reconstruction procedure. Detailed description of the event selections used in this study is discussed in Chapter 6.

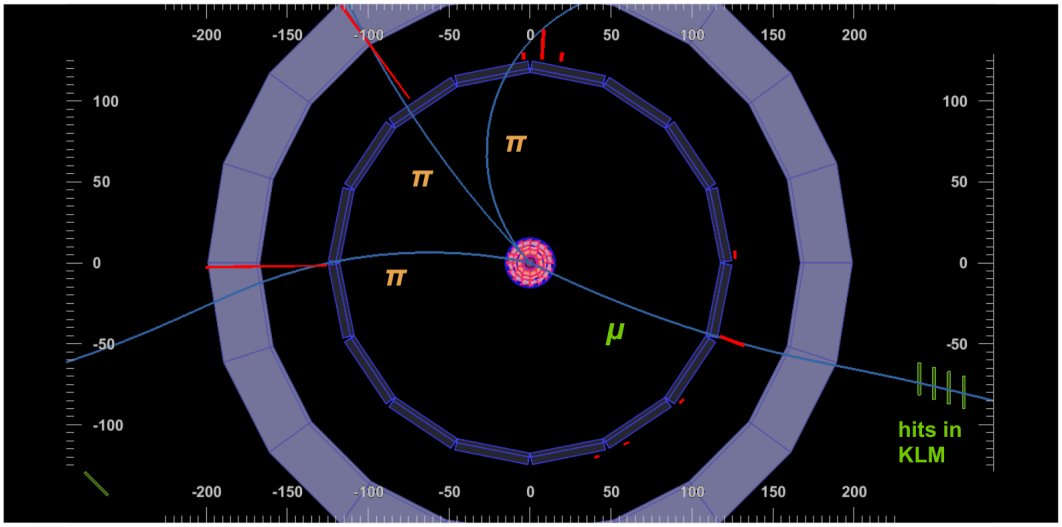

Figure 4.2: *Event display for a candidate signal 3x1-prong signal event reconstructed in Belle II data.* The picture shows the 2D projection of the Belle II detector into the (r, φ) plane. Tracks of four muons were reconstructed with the 3x1-prong topology which is characteristic for τ-pair events.

5. π^0 reconstruction

As was stated in Chapter 1, π^0 reconstruction is very important in particle physics data analyses because inefficient reconstruction of π^0s can cause mixing of samples with different decay modes.

An example of such event migration is shown in Fig.5.1. τ lepton decay modes $\tau \to 3\pi\nu$, $\tau \to 3\pi\pi^0\nu$ and $\tau \to 3\pi 2\pi^0\nu$ only differ by the number of π^0s in the final state and reliable reconstruction of the π^0s is essential in order to distinguish between these events.

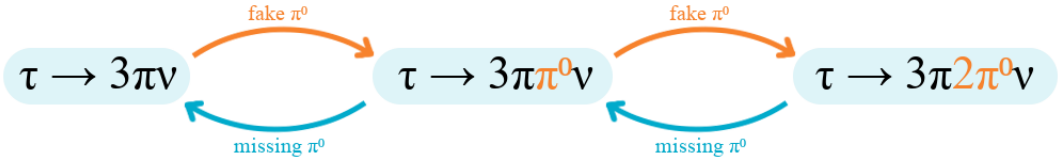

Figure 5.1: *τ decay mode mixing.* τ decay final states can involve different number of π^0 mesons and missing a π^0 or reconstructing a fake can cause event migration between samples. [11]

The π^0 reconstruction efficiency quantifies how many of the produced π^0 were reconstructed. This efficiency can differ in data and simulation. It is essential to measure the π^0 reconstruction efficiency in data in order to correct any mismodelling of the efficiency in MC simulation.

The π^0 mesons are often present in the final states of various processes, not only τ decays, and results obtained from this τ lepton study provide π^0 reconstruction efficiency correction applicable to other physics analyses as well.

This chapter provides more details in π^0 mesons and also defines the π^0 reconstruction efficiency correction, which is the main topic of this thesis.

5.1 π^0 mesons

Neutral pions are the lightest mesons with a mass of (134.9770 ± 0.0005) MeV. π^0 mesons decay very quickly, with a lifetime of $(8.52 \pm 0.18) \times 10^{-17}$ s and the main decay mode is $\pi^0 \to 2\gamma$ with probability of almost 99 % [10]. The reason for such a short lifetime is that the decay into two photons is an electromagnetic process - decays mediated by the weak force are in general much slower.

Therefore, π^0s themselves cannot be detected as they decay almost immediately after they are created. What is measured are the π^0 decay products, the two photons. Photons are measured in ECL where they deposit all of their energy and are absorbed in the crystals. To identify a π^0, two photon ECL clusters have to be matched together, the photon pair coming from a π^0 decay will have its invariant mass close to the π^0 meson mass mentioned above.

However, photons can be produced via other processes, such as ISR or FSR, and we can also detect photons coming from the beam background (see Chapter 2).

Identifying a photon coming from a π^0 decay is therefore not a straightforward task since the background photons can also randomly combine into a pair that has a mass close to the π^0 mass, this combinatorial background then yields fake π^0 candidates.

Another complication is when more than one π^0 is created in the event, it is then again challenging to pair the photon clusters correctly and reconstruct the true π^0s.

The π^0 reconstruction criteria used in this study will be described in Chapter 6.

5.2 Reconstruction efficiency correction

The π^0 reconstruction efficiency describes the fraction of π^0s which were measured and reconstructed compared to the number of created π^0s. In order to compare data and simulation, the reconstruction efficiency in MC has to be corrected to match the efficiency in data.

The efficiency correction for π^0s can be determined as the ratio of the reconstruction efficiencies in data and MC

$$\eta_{\pi^0} = \frac{\epsilon_{\pi^0}^{data}}{\epsilon_{\pi^0}^{MC}}. \tag{5.1}$$

Different approaches can be used to measure this efficiency correction factor. The method* used in this analysis defines the π^0 reconstruction efficiency correction as the following double ratio:

$$\eta_{\pi^0} = \frac{N^{data}(\tau \to 3\pi\pi^0\nu_\tau)}{N^{MC}(\tau \to 3\pi\pi^0\nu_\tau)} \div \frac{N^{data}(\tau \to 3\pi\nu_\tau)}{N^{MC}(\tau \to 3\pi\nu_\tau)}, \tag{5.2}$$

where N^{data} and N^{MC} are the numbers of selected $e^+e^- \to \tau^+\tau^-$ events in data and simulation where one of two τ leptons decayed into a $3\pi\pi^0\nu_\tau$ or $3\pi\nu_\tau$ final state. The second τ is reconstructed in either $\tau \to e\nu_\tau\bar{\nu_e}$ or $\tau \to \mu\nu_\tau\bar{\nu_\mu}$ channel.

The advantage of the double ratio approach is that many of effects other than π^0 efficiency should cancel out in data and MC. The approaches to estimating the signal yields in formula 5.2 are discussed in Chapter 7.

This method was inspired by a similar study on π^0 efficiency correction which was done by the BaBar collaboration. The most important information about the analysis are summarized in Appendix A.1, the original description can be found in [3].

6. Analysis setup

One of the main parts of the analysis involves selecting the signal events and separating them from background. The goal is to obtain a sample with the highest possible purity.

In order to select the signal, various conditions are imposed on particular measured variables. Variables with significant discriminating power are chosen according to the known event characteristics and particle properties. The condition typically results in setting an upper and/or lower limit on a continuous variable, or fixing some overall event characteristic such as constraining the number of reconstructed tracks.

The selection is then optimized with respect to the gain in purity and also with respect to the loss in efficiency. An optimal selection increases the signal purity while maintaining good efficiency, i.e. rejects mainly background events with as small an impact as possible on the signal yield.

Another aspect which needs to be taken into account is the agreement between the real data and simulated data. Because the simulation is not perfect, the response to a certain condition may vary. A requirement which introduces a significant discrepancy between data and MC simulation cannot be used.

This chapter starts with a description of the event selections and particle selections used in this τ lepton study. This is followed by a comparison of the data/MC agreement after the presented selections.

6.1 Event selection

The events in data are first required to fire the *lml0* trigger. As described in Section 2.2.3, this trigger requires at least three ECL clusters at L1, and so it has high efficiency for the signal events.

Based on the known physical properties of τ leptons and their decays, we can further constrain some of the event characteristics in order to select the events we are interested in. The following subsections comprise the used selection requirements.

6.1.1 Tracks

Due to the short life time of the τ lepton, its decay products are expected to originate mainly from the interaction point (IP). Thus, the τ-pair candidate events are selected by requiring four charged tracks with zero net charge (two tracks with plus charge and two with minus charge, summing to zero total charge), satisfying the following conditions:

- -3 cm $<$ dz $<$ 3 cm ,
- dr $<$ 1 cm ,

where dz and dr are the longitudinal and transverse coordinates of the IP.

6.1.2 Charged particles selection

On the tag side we allow only leptonic decays, the charged track of the 1-prong decay is thus required to meet the criteria of being an electron or a muon. For selecting these two kinds of particles, lepton identification (ID) variables are used in this analysis. Particle ID are special variables expressing the likelihood of the track being left by a certain type of particle.

Particle ID is a number between 0 and 1. The values used in this analysis are:

- electronID > 0.9 for electrons,
- muonID > 0.9 for muons,

with

$$\text{electronID} = \frac{\mathcal{L}_\text{e}}{\mathcal{L}_\text{e} + \mathcal{L}_\mu + \mathcal{L}_\pi + \mathcal{L}_\text{K} + \mathcal{L}_\text{p} + \mathcal{L}_\text{d}} \tag{6.1}$$

and

$$\text{muonID} = \frac{\mathcal{L}_\mu}{\mathcal{L}_\text{e} + \mathcal{L}_\mu + \mathcal{L}_\pi + \mathcal{L}_\text{K} + \mathcal{L}_\text{p} + \mathcal{L}_\text{d}}, \tag{6.2}$$

where $\mathcal{L}_e, \mathcal{L}_\mu, \mathcal{L}_\pi, \mathcal{L}_K, \mathcal{L}_p$ and $\mathcal{L}_d$ are the likelihoods of particle hypotheses – electron, muon, pion, kaon, proton and deuteron. These likelihoods are calculated using the information from all available Belle II subdetectors, excluding SVD.

The sample of events which satisfy the condition electronID > 0.9 for the 1-prong track is called the electron channel. Similarly, for muonID > 0.9 it is called the muon channel.

On the 3-prong side, the measured decays are $\tau \to 3\pi\pi^0\nu_\tau$ and $\tau \to 3\pi\nu_\tau$. The three charged tracks thus originate from charged pions. Pions are selected using the following requirements:

- $E/p < 0.8$ for pions,

where E is the energy deposit in the ECL and p is the momentum of the particle in laboratory system. This requirement mainly rejects electrons because for electrons E/p is closer to 1.

At this stage, the contamination from τ decays to K mesons is assumed to be negligible given the branching fractions of $\tau \to K\pi\pi\pi^0\nu$ and $\tau \to KK\pi\pi^0\nu$, see Tab. 1.2.

6.1.3 Neutral particles selection

In this study of the π^0 reconstruction efficiency, we used different sets of selection criteria to reconstruct a π^0. We define eight π^0 selections and then we analyze the reconstruction efficiency for each selection separately.

The π^0s are reconstructed from photon pairs, the selections impose conditions on variables such as photon energy E_γ or invariant mass of the photon pair $M_{\gamma\gamma}$. "Eff60", "Eff50", "Eff40", "Eff30", "Eff20" and "Eff10" are the recommended π^0

selections coming from the Belle II Neutrals Performance Group of the Belle II collaboration in the study of B-decays. They target π^0 reconstruction efficiencies of 60%, 50%, 40%, 30%, 20% and 10%, respectively.

"Nom" π^0 is a selection used specifically in the Belle II τ analyses. "Low" is a modification of "Nom", the difference consist in lower energy threshold for the photon energy.

The selection criteria for the "Nom" and "Low" π^0s are listed in Tab. 6.1, the recommended π^0 selections "Eff60", "Eff50" etc. are summarized in Appendix A.2.

Table 6.1: Different π^0 selections.

Variable	**"Nom"**	**"Low "**
E_γ [MeV]	> 100	> 25
cos θ	[-0.8660, 0.9563]	[-0.8660, 0.9563]
clusterNHits	> 1.5	> 1.5
$M_{\gamma\gamma}$ [MeV]	[115, 152]	[115, 152]

The authors of this study also developed an optimized π^0 selection which is based in the "Low" selection and it is discussed in Chapter 9.

For further reference, we also define π^0 "with side-bands" which are the same sets of selections as what was just described but with the $M_{\gamma\gamma}$ requirements dropped. Those selections will be addressed as "LowSB", "NomSB", "Eff60SB" etc.

Apart from π^0 photons, we also reconstruct additional photons using the following criteria:

- $E_\gamma > 200$ MeV ,
- $-0.8660 < \cos\theta < 0.9563$,
- clusterNHits > 1.5 ,
- not a π^0 photon.

The requirement on $\cos\theta$ corresponds to the range of CDC acceptance, clusterNHits is the number of weighted crystals in the ECL energy cluster.

6.1.4 Background suppression

After requiring events to pass the trigger and the previously mentioned offline selections, there is still substantial background contamination coming mainly from continuum ($e^+e^- \to q\bar{q}, q = u, d, c, s, b$), radiative dilepton processes ($e^+e^- \to \ell^+\ell^-\gamma, \ell = e, \mu$) and 2-photon processes (mostly $e^+e^- \to e^+e^-\mu^+\mu^-$). Additional selections are applied to suppress these background contributions.

On the 3-prong side, the charged track transverse momenta p_T are required to satisfy the following conditions:

- *cut* 1: leading track $p_T > 0.5$ GeV ,
- *cut* 2: subleading track $p_T > 0.2$ GeV ,
- *cut* 3: third track $p_T > 0.05$ GeV .

The tracks are ordered according to their momentum. The requirements are visualised in Fig. 6.1, the value of the condition is marked with a red arrow. Imposing lower threshold on transverse momenta suppresses the low-p_T tracks originating from the dilepton and 2-photon processes whose products are mainly emitted in the direction of the colliding particle beams.

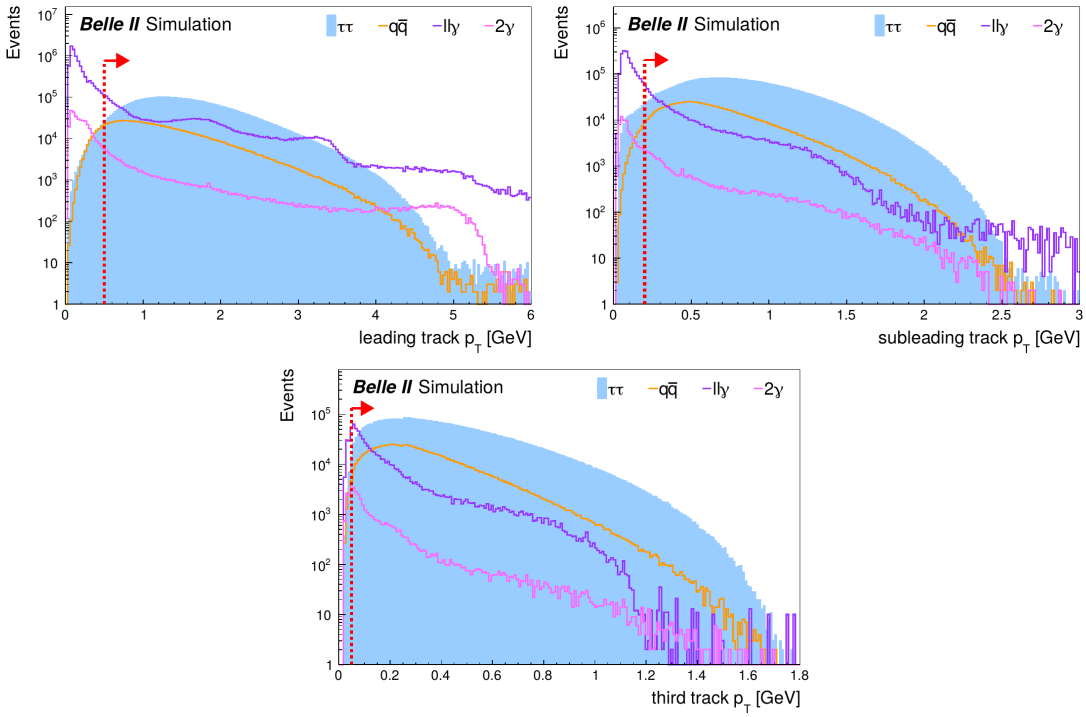

Figure 6.1: *MC track* p_T. The figure shows the distribution of leading track p_T, subleading track p_T after *cut* 1 and third track p_T after *cut* 2. The τ-pair signal (blue filled histogram) is compared to the background contributions (coloured lines). The red arrow marks the value of the requirement.

On the 1-prong side leptonic decays are used. Therefore, no π^0s are allowed to be reconstructed on the 1-prong hemisphere, however at most one photon is allowed:

- *cut* 4: 1-prong $N_{\pi^0} = 0$,
- *cut* 5: 1-prong $N_\gamma \leq 1$.

Photon and π^0 multiplicities are shown in Fig. 6.2. This requirements help to suppress the continuum background, which tends to have a higher neutrals multiplicity compared to the τ-pair signal.

As was explained in Chapter 4, variables with high discrimination power for selecting τ-pair events are the thrust, and visible energy E_{vis} in CMS, the distributions are shown in Fig. 6.3. In this analysis the following requirements were applied:

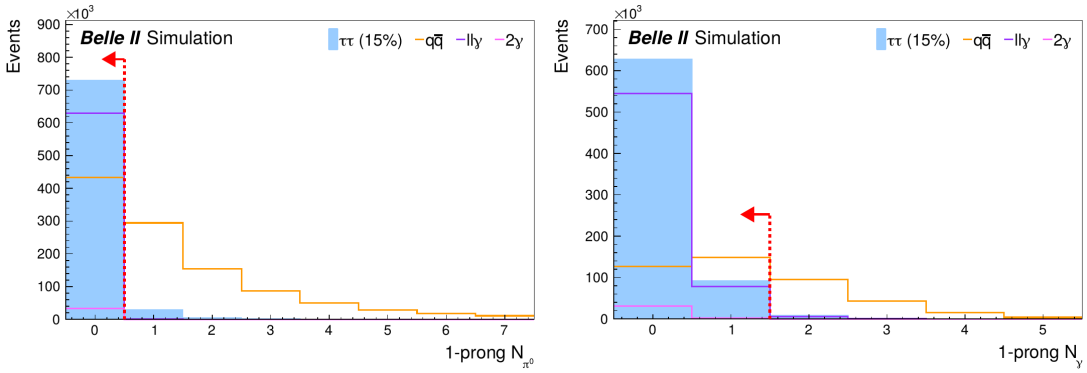

Figure 6.2: *MC photon and π^0 multiplicity* The plots show the photon and π^0 multiplicity on the 1-prong side - N_{π^0} after *cut* 3, N_γ after *cut* 4. The τ-pair is scaled by a factor of 0.15 to make the background more visible.

- *cut* 6: $0.85 <$ thrust < 0.99 ,
- *cut* 7: $1.7 < E_{vis}(\text{CMS}) < 9.1$ GeV .

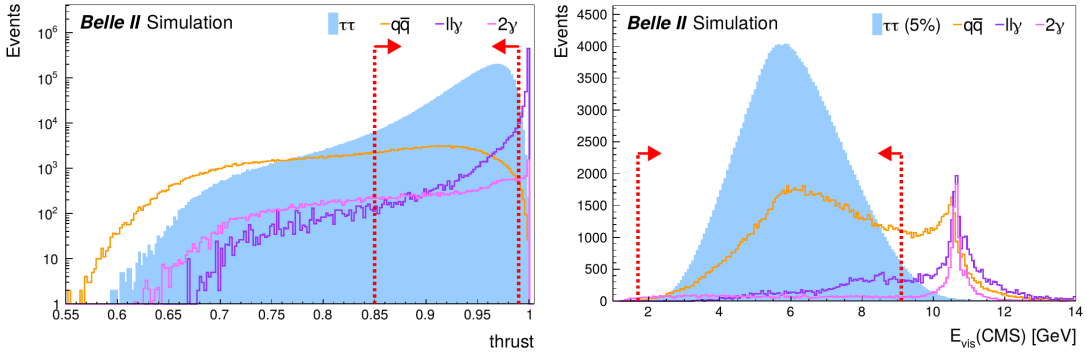

Figure 6.3: *MC thrust and E_{vis}.* Thrust distribution is shown after *cut* 5, $E_{vis}(\text{CMS})$ after *cut* 6. For the $E_{vis}(\text{CMS})$ plot, the τ-pair is scaled by a factor of 0.05 to make the background more visible.

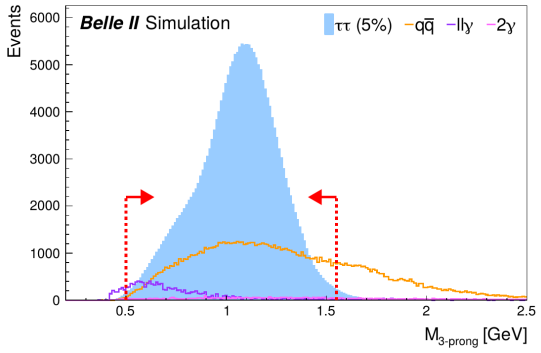

Figure 6.4: *MC $M_{3-prong}$.* The distribution of the invariant mass of the 3-prong side is shown after *cut* 7. The τ-pair is scaled by a factor of 0.05 to make the background more visible.

The requirement on the invariant mass of the 3-prong side shown in Fig. 6.4 reduces the remaining $q\bar{q}$ background component:

- *cut* 8: $0.5 < M_{3-\text{prong}} < 1.55$ GeV .

6.1.5 Efficiency and purity

Usefulness of imposing a requirements was studied in terms of the selection efficiency and the purity of the sample before and after the selection.

The selection efficiency is decined as the number of signal events that pass the selection divided by the number that was generated

Signal purity is defined as

$$purity = \frac{N_{sig}}{N_{sig} + N_{bkg}}, \tag{6.3}$$

where N_{sig} is the number of signal events, N_{bkg} are background events.

After applying the requirements described earlier in this section, the selection efficiency is 45.22 % and purity is 97.84 %. Amongst these τ-pair events, 61.80 % is $\tau \to 3\pi\nu$, 27.81 % is $\tau \to 3\pi\pi^0\nu$ and 10.40 % is $\tau \to other$.

6.1.6 Trigger correction

In data the events which do not fire any trigger are not read out and therefore we lose them while in MC there is no trigger requirement, so the efficiency in collecting events is 100 % in the simulation.

The *lml0* trigger efficiency is measured in data using the following formula

$$\epsilon_{\text{trigger}} \equiv \epsilon_{lml0} = \frac{(fff \vee ffo) \wedge lml0}{fff \vee ffo}, \tag{6.4}$$

where *fff, ffo* and *lml0* are the trigger bits defined in Section 2.2.3. The events are required to fire the ECL-based *lml0* trigger, while the CDC-based *fff* and *ffo* are used as a reference trigger for estimating the efficiency. The information about the fired triggers is taken from data, and the MC events are weighted by the measured ϵ_{lml0} accordingly.

6.2 Data/MC agreement

This section presents the plots of important variables' distributions after the aforementioned selections were applied. The plots compare the data and MC samples, with the signal and various background components shown in different colours. Each MC component (see "Name of the production" in Tab. 3.1) also needs to be scaled by the luminosity factor to match the real data luminosity, that is

$$N_{MC} \quad \to \quad \frac{\mathcal{L}_{data}}{\mathcal{L}_{MC}} \times N_{MC} \tag{6.5}$$

Fig. 6.5 shows thrust and E_{vis} distributions for the 1-prong electron and muon decay channel separately, as well as the combination. Different τ decay modes as well as non-τ background MC components are distinguished using the MC truth information.

In order to avoid possible unblinding of other τ lepton analyses within the Belle II collaboration, the data points in Fig. 6.5 contain all Exp7, Exp8 and Exp10 data but only 10 % of the Exp12 data. This recommendation is important for plotting event variables such as thrust and E_{vis}, however, we have been granted the permission by the collaboration to use all available Exp12 data for looking at π^0-specific variables shown later in this thesis.

6.2.1 Truth-matching

The signal MC component is determined by matching the reconstructed π^0s to real π^0s using the MC truth information. In each event, multiple π^0 candidates are reconstructed and they can be ordered by their energies within one event. There can always be just one real π^0 in the signal event so only one of the candidates is truth-matched to the real π^0.

Fig. 6.6 shows the data/MC agreement of the π^0 mass distribution for all eight π^0 selections in the full $M_{\gamma\gamma}$ range. The $\tau\tau(real)$ MC component counts only π^0 reconstructed from such pair of photons where both of the photons were truth-matched to the same generated π^0, while $\tau\tau(fake)$ contains all π^0 candidates where either one or both of the photons come from the background.

The distributions in Fig. 6.6 corresponds to the π^0 candidate which has the highest momentum among the π^0s reconstructed in one event.

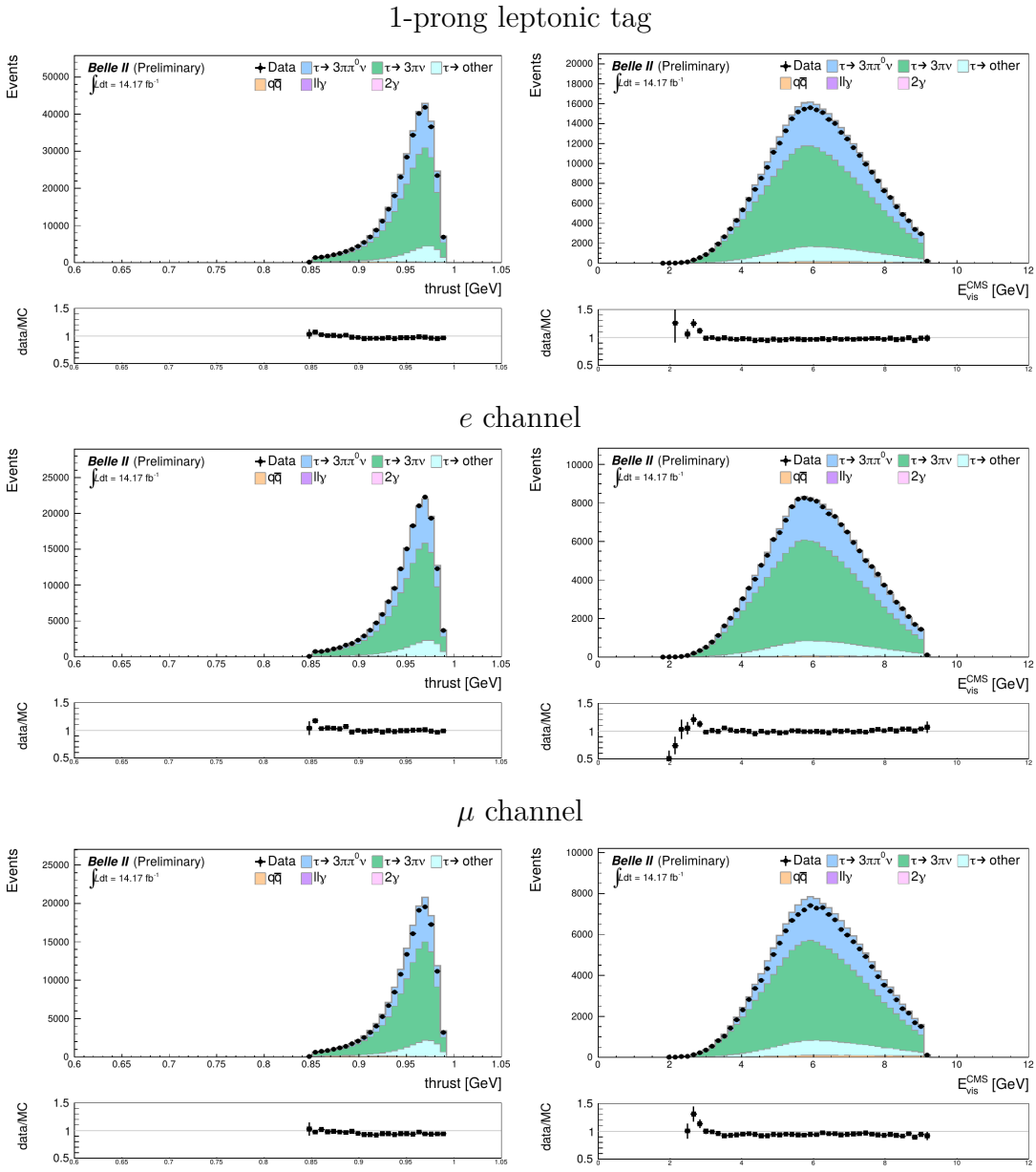

Figure 6.5: *Thrust and visible energy.* The plots show the thrust value and E_{vis} in CMS after the selections described in this section. The top two plots show all events, the middle two plots show only events in the electron channel, the bottom two plots show events in the muon channel. These plots include only 10 % of Exp12 data. Statistical uncertainties are shown.

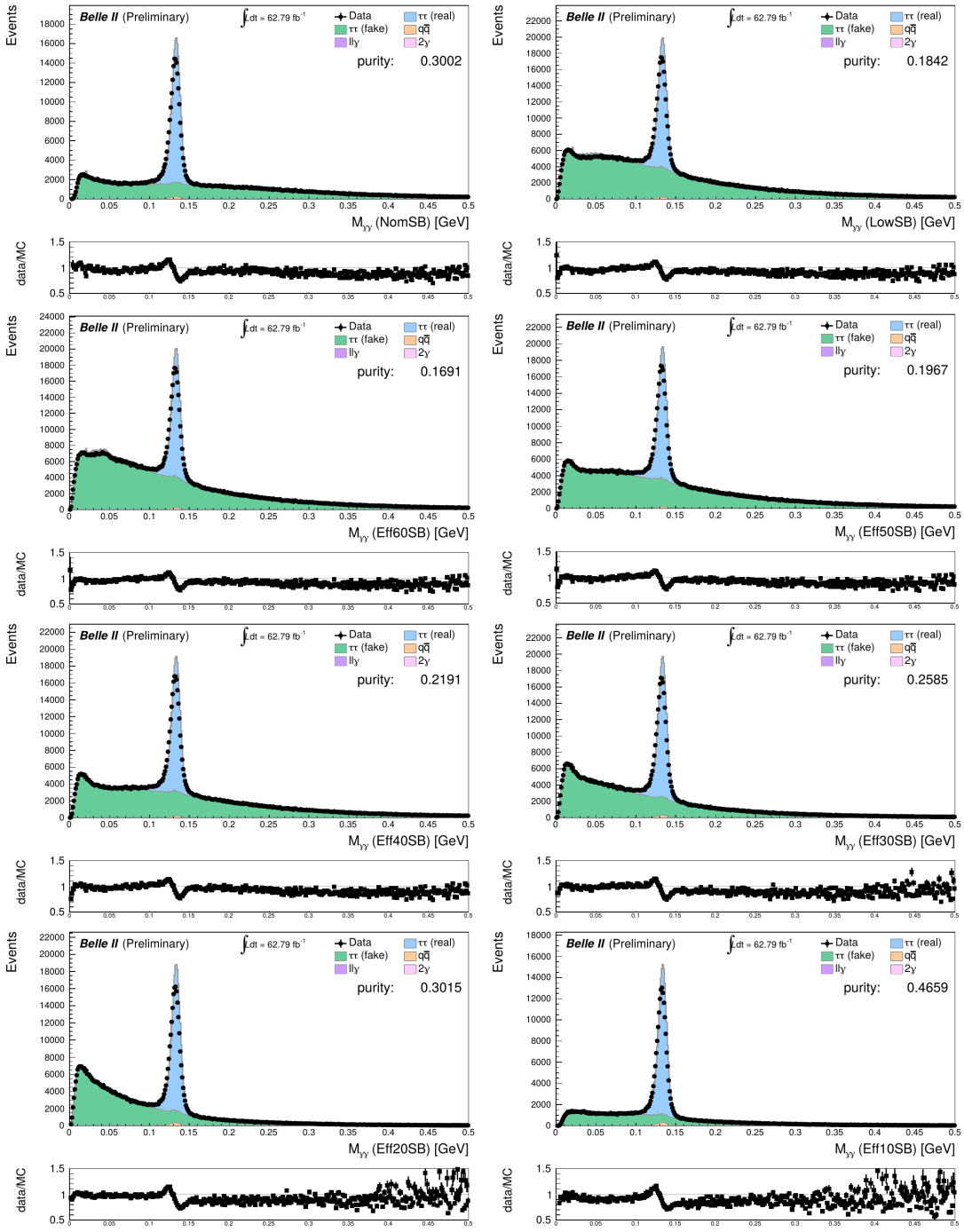

Figure 6.6: *$M_{\gamma\gamma}$ data/MC agreement.* The figure includes plots of full $M_{\gamma\gamma}$ distributions for "NomSB", "LowSB", "Eff60SB", "Eff50SB", "Eff40SB", "Eff30SB", "Eff20SB" and "Eff10SB" π^0 selections, respectively. Statistical uncertainties are shown.

7. Signal selection

In order to obtain the number of events for the efficiency correction formula (Eq. 5.2), we need to estimate the signal yield of our samples, separately for each of the eight π^0 types defined in Chapter 5, for both data and MC. A different approach was used for the signal of $\tau \to 3\pi\pi^0\nu$ and $\tau \to 3\pi\nu$ events. This chapter describes the methods used and summarizes the resultant signal yields.

7.1 $3\pi\pi^0$ signal

As was described in Chapter 6.2.1, there can always be just one real π^0 in the signal event. In most of the cases the π^0 candidate with the highest energy is the true one, the fake π^0s are often reconstructed from background photons which have lower energy than the true π^0 photons. However, it can also happen that the π^0 candidate with highest energy is fake and the true π^0 is one of the candidates with lower energy.

As an example, Fig. 7.1 shows the mass distributions of the three highest energy π^0 candidates for "Eff20SB" π^0s. The signal "$\tau\tau$ (real)" peaks around the π^0 mass, while the background "$\tau\tau$ (fake)" is a smoothly falling distribution.

To increase our $\tau \to 3\pi\pi^0\nu$ signal yield we are summing the π^0 mass distributions of the three reconstructed π^0 candidates with the highest energy. Since there is only one real π^0 in each event, this summing does not lead to double counting signal events.

The resultant distribution is then fitted with a combination of a peak function for the signal and a polynomial function for the background. The signal yield is then calculated as the integral over the signal function within the mass window. This mass range is different for each of the considered π^0 selections, the values of the mass cuts are summarized in Tab. 7.1.

Table 7.1: π^0 mass window.

π^0 selection	M_{min} (GeV)	M_{max} (GeV)
"Eff10"	0.127	0.139
"Eff20"	0.121	0.142
"Eff30"	0.120	0.145
"Eff40"	0.120	0.145
"Eff50"	0.105	0.150
"Eff60"	0.030	-
"Nom"	0.115	0.152
"Low"	0.115	0.152

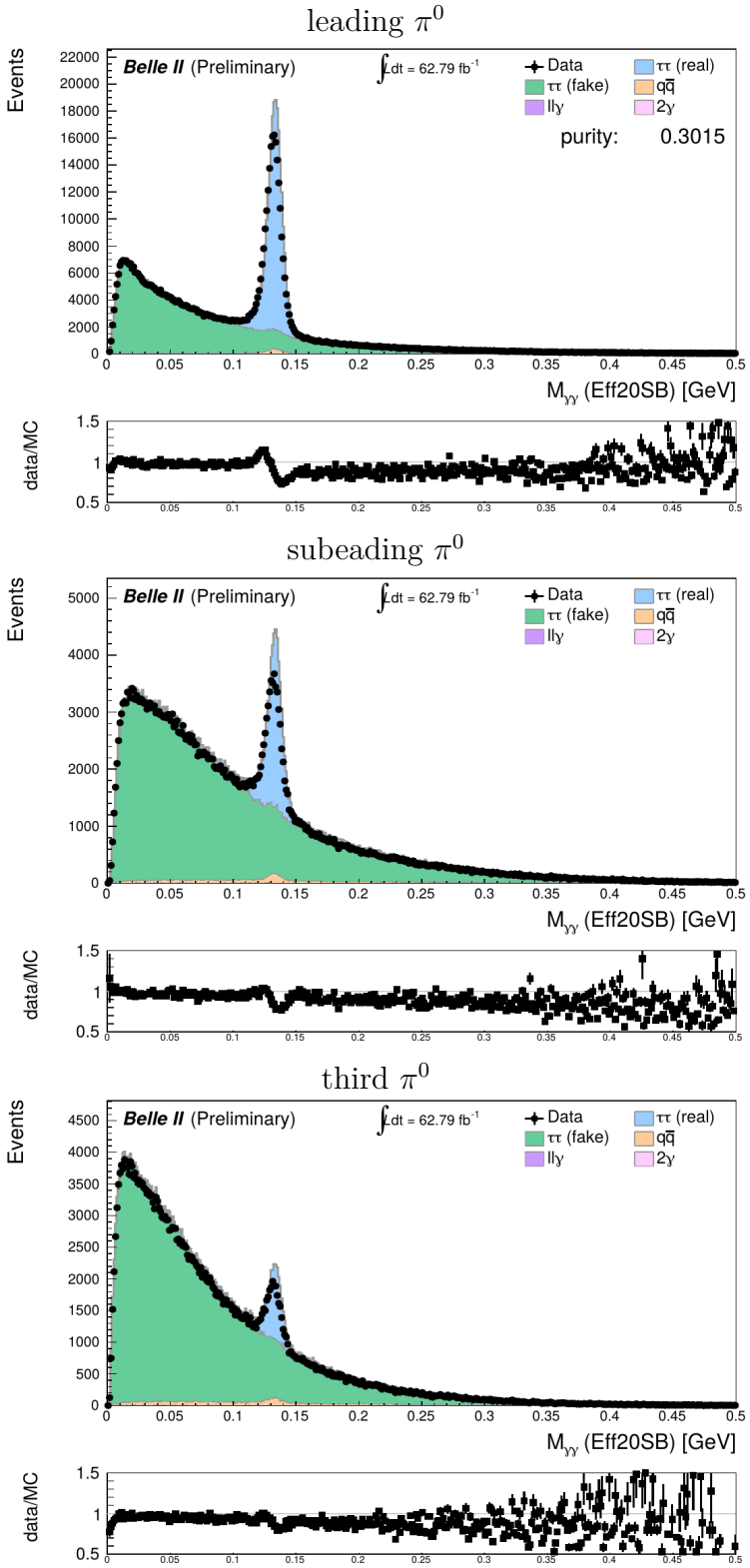

Figure 7.1: $3\pi\pi^0$ *signal definition example.* These plots show the $M_{\gamma\gamma}$ distributions for the the π^0s with the highest energy reconstructed using the "Eff20SB" selection criteria.

7.1.1 Fitting procedure

Fitting of the mass distributions was done within the ROOT framework [25] using the RooFit library [26]. For defining the model probability distribution function (pdf) we used pre-defined ROOT functions and combined these functions into a pdf by means of an extended maximum likelihood fit. More details about this method in RooFit is described in Chapter 3 of [26], the general description of the extended maximum likelihood can be found in [27]. The goodness of fit was evaluated in terms of χ^2/ndf.

The peak function used for calculating the signal yield is the sum of two Gaussians (double Gaussian), the background is the 3rd order polynomial. The definition of a Gaussian is given below:

$$G(x;\mu,\sigma) = \frac{1}{\sigma\sqrt{2\pi}} \times \exp\left(-\frac{(x-\mu)^2}{2\sigma^2}\right), \tag{7.1}$$

the plot of the Gaussian function is shown in Fig. 7.2. Several other peak functions were also considered, an example of a comparison of the fit results can be found in Appendix B.1. This choice of the double Gaussian proved itself to be the best for our analysis in terms of χ^2/ndf and stability of the fitting process.

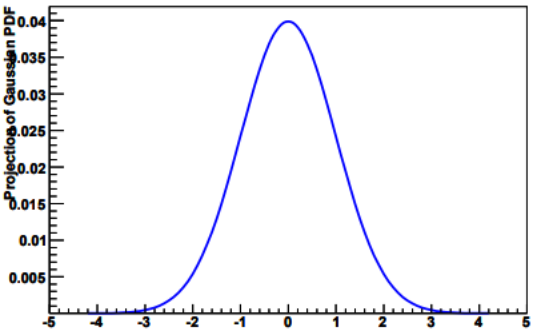

Figure 7.2: *Gaussian pdf.* The plot shows the characteristic shape of the Gaussian function. [28]

The resultant pdf has the following form

$$pdf = n_1^{sig} \cdot G_1 + n_2^{sig} \cdot G_2 + n^{bkg} \cdot P, \tag{7.2}$$

where G_1 and G_2 are the two Gaussian functions and P is the polynomial function

$$P(x) = T^{(0)}(x) + c_1 \cdot T^{(1)}(x) + c_2 \cdot T^{(2)}(x) + c_3 \cdot T^{(3)}(x), \tag{7.3}$$

where

$$\begin{aligned} T_{(0)}(x) &= 1 \\ T_{(1)}(x) &= x \\ T_{(2)}(x) &= 2x^2 - 1 \\ T_{(3)}(x) &= 4x^3 - 3x \end{aligned} \tag{7.4}$$

are the Chebyshev polynomials of the first kind.

The factors n_1^{sig}, n_2^{sig} and n^{bkg} are the numbers of events. The pdf is then not normalized to 1 but to $n_1^{sig}+n_2^{sig}+n^{bkg}$. These factors are then used for estimating the signal yield which is calculated as

$$n^{sig} = n_1^{sig} \cdot f_1^{sig} + n_2^{sig} \cdot f_2^{sig} \equiv n_1 + n_2, \tag{7.5}$$

where f_1^{sig}, f_2^{sig} are the integrals of G_1 and G_2 over the mass window range. This factor represents the fraction of signal events which fulfil the mass requirement of the given π^0 selection from Tab. 7.1.

The error propagation of signal yield uncertainty $\sigma^2(n^{sig})$ was calculated as

$$\sigma^2(n^{sig}) = \sigma_1^2 + \sigma_2^2 + 2\ \mathrm{cov}(n_1, n_2), \tag{7.6}$$

with

$$\sigma_{1,2}^2 = n_{1,2}^2 \cdot \left(\frac{\sigma^2(n_{1,2}^{sig})}{(n_{1,2}^{sig})^2} + \frac{\sigma^2(f_{1,2}^{sig})}{(f_{1,2}^{sig})^2} \right). \tag{7.7}$$

The uncertainties of $n_{1,2}^{sig}$ are determined as statistical uncertainties of the fit parameters, the list of parameters entering the pdf formula in Eq. 7.2 is summarized in Tab. 7.2. The uncertainties of $f_{1,2}^{sig}$ are estimated by propagating the pdf parameters' uncertainties into the integrals of the pdfs $G_{1,2}$. This is handled by RooFit which also takes into account the correlation between the parameters. The correlation term entering the formula in Eq. 7.6 reduces to the covariance of n_1^{sig} and n_2^{sig} since the integrals f_1^{sig}, f_2^{sig} are calculated independently of the fitting procedure, so

$$\mathrm{cov}(n_1, n_2) = \mathrm{cov}(n_1^{sig}, n_2^{sig}). \tag{7.8}$$

Table 7.2: Double Gaussian fit parameters.

Parameter	Description
μ_1	mean of G_1
σ_1	sigma of G_1
μ_2	mean of G_2
σ_2	sigma of G_2
c_1	linear term coefficient of P
c_2	quadratic term coefficient of P
c_3	cubic term coefficient of P
n_1^{sig}	normalization of G_1
n_2^{sig}	normalization of G_2
n^{bkg}	normalization of P

7.1.2 Fit results

The π^0 mass distributions were fitted in the same way for both data and the total (signal + background) MC distributions, for all of the considered π^0 selections.

Fig. 7.3 and 7.4 show the fitted distributions. The plots also include the χ^2 and χ^2/ndf values, and the signal yield which is the integral of the post-fit signal function over the mass window range marked by vertical lines.

7.2 3π signal

The signal for $\tau \to 3\pi\nu$ was determined from events with $N_{\pi^0} = 0$. The distributions of π^0 multiplicity on the 3-prong side can be found in Appendix B.3. The plots in Fig. 7.5 show the E_{vis} distributions of events with no reconstructed π^0s.

The MC signal yield is then determined as the number of events truth-matched to $\tau \to 3\pi\nu$ decay mode. The signal yield in data is calculated after subtracting the MC background components,

$$n_{sig}^{data} = n_{total}^{data} - n_{bkg}^{MC}, \tag{7.9}$$

where n_{total}^{data} is the total number of data events with $N_{\pi^0} = 0$, and n_{bkg}^{MC} is the sum of all MC components other than $\tau \to 3\pi\nu$.

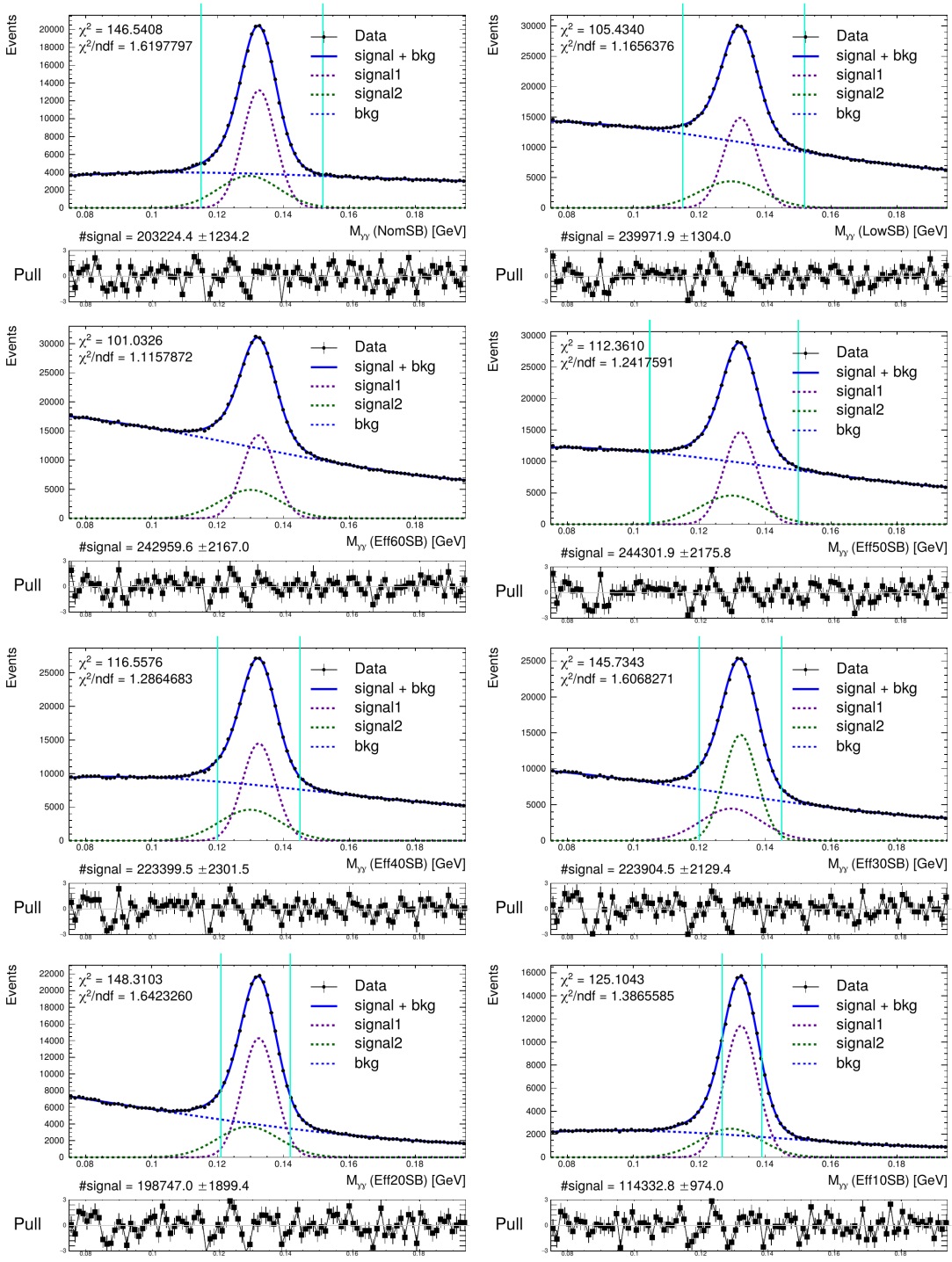

Figure 7.3: *$M_{\gamma\gamma}$ double Gaussian fits (data).* The plots show the double Gaussian fits of the π^0 mass distributions in data for "NomSB", "LowSB", "Eff60SB", "Eff50SB", "Eff40SB", "Eff30SB", "Eff20SB" and "Eff10SB" π^0 selections. Vertical lines mark the mass window as indicated in Tab. 7.1.

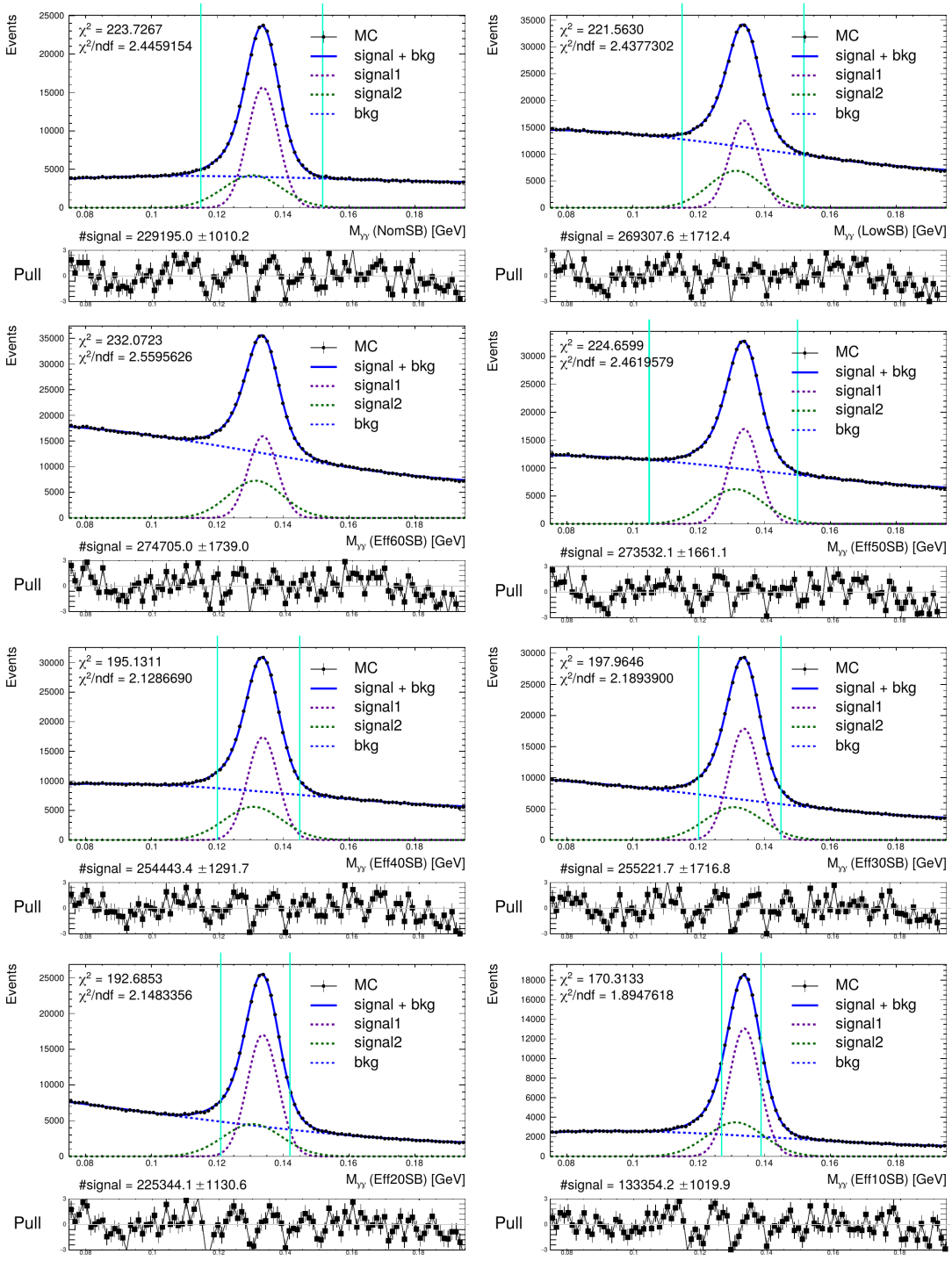

Figure 7.4: *$M_{\gamma\gamma}$ double Gaussian fits (MC).* The plots show the double Gaussian fits of the π^0 mass distributions in MC for "NomSB", "LowSB", "Eff60SB", "Eff50SB", "Eff40SB", "Eff30SB", "Eff20SB" and "Eff10SB" π^0 selections. Vertical lines mark the mass window as indicated in Tab. 7.1.

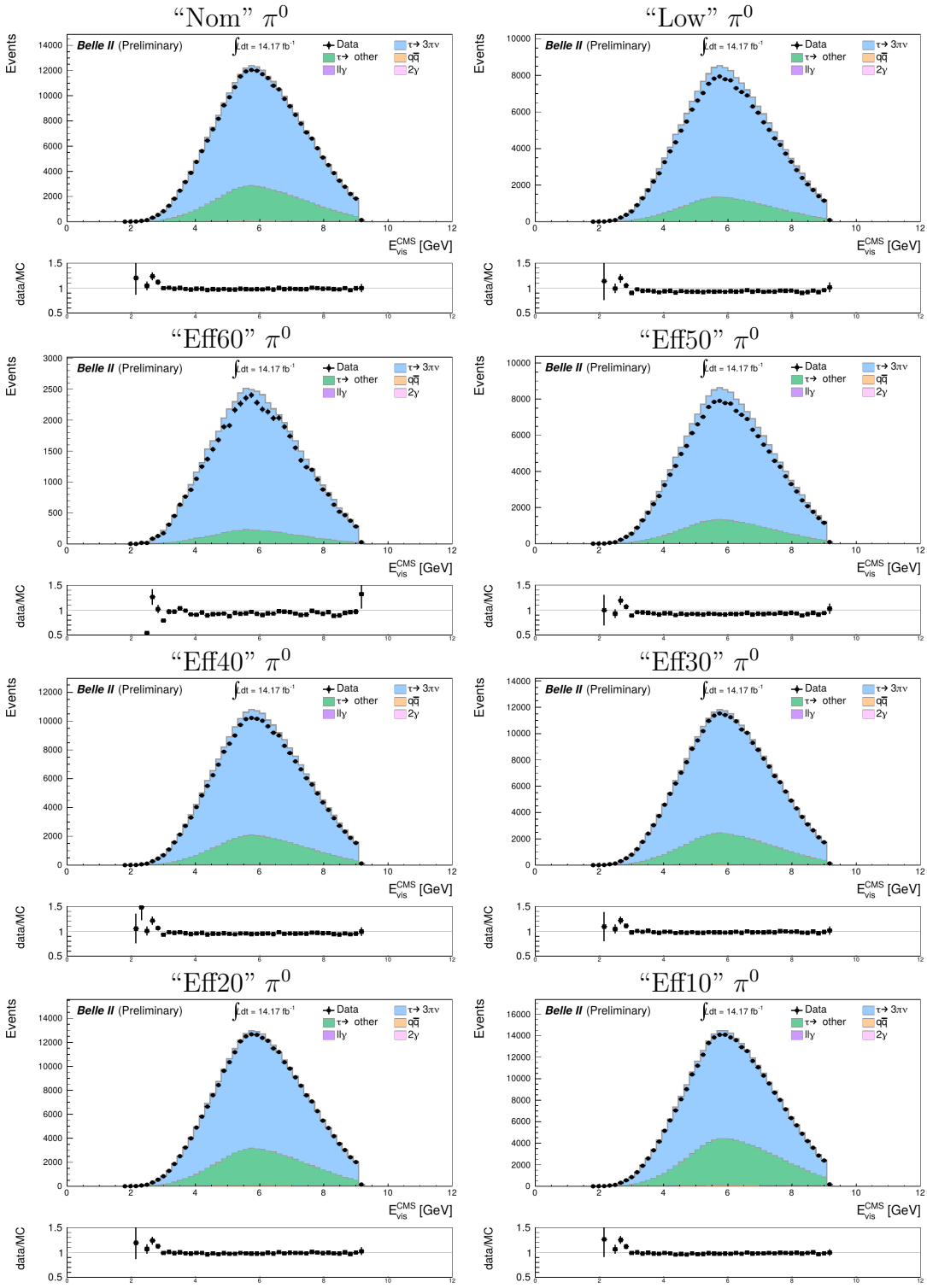

Figure 7.5: *E_{vis} for $N_{\pi^0} = 0$ events.* The plots show E_{vis} distributions of events with $N_{\pi^0} = 0$ for "Nom", "Low", "Eff60", "Eff50", "Eff40", "Eff30", "Eff20" and "Eff10" π^0 selections. In accord with Chapter 6, the plots of E_{vis} include only 10 % of Exp12 data.

7.3 Signal yields summary plots

The signal yields were calculated for $\tau \to 3\pi\pi^0\nu$ and $\tau \to 3\pi\nu$ event both in data and MC using the methods described in the preceding sections. The resultant values are summarized in the plots in Fig. 7.6.

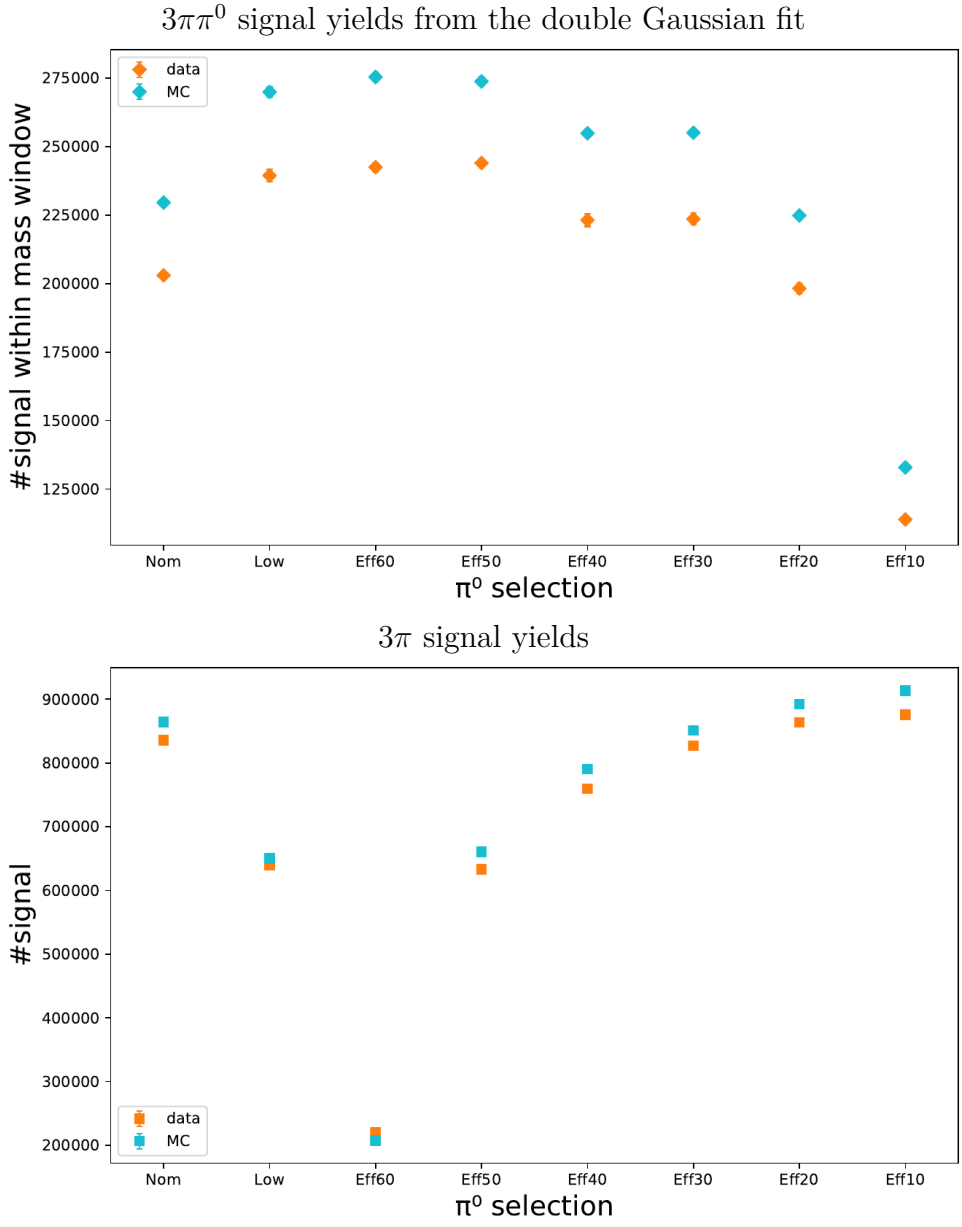

Figure 7.6: *Signal yields.* Shown plots summarize the signal yields of the $\tau \to 3\pi\pi^0\nu$ and $\tau \to 3\pi\nu$ events in data and MC for all considered π^0 selections. The both $3\pi\pi^0$ and 3π signal yields signal yields were measured using the full data statistics. The uncertainties shown in the $3\pi\pi^0$ signal yields plot were calculated according to Eq. 7.6, uncertainties of the 3π signal yields are statistical only.

8. Results on π^0 efficiency

Using Eq. 5.2, the π^0 reconstruction efficiency correction between the data and MC was calculated for the eight considered π^0 selections (see Section 6.1.3). This chapter presents the results on the average efficiency correction, as well as the momentum dependent correction.

8.1 Uncertainty

The total uncertainty of the π^0 efficiency correction η_{π^0} was calculated from the statistical uncertainty σ^2_{stat} and total systematic uncertainty $\sigma^2_{\text{total syst}}$:

$$\sigma^2_{\text{total}} = \sigma^2_{\text{stat}} + \sigma^2_{\text{total syst}}. \tag{8.1}$$

The following subsections describe the individual contributions and summarize the resultant values of the uncertainties.

8.1.1 Statistical uncertainty

The statistical uncertainty of the π^0 efficiency correction η_{π^0} (Eq. 7.6) was calculated as

$$\sigma^2_{\text{stat}} = \eta^2_{\pi^0} \cdot \left(\frac{(\sigma^{data}_{3\pi\pi^0})^2}{(N^{data}(\tau \to 3\pi\pi^0\nu_\tau))^2} + \frac{(\sigma^{MC}_{3\pi\pi^0})^2}{(N^{MC}(\tau \to 3\pi\pi^0\nu_\tau))^2} + \right. \\ \left. + \frac{(\sigma^{data}_{3\pi})^2}{(N^{data}(\tau \to 3\pi\nu_\tau))^2} + \frac{(\sigma^{MC}_{3\pi})^2}{(N^{MC}(\tau \to 3\pi\nu_\tau))^2} \right), \tag{8.2}$$

where the uncertainties $\sigma^{data}_{3\pi\pi^0}, \sigma^{MC}_{3\pi\pi^0}$ were calculated according to Eq. 7.6 and $\sigma^{data}_{3\pi}, \sigma^{MC}_{3\pi}$ are statistical only. N^{data} and N^{MC} are defined in Chapter 5.

The resultant values of the statistical uncertainty are listed in Tab. 8.1.

8.1.2 Systematic uncertainties

The following set of systematic uncertainties was considered:

- fit function uncertainty σ^2_{fit},
- luminosity uncertainty σ^2_{lumi},
- trigger efficiency uncertainty σ^2_{trig},
- leptonID efficiency uncertainty $\sigma^2_{\text{LID eff}}$,
- leptonID fake rate uncertainty $\sigma^2_{\text{LID fake}}$,
- BR uncertainty σ^2_{BR},
- tracking efficiency uncertainty σ^2_{track}.

Fit function uncertainty: Systematic uncertainty of the fit was estimated by means of comparing the used fit pdf and a fit with different pdf with similarly good performance. The variance is then evaluated as the difference of the central values of signal yields estimated from the two fit models. The reference fit combines Crystal Ball (CB) function,

$$CB(x;\mu,\sigma,\alpha,n) = \begin{cases} \frac{1}{\sigma\sqrt{2\pi}} \times \exp\left(-\frac{(x-\mu)^2}{2\sigma^2}\right), & \text{for} \quad x > \mu - \alpha\sigma, \\ \frac{1}{\sigma\sqrt{2\pi}} \times \frac{(n/\alpha)^n \exp(-\alpha^2/2)}{((\mu-x)/\sigma + n/\alpha - \alpha)}, & \text{for} \quad x \leq \mu - \alpha\sigma \end{cases}, \tag{8.3}$$

for the signal and 3rd order polynomial for the background. The characteristic shape of the CB distribution is shown in Fig. 8.1.

The examples of the CB fits are given in Fig. 8.2, the rest of the plots can be found in Appendix B.2.

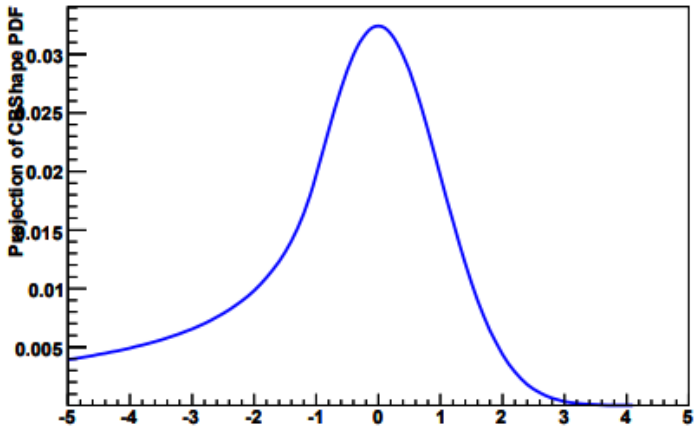

Figure 8.1: *CB pdf.* The plot shows the typical shape of the CB function. [28]

Luminosity uncertainty: The uncertainty on the total integrated luminosity of the data sample. This was measured using Bhabha and digamma events to be 62.79 ± 0.005 fb^{-1} [29].

Trigger efficiency uncertainty: The uncertainty on the *lml*0 trigger efficiency measured in data and used to correct MC, as described in Section 2.2.3.

LeptonID efficiency uncertainty: The uncertainty associated to the difference between data and MC in the electronID and muonID efficiencies. These uncertainties were provided by the Belle II Lepton ID Group, and were measured using $J/\Psi \to \ell^+\ell^-$ decays, as well as 2-photon and radiative dimuon events [30].

LeptonID fake rate uncertainty: The uncertainty associated to the difference between data and MC in the electronID and muonID mis-identification or "fake" rates. These uncertainties were also provided by the Belle II Lepton ID Group, and were measured using $K^0_s \to \pi^+\pi^-$, $D^{*+} \to D^0(K^-\pi^+)\pi^+$ and τ-pair decays [30].

BR uncertainty: The uncertainty on the $\tau \to 3\pi\nu$ and $\tau \to 3\pi\pi^0\nu$ BRs [10].

Tracking efficiency uncertainty: The uncertainty associated to the difference between data and MC in the track reconstruction efficiency. This uncertainty was provided by the Belle II Tracking Group, and was measured using τ-pair decays [31].

All systematic uncertainties were summed in quadrature:

$$\sigma^2_{\text{total syst}} = \sigma^2_{\text{fit}} + \sigma^2_{\text{lumi}} + \sigma^2_{\text{trig}} + \sigma^2_{\text{LID eff}} + \sigma^2_{\text{LID fake}} + \sigma^2_{\text{BR}} + \sigma^2_{\text{track}}. \tag{8.4}$$

The resultant variations on the average efficiency corrections due to the considered systematic sources are listed in Tab. 8.1.

Table 8.1: Uncertainties on the average efficiency corrections.

Uncertainty [%]	Low	Nom	Eff60	Eff50	Eff40	Eff30	Eff20	Eff10
fit	± 0.30	± 0.15	± 0.46	± 0.11	± 0.09	± 0.10	± 0.27	± 0.87
luminosity	± 0.03	± 0.02	< 0.01	± 0.01	± 0.02	± 0.01	± 0.02	< 0.01
trigger efficiency	± 0.01	± 0.05	± 0.04	± 0.07	± 0.05	± 0.02	± 0.02	± 0.03
leptonID efficiency	± 1.00	± 1.69	± 0.49	± 1.00	± 1.33	± 1.46	± 1.84	± 3.19
leptonID fake rate	± 0.05	± 0.59	± 0.35	± 0.10	± 0.37	± 0.30	± 0.57	± 1.16
BR	± 0.03	± 0.03	± 0.01	± 0.08	± 0.02	± 0.01	± 0.01	± 0.01
tracking efficiency	± 0.61	± 0.91	± 0.35	± 0.62	± 0.74	± 0.83	± 0.96	± 1.28
systematic uncertainty	± 1.21	± 2.01	± 0.84	± 1.19	± 1.57	± 1.70	± 2.17	± 3.73
statistical uncertainty	± 1.19	± 0.77	± 1.01	± 0.95	± 1.20	± 1.13	± 1.14	± 1.34
total uncertainty	± 1.69	± 2.16	± 1.32	± 1.52	± 1.98	± 2.04	± 2.45	± 3.96

This table shows the % uncertainty on the average correction for the eight studied π^0 selections. The first seven rows list the resultant variations due to the considered systematic sources. The last three rows show the total systematic uncertainty $\sigma_{total\ syst}$ (Eq. 8.4), the statistical uncertainty σ_{stat} (Eq. 8.2), and the total π^0 efficiency correction uncertainty σ_{total} (Eq. 8.1).

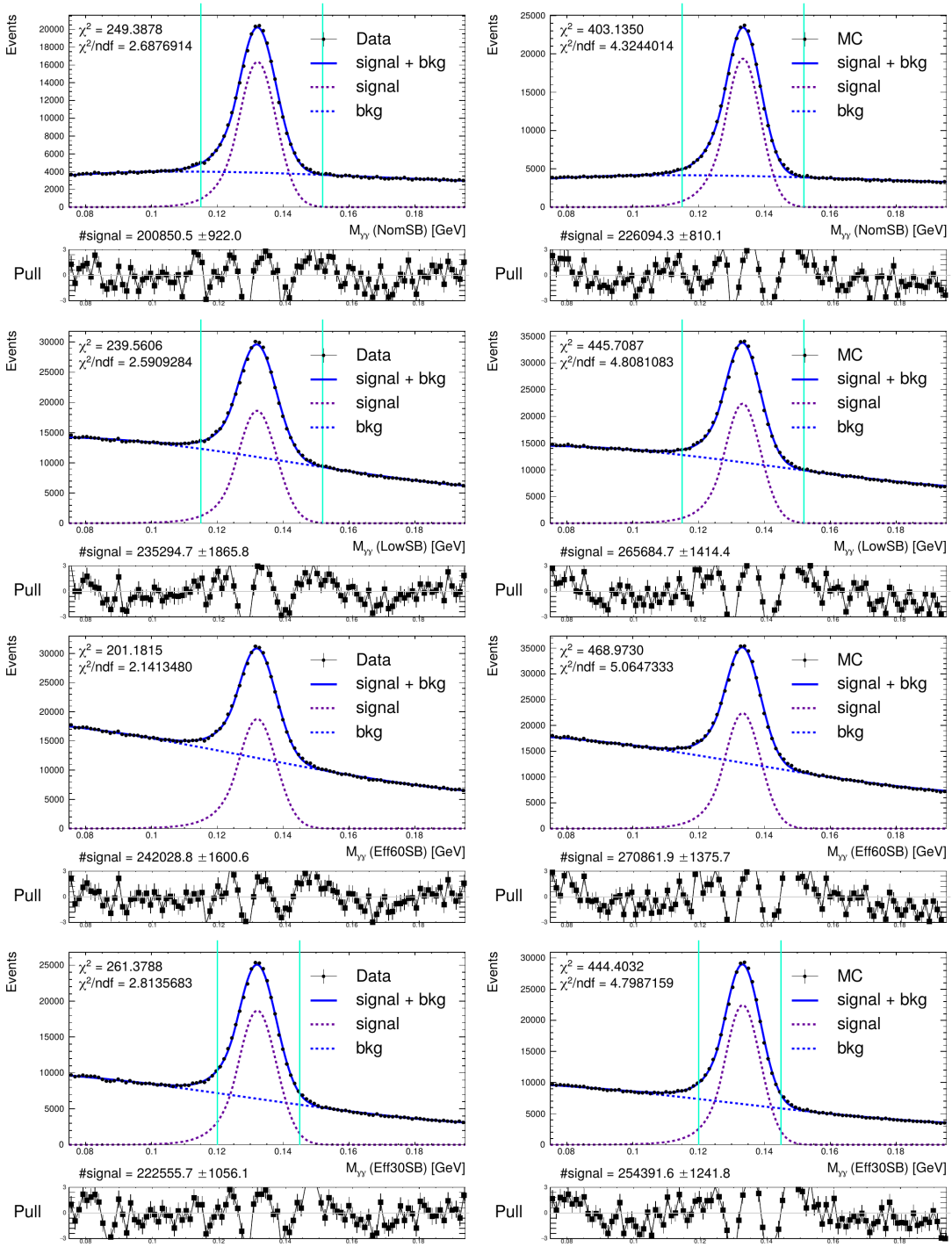

Figure 8.2: *$M_{\gamma\gamma}$ CB fits (examples).* The plots show examples of the CB fits of the π^0 mass distributions in data and MC for "NomSB", "LowSB", "Eff60SB" and "Eff30SB" π^0 types.

8.2 Average correction

The results for the π^0 efficiency correction integrated over the whole momentum region are summarized in Fig. 8.3. The statistical uncertainty was calculated using Eq. 8.2, the total uncertainty was determined by Eq 8.1.

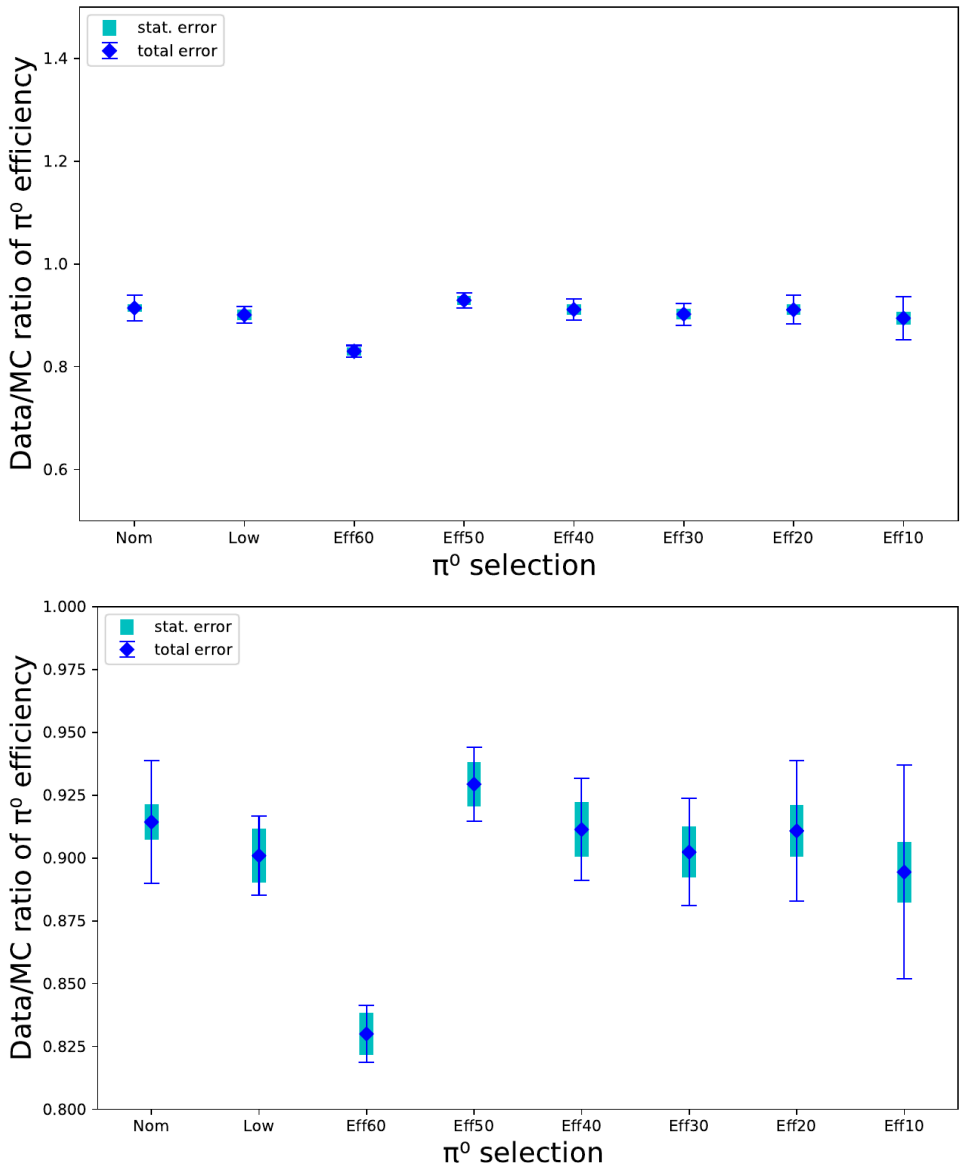

Figure 8.3: *Average π^0 reconstruction efficiency correction.* The plots summarize π^0 reconstruction efficiency correction between data and MC for all considered π^0 selections. The lower plot shows the same results with y-axis zoomed in. The uncertainties shown were determined using Eq. 8.2 and Eq 8.1.

8.3 Momentum dependent correction

For estimating the momentum dependence of the efficiency correction, the samples were divided into 11 π^0 momentum bins. To obtain the signal yield, the π^0

mass distributions were fitted using the procedure described in Chapter 7. The fit plots are included in Appendix B.4.

Fig. 8.4 shows the momentum distribution for "LowSB" π^0s. Because the low-momentum region is dominated by background, the first momentum bin was chosen in such a way that the signal peak of π^0 mass within this momentum range is prominent enough to be fitted with the pdf. The other 10 bins were optimized with respect to the "LowSB" π^0 signal, i.e. each of the 10 bins contains approximately the same number of "LowSB" π^0 signal events. The bin ranges are summarized in Tab. 8.2. The same momentum binning was used for all other π^0 selections.

The momentum dependence of π^0 reconstruction efficiency correction is shown in Fig. 8.5, Fig. 8.6 and Fig. 8.7 for the different considered π^0 selections.

The results will be discussed in Chapter 10.

Table 8.2: π^0 momentum bins.

p_{π^0} bin	p_{π^0} range [GeV]
p_1	< 0.67
p_2	[0.67, 0.77]
p_3	[0.77, 0.90]
p_4	[0.90, 1.03]
p_5	[1.03, 1.17]
p_6	[1.17, 1.30]
p_7	[1.30, 1.47]
p_8	[1.47, 1.57]
p_9	[1.57, 1.80]
p_{10}	[1.80, 2.23]
p_{11}	> 2.23

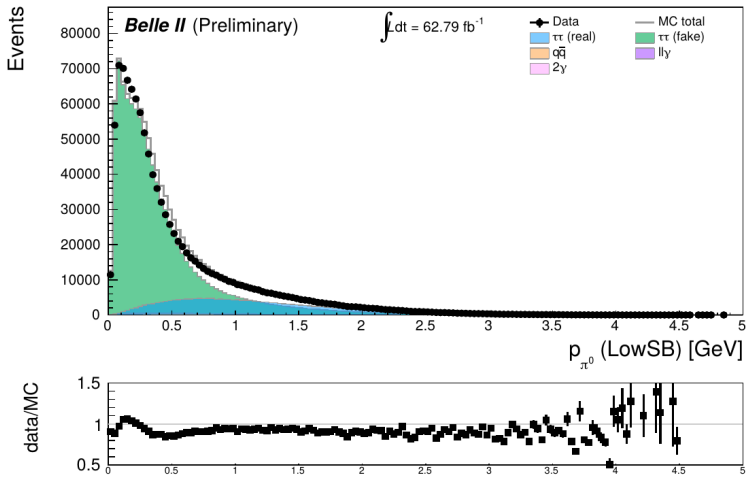

Figure 8.4: π^0 *momentum.* This plot shows the π^0 momentum distribution for "LowSB" π^0s. The signal component "$\tau\tau$ (real)" is shown unstacked.

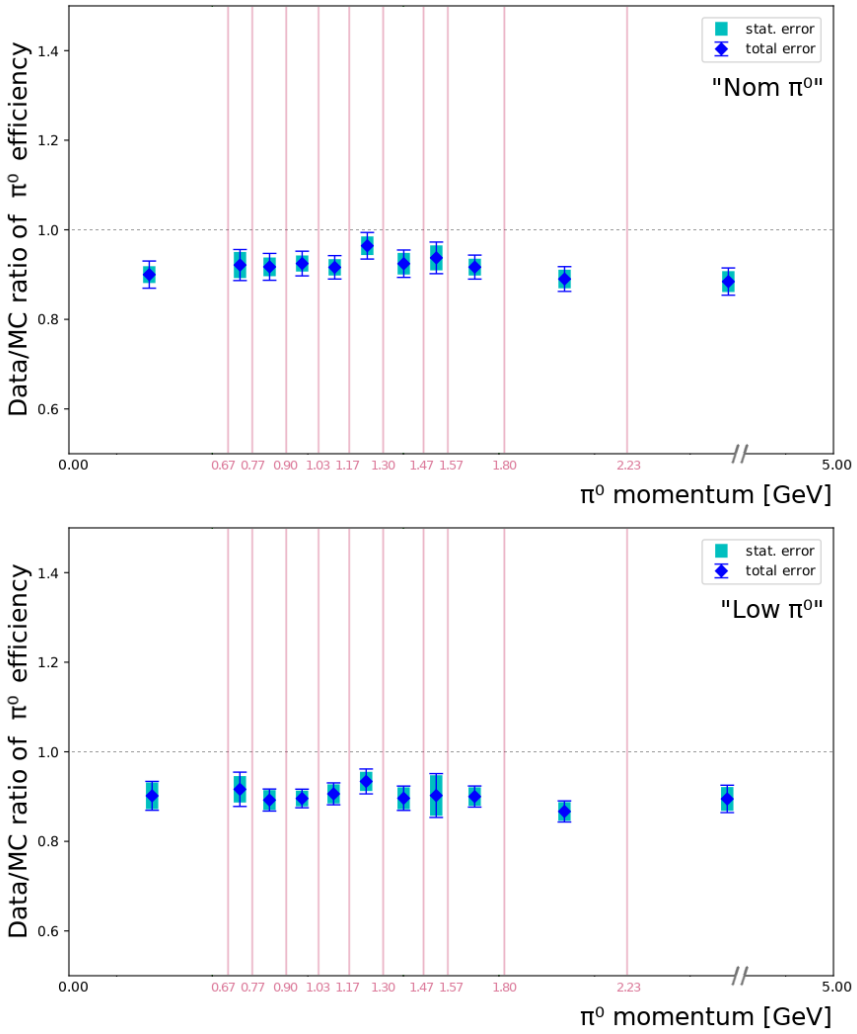

Figure 8.5: *Momentum dependent π^0 reconstruction efficiency correction (i).* The efficiency correction was calculated in 11 momentum bins, the figure shows the p_{π^0} dependence for "Nom" and "Low" π^0 selections. The uncertainties shown were determined using Eq. 8.2 and Eq 8.1.

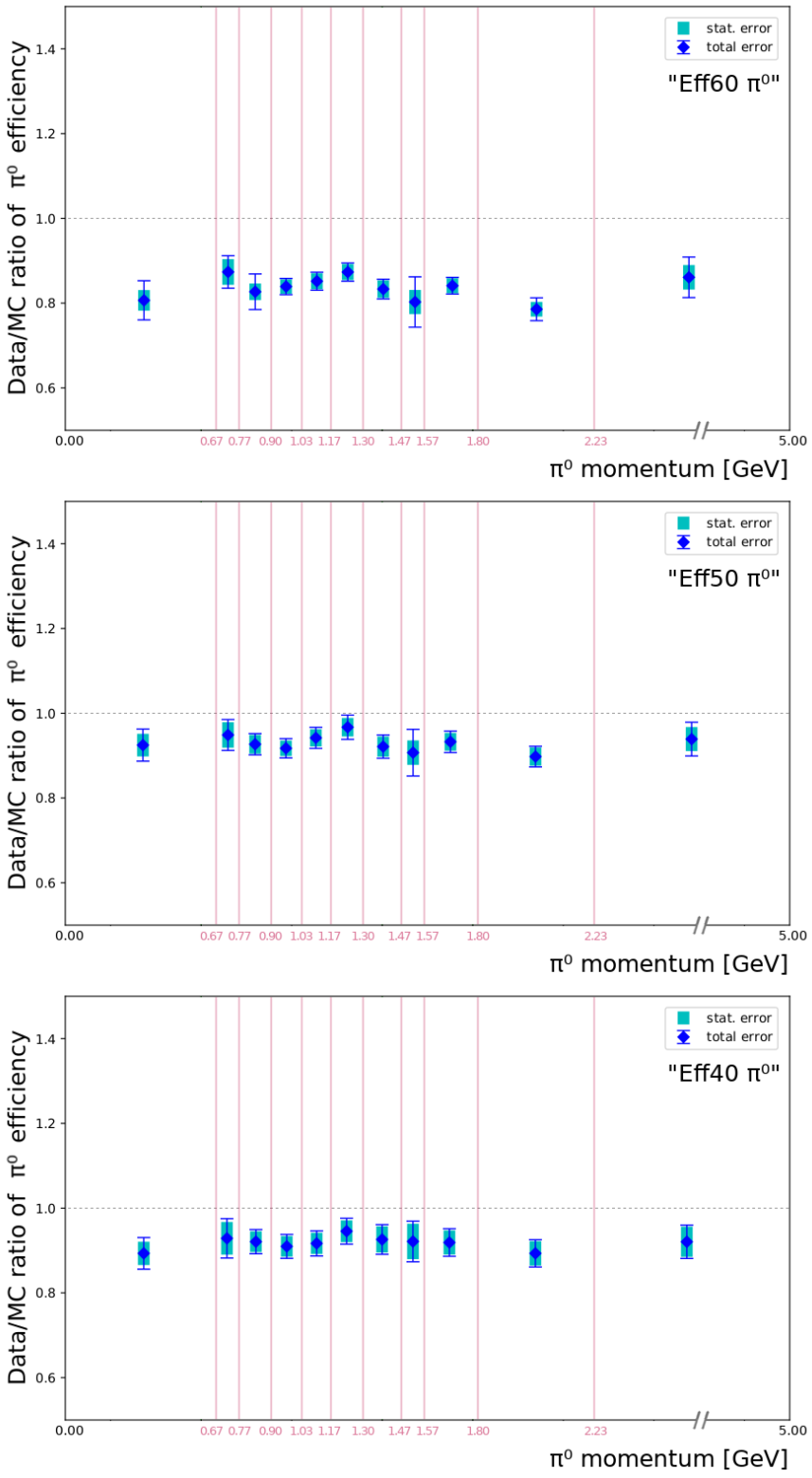

Figure 8.6: *Momentum dependent π^0 reconstruction efficiency correction (ii).* The efficiency correction was calculated in 11 momentum bins, the figure shows the p_{π^0} dependence for "Eff60", "Eff50" and "Eff40" π^0 selections.

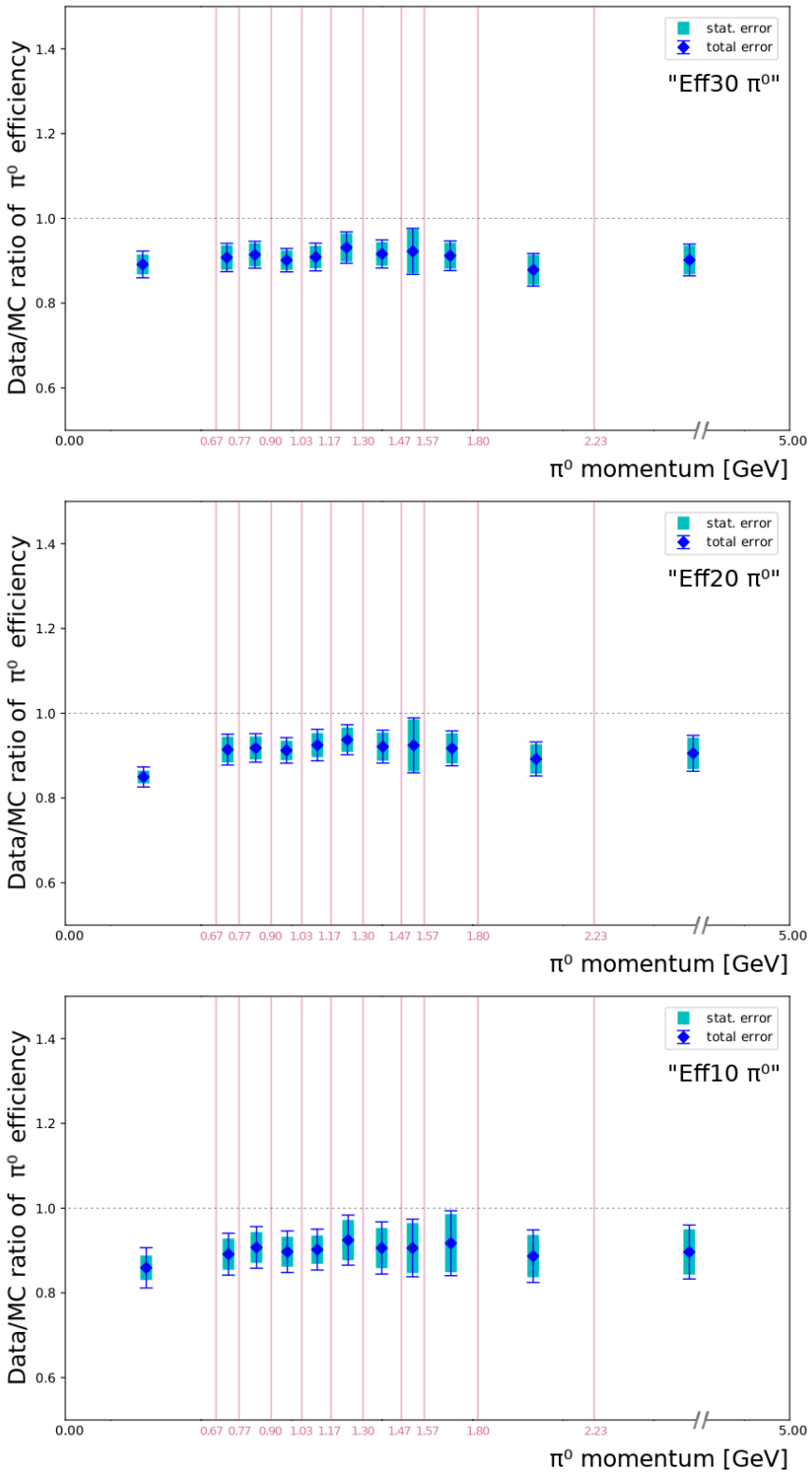

Figure 8.7: *Momentum dependent π^0 reconstruction efficiency correction (iii).* The efficiency correction was calculated in 11 momentum bins, the figure shows the p_{π^0} dependence for "Eff30", "Eff20" and "Eff10" π^0 selections.

9. Optimized π^0 selection

Apart from the eight π^0 selections described in the Chapter 6, another selection based on the "Low" π^0 selection (defined in Tab. 6.1) was developed and optimized, imposing additional requirements on

- the photon energies,
- the angle between the two photons,
- the π^0 momentum,
- the photon timing variables

to suppress the background.

The photon energy is the energy deposit of a photon cluster measured by the ECL. We studied separately the requirements on the energies of the leading and subleading photon within the π^0 candidate photon pair, that is separately for the photon with higher energy, and the photon with lower energy.

The angle between the two photons is the opening angle between the momenta vectors of the photons.

The π^0 momentum is the momentum of the reconstructed π^0 candidate with the highest energy.

Photon timing variables are connected with the time when the photon energy cluster was recorded. The relevant variables will be described further in this chapter.

Among other variables these have been shown to have a discrimination power in separating the signal events from background.

The following section describes the optimisation of the requirements on the previously mentioned variables. The photon timing selection was studied in more detail and the optimization of the timing requirements is described in a separate section.

9.1 Selection requirements

The first part of this section describes the optimization of the requirements on the photon energies, the angle between the two photons and the π^0 momentum. Fig. 9.1 show the data/MC agreement of these distributions, as well as the signal and background MC components.

For the optimization, four different types of events were defined and studied separately.

Fig. 9.2 shows the photon cluster θ angle distributions of the two "LowSB" π^0 photons. The $\theta < 0.55$ range corresponds to forward endcap (FWD), $0.55 < \theta < 2.25$ is barrel section (BRL) and $2.25 < \theta$ is backward endcaps (BWD). It is

evident that the endcaps are more background-dominated than the barrel section and therefore it will be more beneficial to optimize the selections individually for photons in different regions.

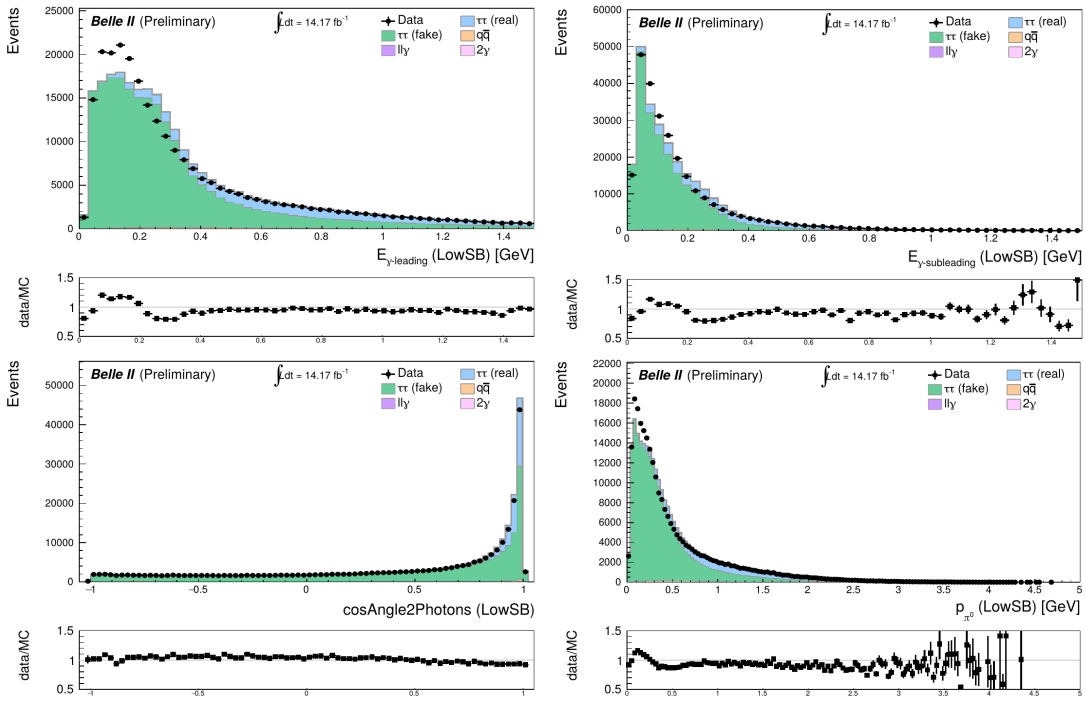

Figure 9.1: *Variables for optimized selections.* This figure shows the distributions of the leading photon energy, the subleading photon energy, the cosine of the angle between the two photons and the π^0 momentum.

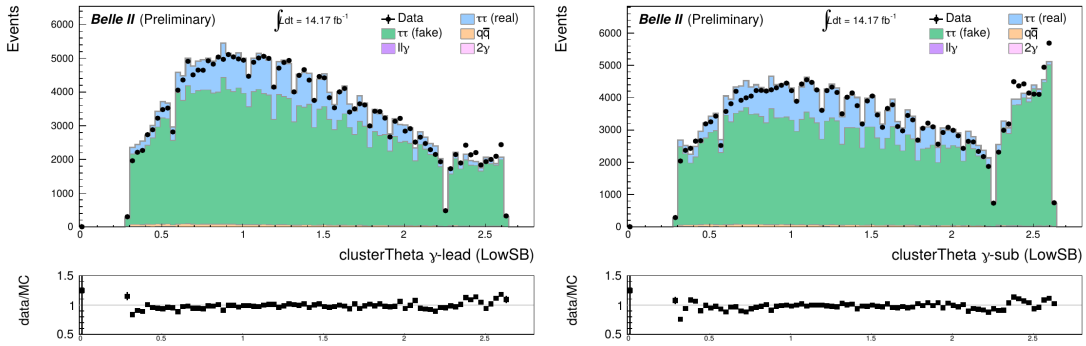

Figure 9.2: *The distribution of the photon cluster θ angle.* The plots show θ angle distributions for leading and subleading photon energy clusters. The $\theta < 0.55$ range corresponds to FWD, $0.55 < \theta < 2.25$ is BRL, $2.25 < \theta$ is BWD.

The following optimization distinguishes events where both π^0 photons were detected in FWD, both in BRL, and both in BWD. The last case covers the events where one of the photons was detected in BWD and the other in was detected in either FWD or BWD. Events where one photon was detected in FWD and other in BWD were also considered but the signal component in such case was negligible and this region was left out from the analysis.

The selections were optimized for the region covering the whole detector as well.

Fig. 9.3 shows the MC distributions of the variables on which the additional requirements were applied on top of the "LowSB" selections, for the whole detector region. The values of the selections were optimized by means of the figure of merit (FOM):

$$\text{FOM} = \frac{s}{\sqrt{s+b}}, \tag{9.1}$$

where s and b are the numbers of signal and background events, respectively. The FOM distribution's maximum corresponds to the best selection for separating signal and background.

Fig. 9.4 compares the $M_{\gamma\gamma}$ distribution of "LowSB" π^0s before and after applying the additional requirements, for the whole detector region.

The optimization plots for the individual regions are shown in Fig. 9.5 - Fig. 9.12 (8 figures).

The values of the additional requirements in each of the considered regions are summarized in Tab. 9.1.

Table 9.1: Optimized selections.

Region	$E_{\gamma-lead}$ [GeV]	$E_{\gamma-sub}$ [GeV]	π^0 cos($\gamma\gamma$ angle)	p_{π^0} [GeV]
whole detector	> 0.3375	> 0.0875	> 0.8792	> 0.6111
γ γ FWD	> 0.5625	> 0.1625	> 0.9458	> 0.9444
γ γ BRL	> 0.4125	> 0.0625	> 0.8875	> 0.6333
γ γ BWD	> 0.4125	> 0.1125	> 0.8708	> 0.6111
γ BRL, γ FWD/BWD	> 0.3625	> 0.0875	> 0.8875	> 0.5889

Before applying the new optimized selections, i.e. for "LowSB" π^0 selection, the efficiency is 45.13% and the purity is 23.43%. After the optimised selections for the whole detector, the efficiency is 26.54% and purity 86.32, while for the region specific selections it is 24.82% and 87.53%.

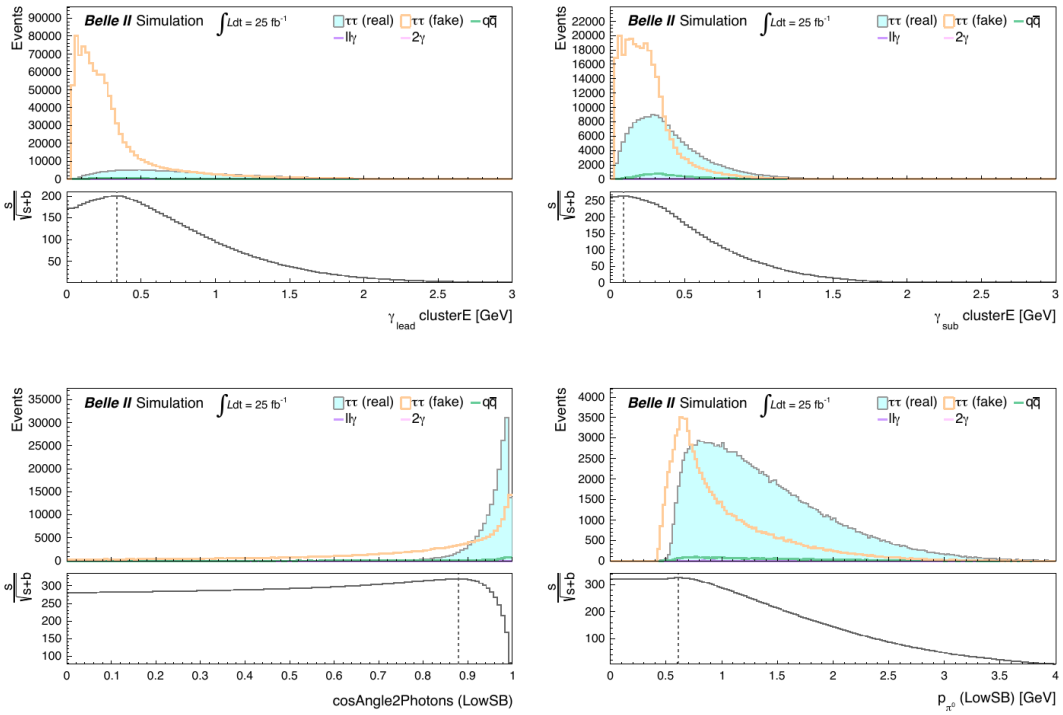

Figure 9.3: *Variables used for the optimization of the selection (whole detector).* The plots show the distributions of variables which were used in the optimized selection, the requirements values are marked with vertical line in the FOM.

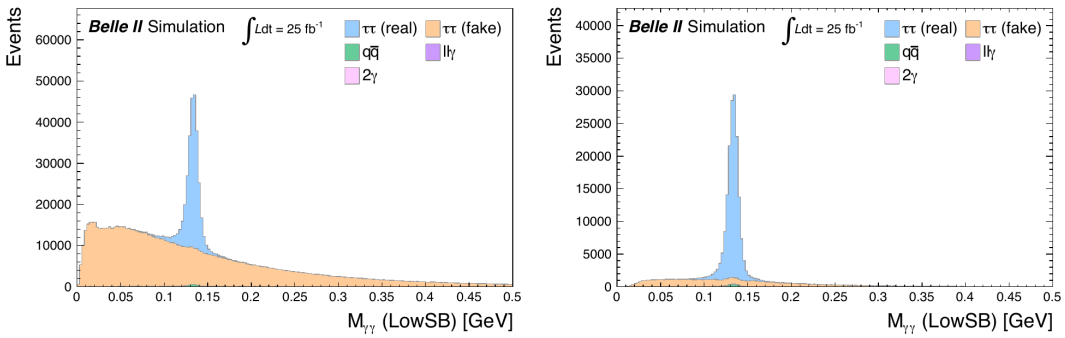

Figure 9.4: *The invariant mass distribution of two photons $M_{\gamma\gamma}$ (whole detector).* The figure compares the $M_{\gamma\gamma}$ distribution of the "LowSB" π^0 for the whole detector region, before and after applying the optimized selections listen in Tab. 6.1.

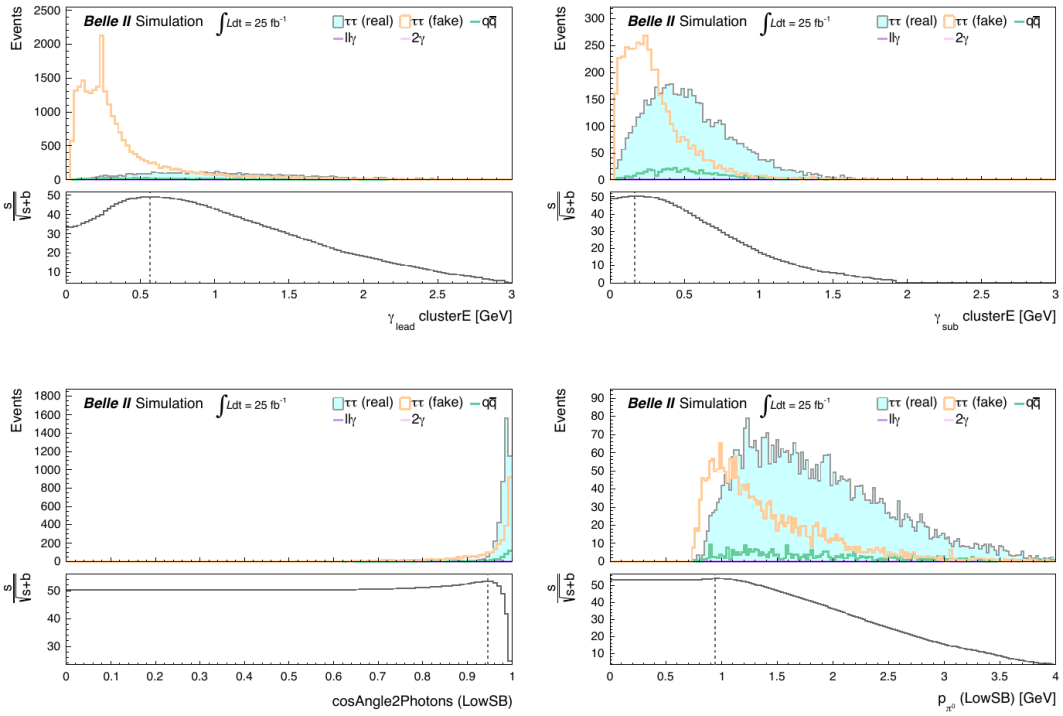

Figure 9.5: *Variables used for the optimization of the selection (FWD).* The plots show the distributions of variables which were used for the optimized selection. The distributions are showing event where both photons were registered in FWD.

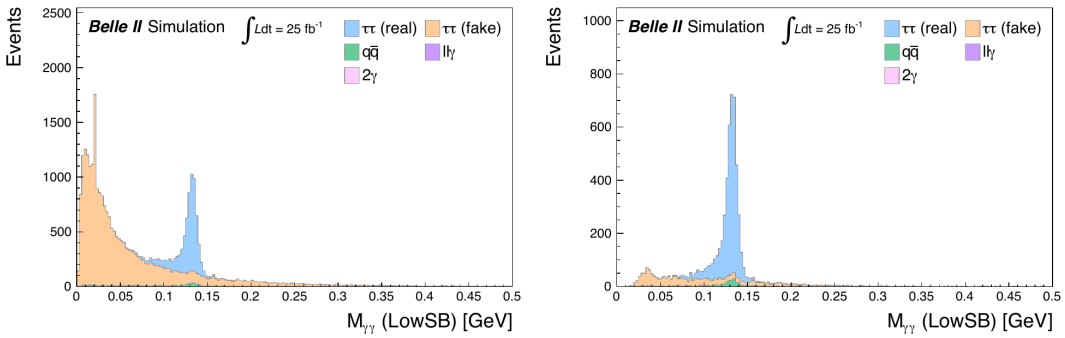

Figure 9.6: *The invariant mass distribution of two photons $M_{\gamma\gamma}$ (FWD).* The figure compares the $M_{\gamma\gamma}$ distribution of the "LowSB" π^0 for the FWD region, before and after applying the optimized selections.

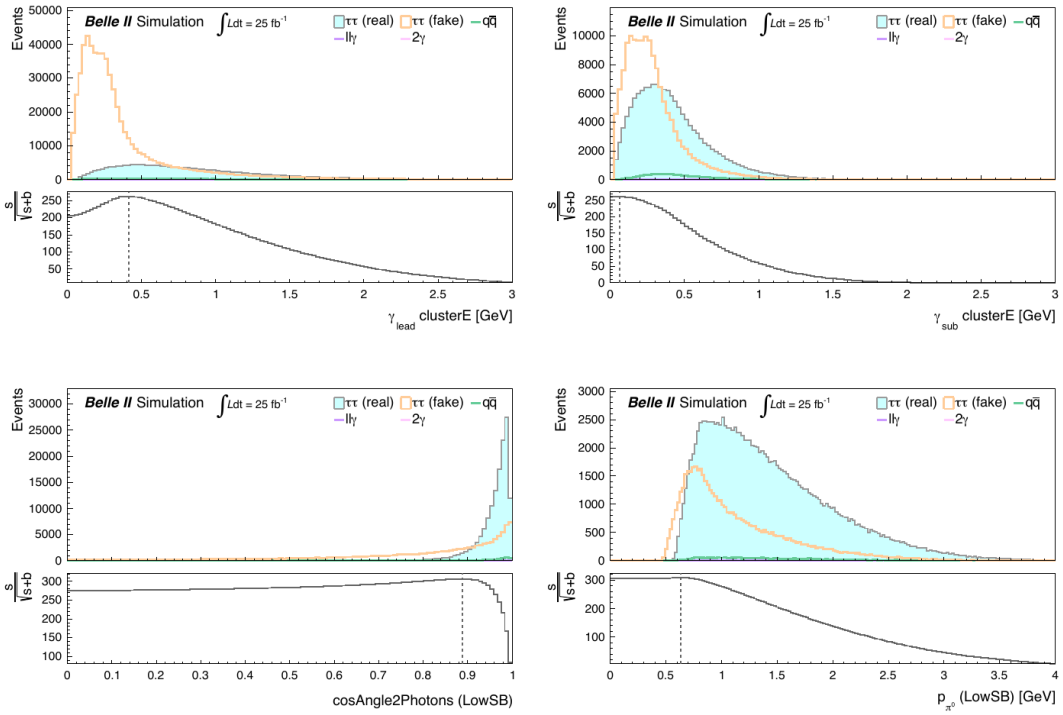

Figure 9.7: *Variables used for the optimization of the selection (BRL).* The plots show the distributions of variables which were used for the optimized selection. The distributions are showing event where both photons were registered in BRL.

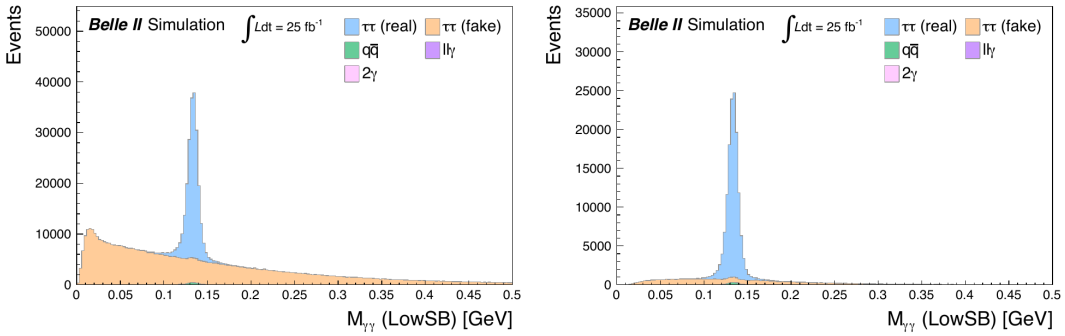

Figure 9.8: *The invariant mass distribution of two photons $M_{\gamma\gamma}$ (BRL).* The figure compares the $M_{\gamma\gamma}$ distribution of the "LowSB" π^0 for the BRL region, before and after applying the optimized selections.

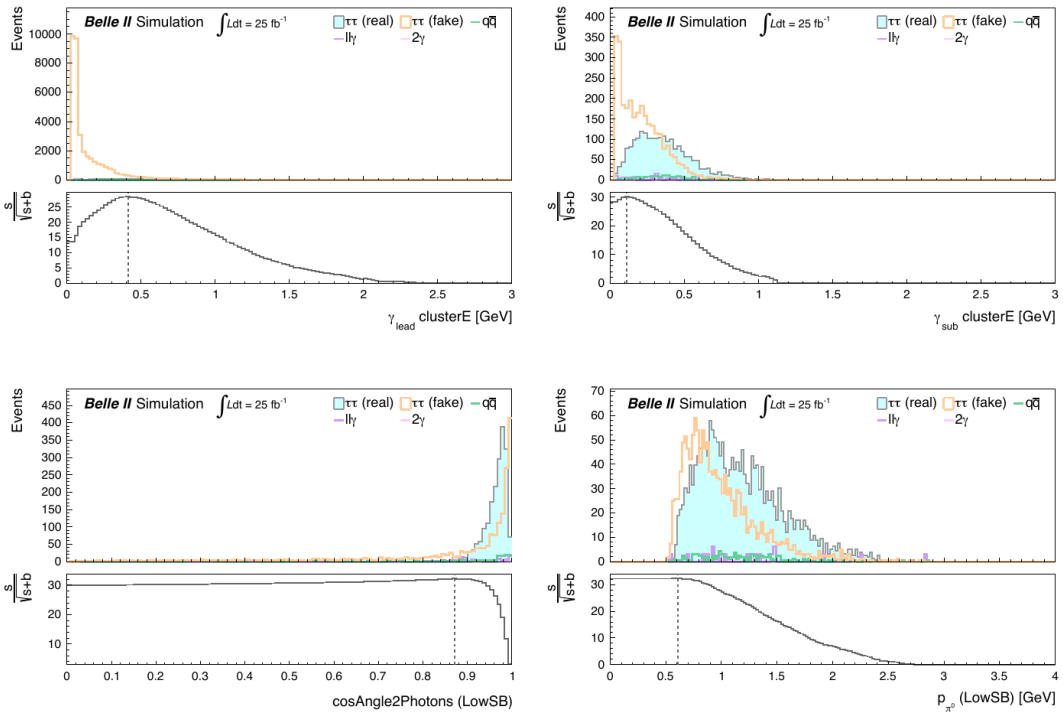

Figure 9.9: *Variables used for the optimization of the selection (BWD).* The plots show the distributions of variables which were used for the optimized selection. The distributions are showing event where both photons were registered in BWD.

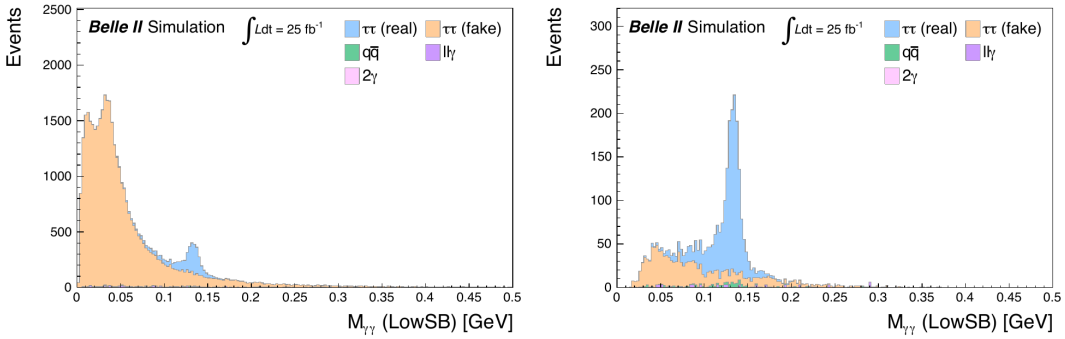

Figure 9.10: *The invariant mass distribution of two photons $M_{\gamma\gamma}$ (BWD).* The figure compares the $M_{\gamma\gamma}$ distribution of the "LowSB" π^0 for the BWD region, before and after applying the optimized selections.

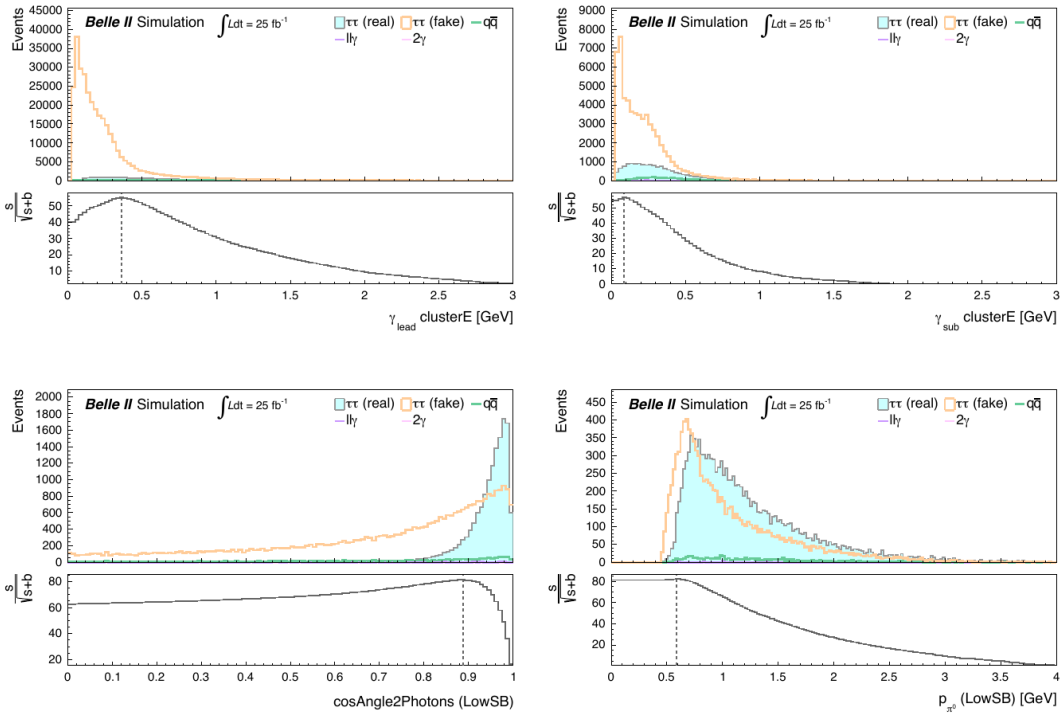

Figure 9.11: *Variables used for the optimization of the selection (BRL + FWB/BWD).* The plots show the distributions of variables which were used for the optimized selection. The distributions are showing event where one photons was detected in BRL and the other in either FWD or BWD.

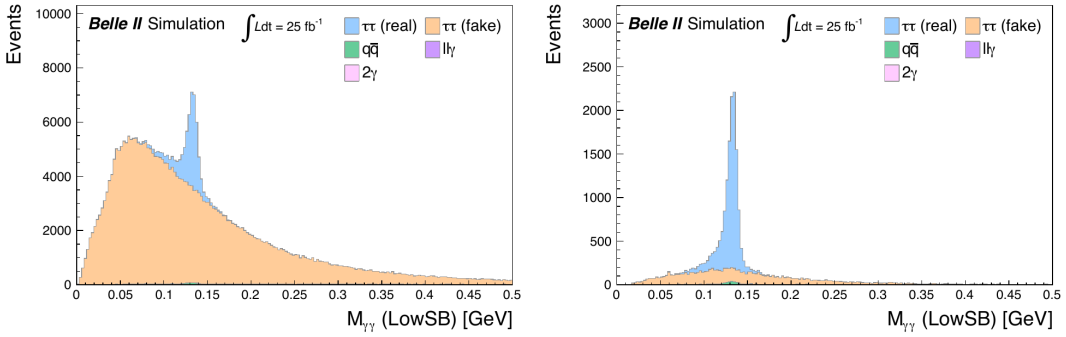

Figure 9.12: *The invariant mass distribution of two photons $M_{\gamma\gamma}$ (BRL + FWD/BWD).* The figure compares the $M_{\gamma\gamma}$ distribution of the "LowSB" π^0 for events where one photons was detected in BRL and the other in either FWD or BWD, before and after applying the optimized selections.

9.2 Photon timing study

Photons are reconstructed from the ECL energy clusters. The photon timing is given by the fitted time of the recorded waveform of the highest energy crystal in the cluster. In MC simulation, out-of-time clusters were not modelled properly in basf2 release-04, see Fig. 9.13. The simulation of photon timing will be improved in release-05 to better match the data, but this will result in significant increase in out-of-time background clusters in MC.

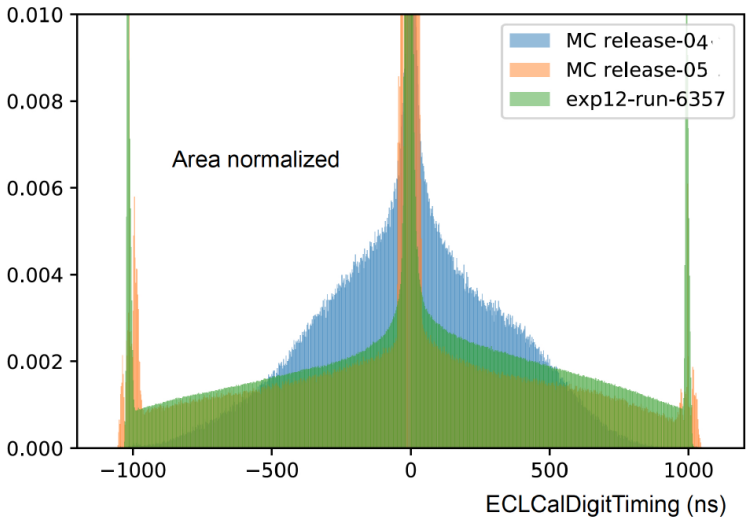

Figure 9.13: *Photon timing simulation.* The blue histogram shows the photon timing distribution simulated with basf2 release-04, the orange histogram is simulation of photon timing in release-05. The green histograms is the measured photon timing distribution from Exp12 data (from one uninterrupted data-taking period called run 6357). The area of each of the histograms is normalized to unity.

Imposing requirements on photon timing can reject these out-of-time clusters from beam backgrounds and thus a good understanding of this variable will become even more important. The results from the study of the photon timing presented in this section are applicable to many Belle II analyses, and currently serve as the official photon timing recommendations from the Belle II Neutrals Performance Group.

9.2.1 Efficiency and purity

The usefulness of imposing requirements on photon timing was judged according to the impact on the selection efficiency and the purity of the sample.

The efficiency was compared using the number of signal events before and after applying increasingly tighter timing requirements. The number of signal was estimated from the fit of the π^0 mass distribution, using the same procedure described in Chapter 7. The model function for the timing study fits was a Crystal Ball for the peak and a 3rd order Chebyshev polynomial for the background.

The purity was calculated according to Eq. 6.3.

9.2.2 clusterTiming

Two types of photon timing selections were studied. The first approach was to apply a threshold on the photon cluster timing itself (clusterTiming). The distributions of the photon timing are shown in Fig. 9.14 and 9.15, both for the leading and subleading π^0 photon. As was mentioned earlier in this section, more very out-of-time clusters are present in the data compared to MC, originating from the beam background photons. The excess of the data over MC in the tails of the photon timing distributions is clearly visible in the log-scale plots in Fig. 9.14 and 9.15.

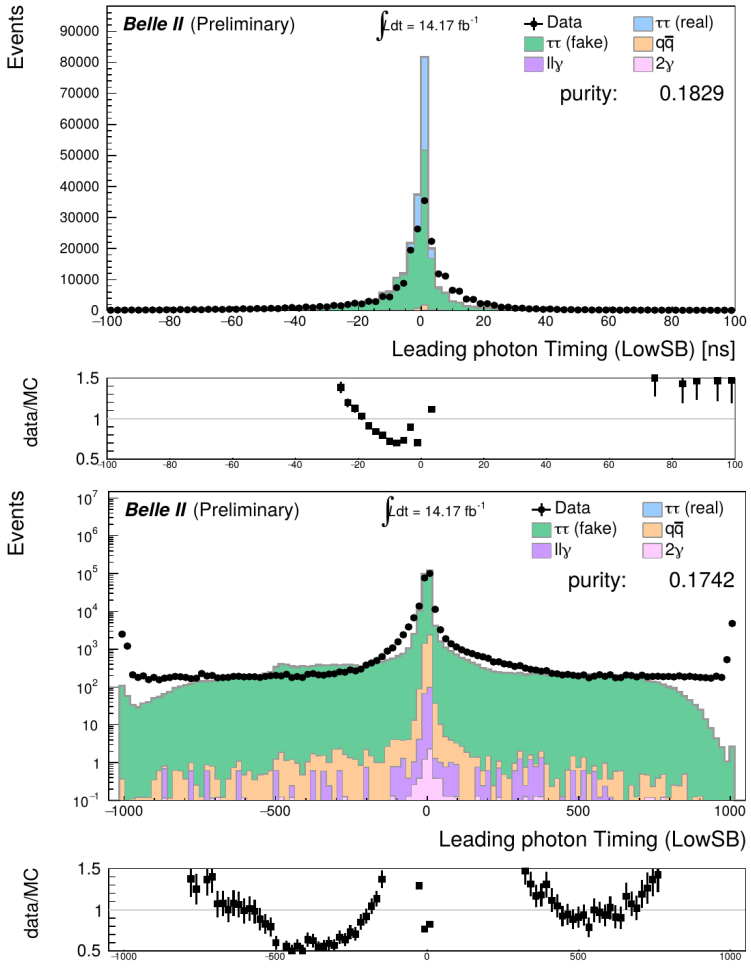

Figure 9.14: *Leading photon timing distribution.* The top plot shows narrow range around the peak, the bottom plot contains the full distribution in log y-axis scale.

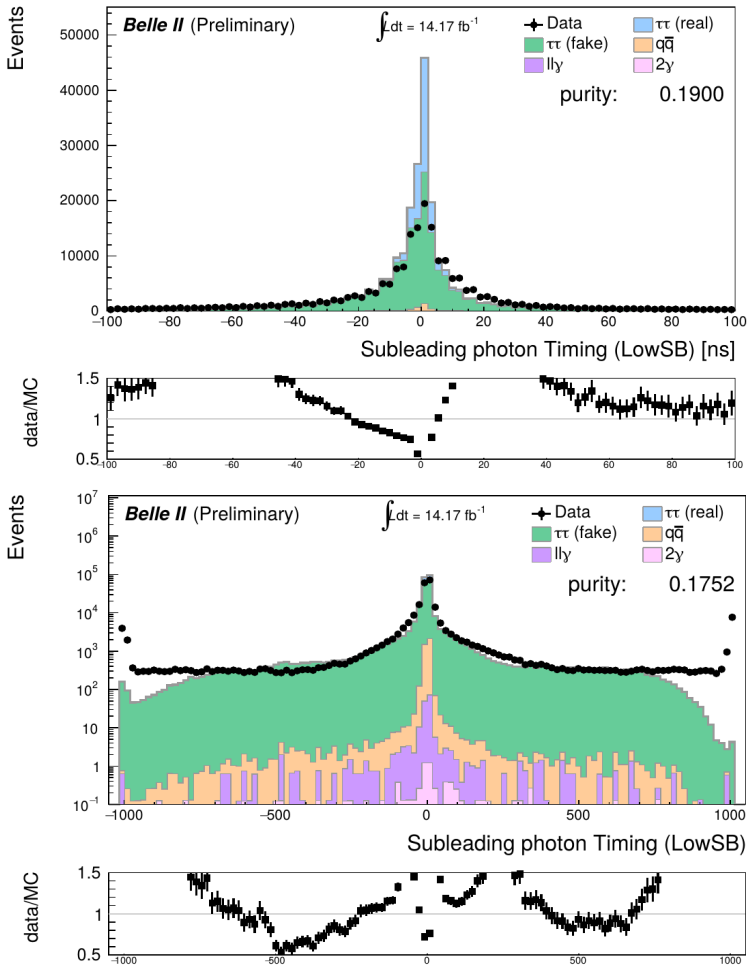

Figure 9.15: *Subleading photon timing distribution.* The top plot shows narrow range around the peak, the bottom plot contains the full distribution in log y-axis scale.

The following set of thresholds on the absolute value of the photon timing were studied:

$$|\text{clusterTiming}| < \{500, 400, 300, 250, 200, 150, 100, 50, 40, 30, 20, 10\}\text{ns}. \quad (9.2)$$

The purity and the number of signal events after each of the cluster timing selections in data and MC is shown in Fig. 9.17. The plots of the fitted π^0 mass distributions can be found in Appendix B.5. The same requirement was simultaneously applied on both the leading and subleading π^0 photon. The plots in Fig. 9.16 show that the signal is contained in a symmetrical region with respect to the two photons' variables.

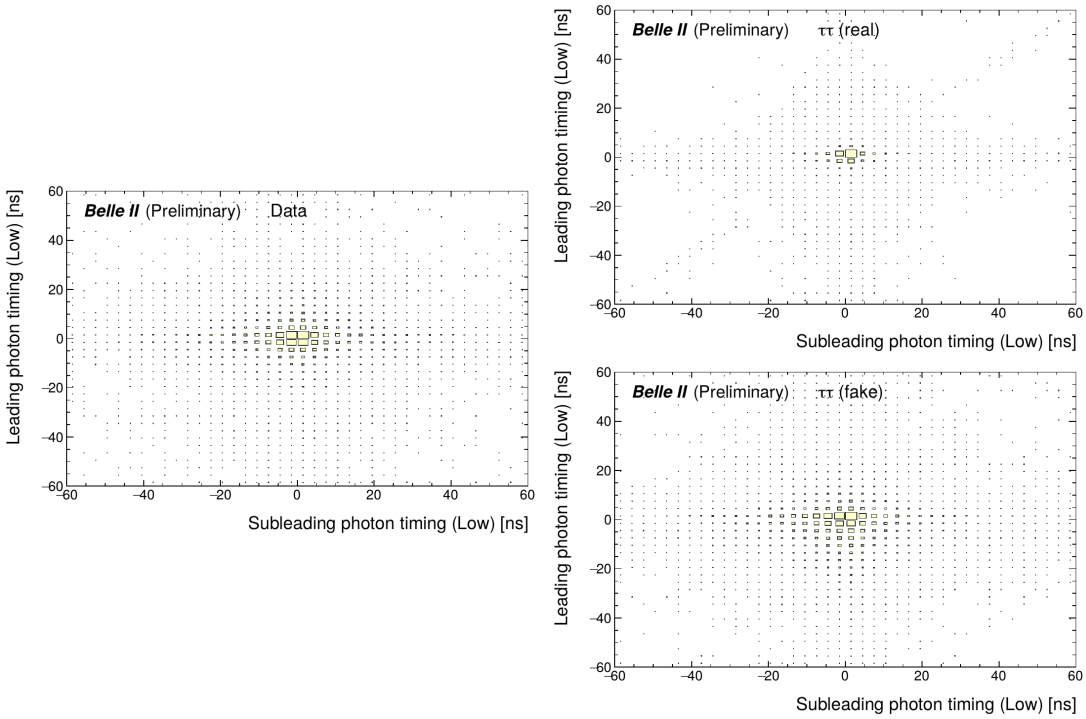

Figure 9.16: *2D plot of photon timing.* The plot on the left shows the correlation between leading photon cluster timing and subleading photon cluster timing in data. The plots on the right show the correlation in MC, for "$\tau\tau$ (real)" and for "$\tau\tau$ (fake)" components.

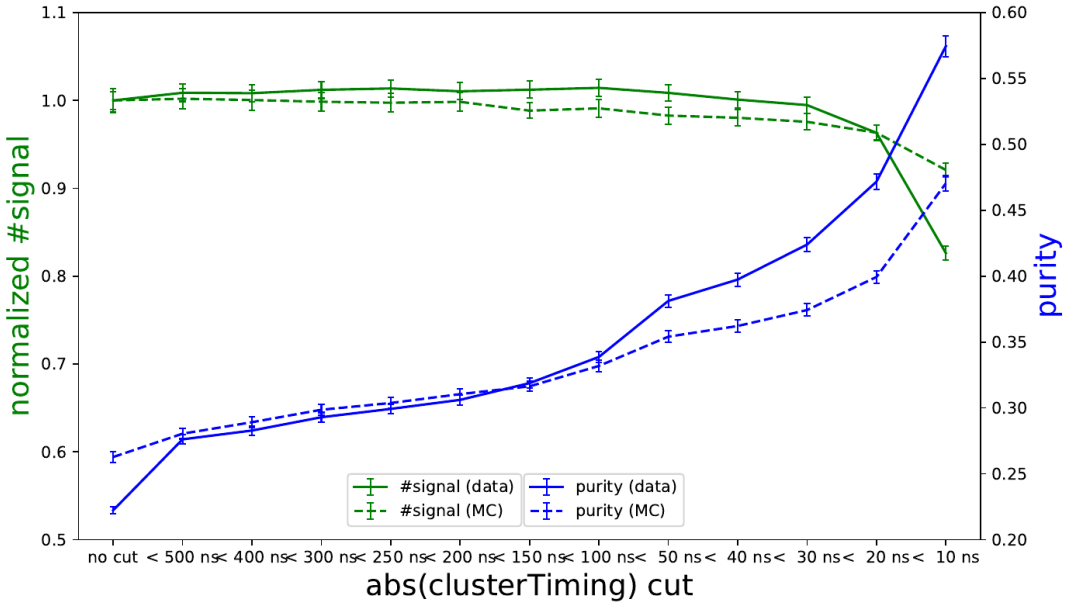

Figure 9.17: *Scan of the absolute timing selection.* The plot shows the purity and number of signal events in data (solid lines) and MC (dashed lines) after imposing different timing requirements. The number of signal events is normalized with respect to the first data point where no timing selection was applied. Uncertainties are statistical only.

9.2.3 clusterTiming/clusterErrorTiming

In addition to clusterTiming, we also studied the value of its associated error (clusterErrorTiming). The photon clusterErrorTiming is the ECL cluster's timing uncertainty that contains 99 % of the true photons and it is currently determined using MC. The timing ratio, defined as clusterTiming/clusterErrorTiming, is designed to give a 99% efficiency for true photons from the IP after requiring |clusterTiming/clusterErrorTiming| < 1. Due to the short lifetimes of the τ leptons and π^0s, the signal photons in this study are essentially coming from the IP.

The distributions of clusterErrorTiming and clusterTiming/clusterErrorTiming are shown in Fig. 9.18.

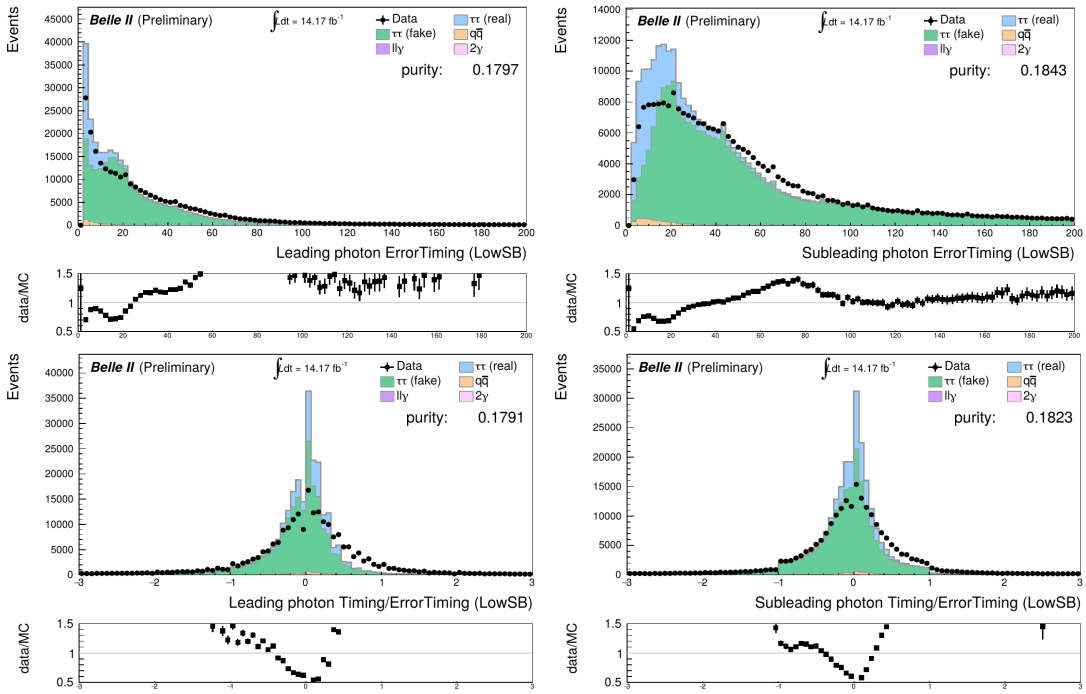

Figure 9.18: *Photon timing error and timing ratio distributions.* The top plots show the distribution of photon clusterErrorTiming, while the bottom plots show the clusterTiming/clusterErrorTiming distribution.

The studied values of the threshold for the timing ratio are the following:

$$|\text{clusterTiming/clusterErrorTiming}| < \{2.5, 2.0, 1.5, 1.0, 0.5\}. \tag{9.3}$$

The purity and the number of signal events in data and MC for the timing ratio selection is shown in Fig. 9.20. Fitted π^0 mass distributions can be found in Appendix B.5. The selection was applied to both the leading and subleading π^0 photon simultaneously. Similarly as for the photon timing, the photon timing ratio distribution for the signal is distributed symmetrically with respect to the two photons' variables, see Fig. 9.19.

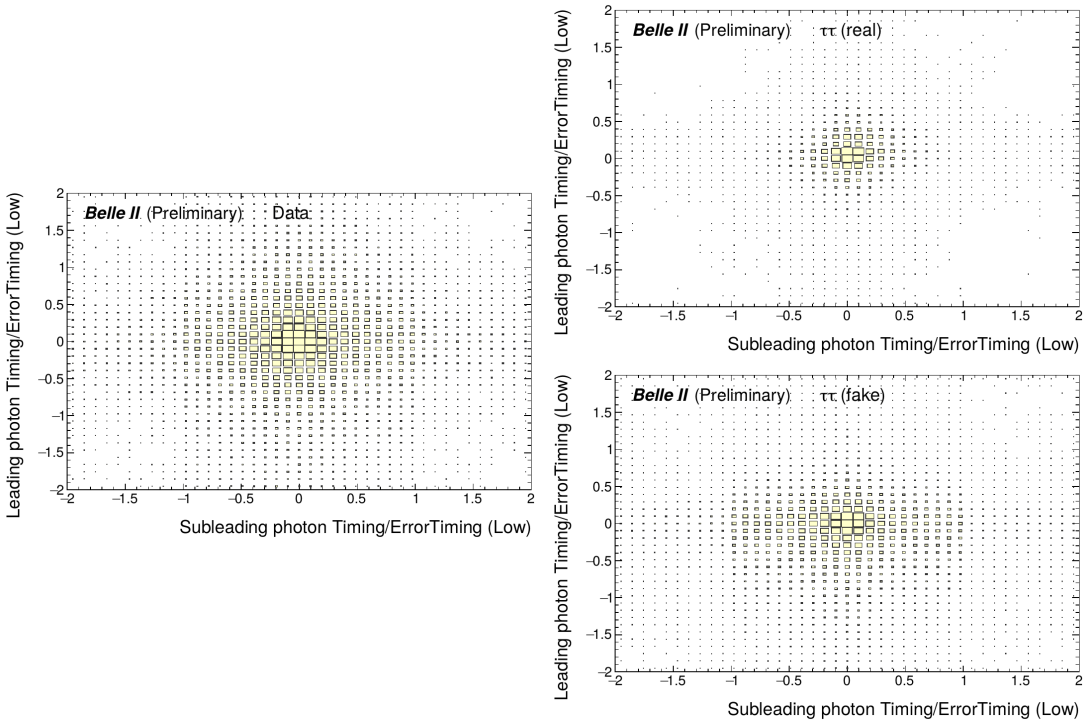

Figure 9.19: *2D plot of photon timing ratio.* The plot on the left shows the correlation between cluster timing ratio of leading and subleading photon in data. The plots on the right show the correlation in MC, for "$\tau\tau$ (real)" and for "$\tau\tau$ (fake)" components.

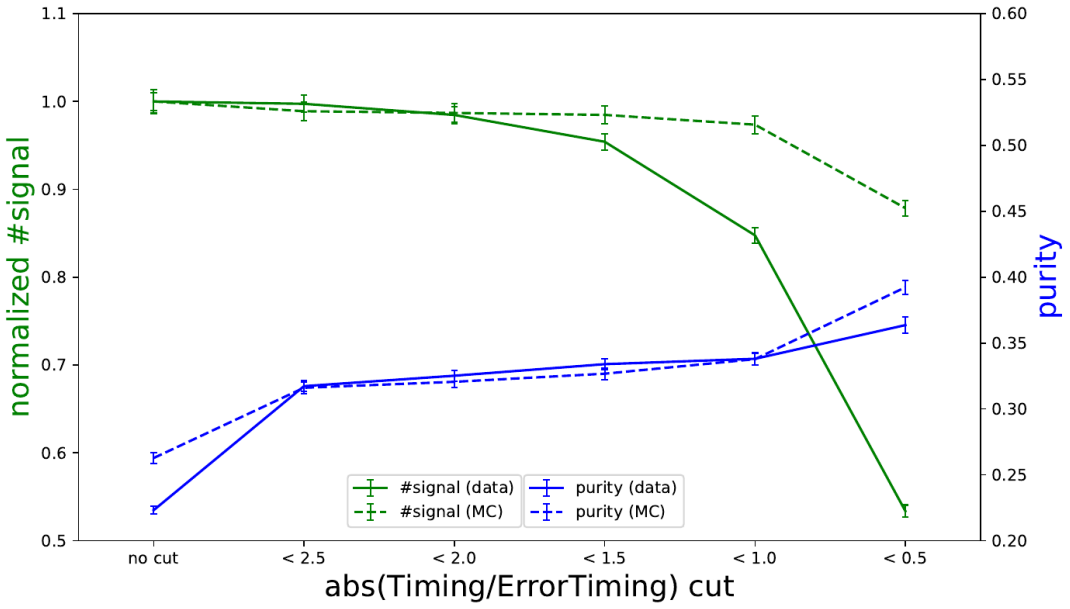

Figure 9.20: *Scan of the absolute timing ratio selection.* The plot shows the purity and number of signal events in data and MC after imposing different requirements on the timing ratio. The number of signal events is normalized with respect to the first data point where no timing selection was applied. Uncertainties are statistical only.

9.2.4 Recommendations

Based on the results shown in the previous subsections, the recommended photon timing selections were determined as the following conditions:

- *Loose timing selection*: abs(clusterTiming) < 200 ns
- *Tight timing selection*: abs(clusterTiming) < 200 ns *and* abs(clusterTiming/clusterErrorTiming) < 2.0

The chosen values reject the out-of-time clusters while maintaining good data/MC agreement. The *tight timing selection* further increases the purity of the sample by rejecting additional background photons. This is illustrated in Fig. 9.21 which shows the photon timing distribution after applying the condition on the timing ratio. The timing ratio requirement does not reject all of the photons with |clusterTiming| > 200 ns, and so imposing thresholds on both variables simultaneously resulted in the best background photon rejection.

Fig. 9.22 shows the subleading photon energy distribution comparison before and after applying the recommended selection, displaying only the MC signal component. It can be seen from the ratio plots below the distributions that the imposed requirements has only a negligibleimpact on the signal efficiency.

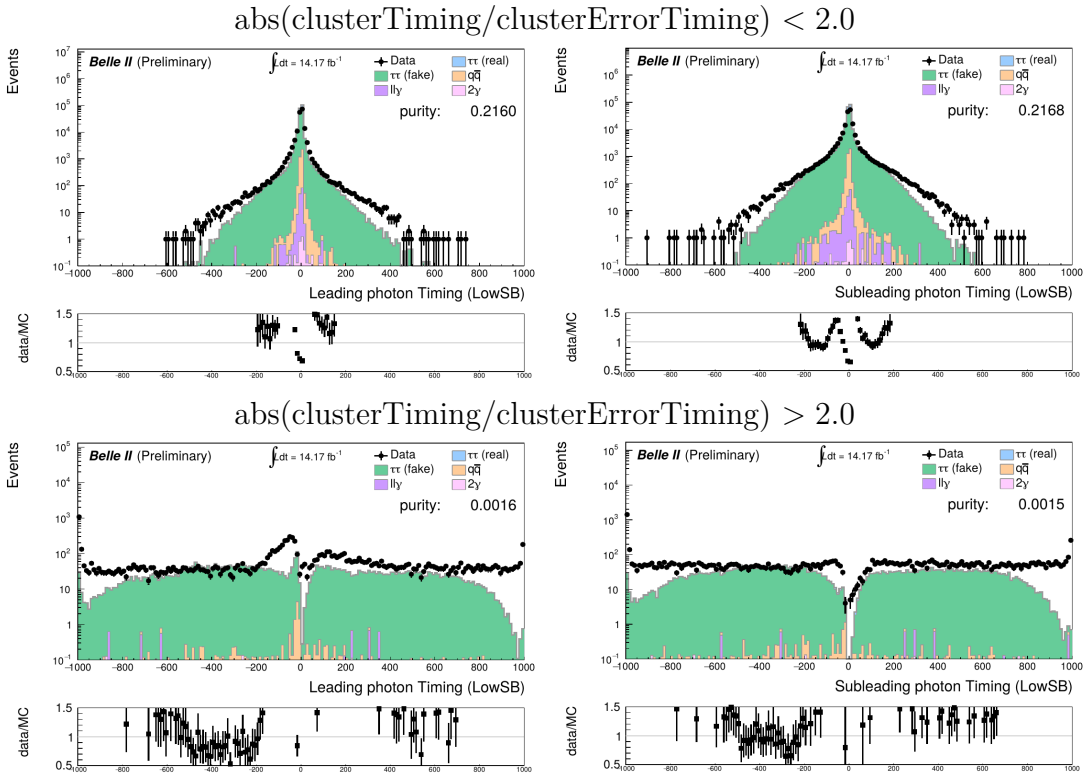

Figure 9.21: *Timing distribution after timing ratio selection.* The top plots show the photon timing distribution after applying the condition abs(clusterTiming/clusterErrorTiming) < 2.0. The bottom plots show timing distribution for the photons that are rejected by applying this condition.

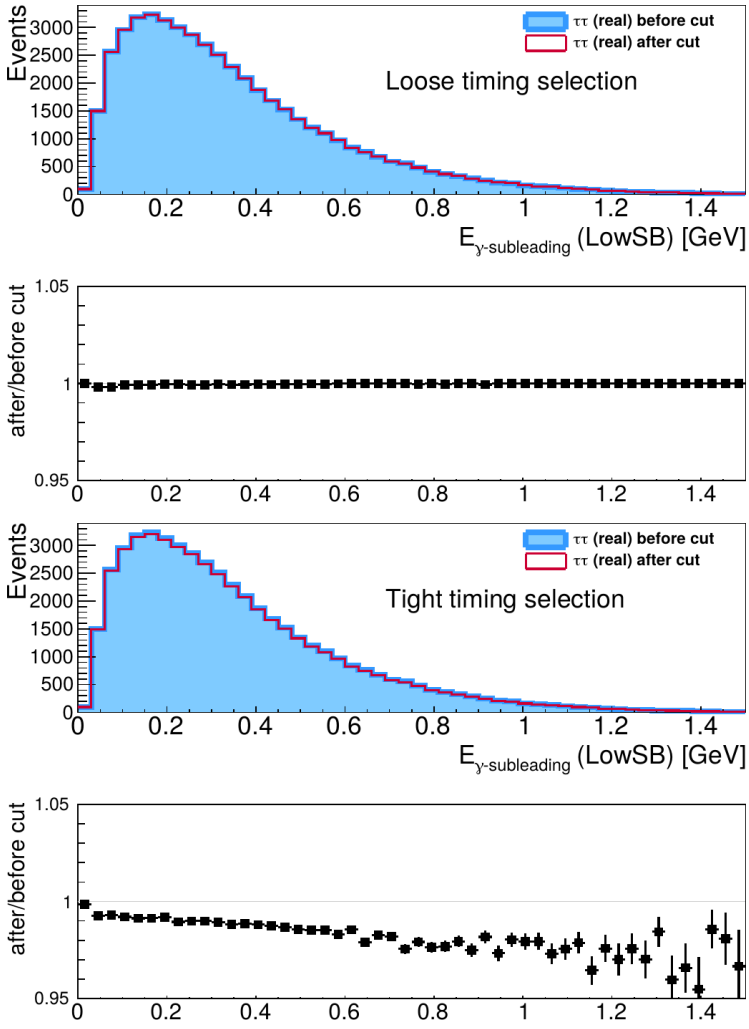

Figure 9.22: *Subleading photon energy distribution.* The plots show the subleading photon energy distribution of the signal MC component, comparing the distributions before and after applying the recommended photon timing selections.

10. Discussion

The aim of this chapter is to give a wider context to the obtained results and to propose further studies.

10.1 Comparison with π^0 study with B decays

The results on the π^0 efficiency correction obtained from the study presented in this thesis are compared to a similar measurement performed by T. Koga, A. Selce and S. Stengel at Belle II prior to this analysis. In their analysis, π^0 from B meson decays were used. More information about the study and its main results are summarized in Appendix A.3.

Fig. 10.1 compares the results on the π^0 efficiency correction measured in τ decays with the results from the study with B decays. The comparison is available for the "Eff50", "Eff40", "Eff30", "Eff20" and "Eff10" π^0 selections.

The results of the two independent measurements are in agreement within the uncertainties. The difference in the statistical precision might be partially explained by analysing more data but also by reconstructing more π^0s in the τ decays compared to the B meson sample.

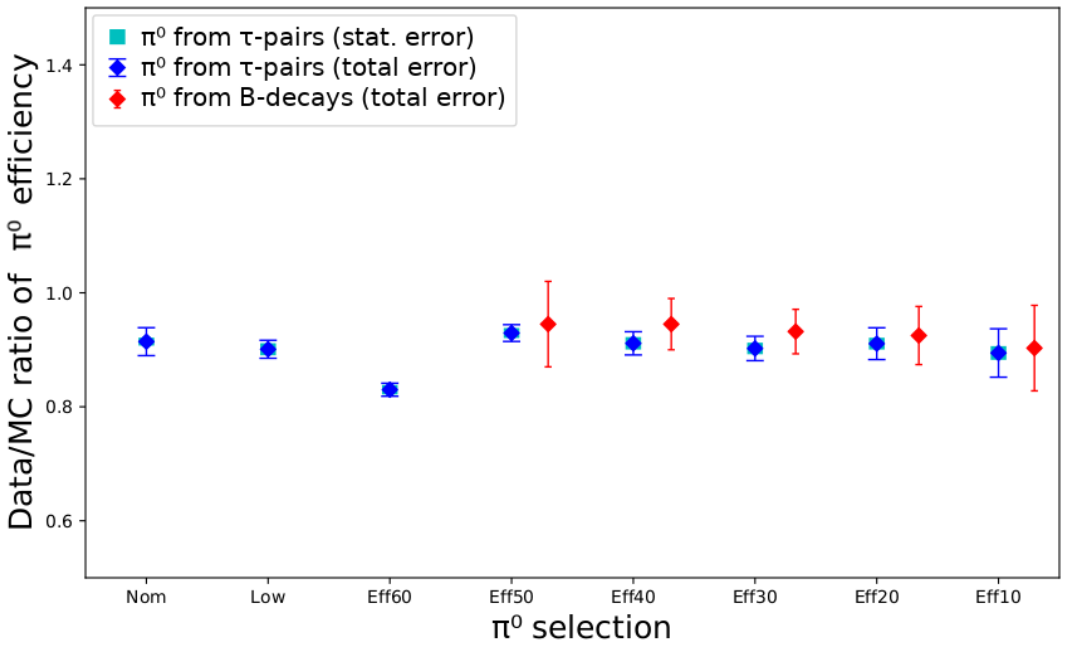

Figure 10.1: π^0 *efficiency correction from* τ *decays and* B *decays.* The plot shows the results from our τ lepton study (blue) compared with results from π^0 study with B decays (red). The statistical and systematic uncertainties for the B-decay study results are listed in Appendix A.2.

The comparison was also made for momentum dependent π^0 efficiency correction, with the results for the "Eff50" π^0 selection shown in Fig. 10.2. The study on momentum dependent π^0 efficiency correction from B and D decays was performed

by T. Koga and is summarized in Appendix A.4. The momentum dependence of the correction measured in τ decays is relatively flat around 0.96 showing no strong dependence on the π^0 momentum. The π^0 efficiency correction obtained from B and D decays is above 1 for higher momentum π^0s bins and drops down to 0.9 for momentum around 0.5 GeV. The reason for the discrepancy between the two measurements is still not understood and is under the investigation.

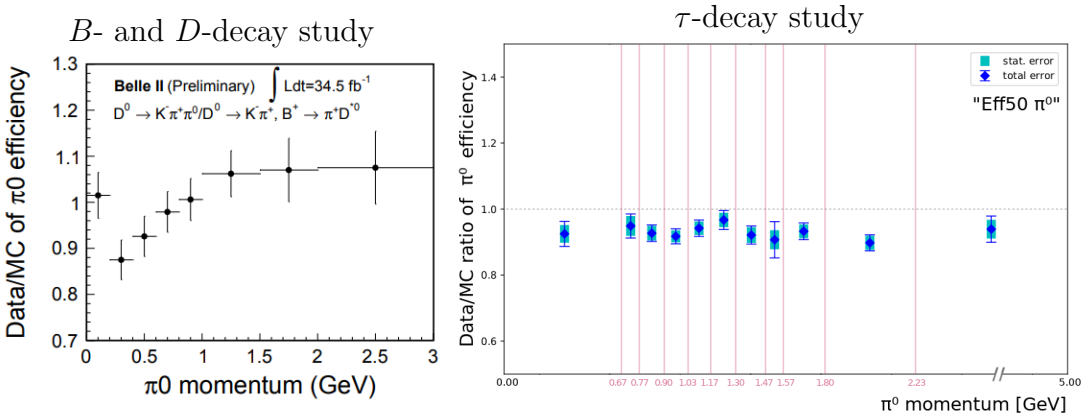

Figure 10.2: *Momentum dependent correction from τ decays and B decays.* The figure compares the result on momentum dependent π^0 reconstruction efficiency correction for "Eff50" π^0 selection as measured in τ decays and B decays. More details about the measurement with B decays can be found in Appendix A.4.

10.1.1 Next steps

Apart from π^0 momentum dependence, the correction can be examined as a function of the θ angle of the π^0. As was discussed in Chapter 9, the signal/background ratio can differ in the different detector regions and the knowledge of the angular dependent correction may be important and useful. Given enough statistics, the efficiency correction could be determined in 2D bins of the π^0 momentum and the θ angle.

The method of measuring the π^0 efficiency correction in the τ decays was developed for 3x1-prong decays but it could also be used for 1x1-prong decays. The backgrounds will be larger in such analysis, but due to larger cross sections of $\tau \to \pi\pi^0\nu$ and $\tau \to \pi 2\pi^0\nu$ (see Fig. 1.2) it could benefit from higher statistics.

10.2 New π^0 selections

Using the results of the optimization described in Chapter 9, four new π^0 selections are defined in Tab. 10.1. This table summarizes the requirements for the "InclOpt", "Opt", "OptLoose" and "OptTight" selections, the exact values are listed in Tab. 9.1 with the photon timing selections defined in Section 9.2.4.

Tab. 10.2 compares the purities and efficiencies of the eight π^0 selections described in Chapter 6 and the selections defined above. While the purity of the "Nom"

Table 10.1: New π^0 selections based on the "Low" selection.

Additional requirement	"InclOpt"	"Opt"	"OptLoose"	"OptTight"
$E_{\gamma-lead}$ [GeV]				
$E_{\gamma-sub}$ [GeV]	same values for	different values	different values	different values
π^0 cos(3D $\gamma\gamma$ angle)	whole detector	for each region	for each region	for each region
p_{π^0} [GeV]				
photon timing	-	-	*Loose selection*	*Tight selection*

selection, which is currently used in the Belle II τ analyses, is around 55 %, the purity of the newly optimized selections is higher by more than 30 %. The efficiency of the new selections matches the "Nom" π^0 efficiency.

Table 10.2: Purity and efficiency.

	"Eff60"	"Eff50"	"Eff40"	"Eff30"	"Eff20"	"Eff10"
efficiency (%)	59.82	49.82	39.93	29.84	19.81	9.81
purity (%)	2.49	10.87	18.82	29.78	50.03	69.25

	"Nom"	"Low"	"InclOpt"	"Opt"	"OptLoose"	"OptTight"
efficiency (%)	25.69	45.13	26.54	24.82	24.80	24.47
purity (%)	55.42	23.43	86.32	87.53	87.84	88.13

The new selections have a good suppression of the π^0 fakes, which are mainly in the low momentum region (see Fig. 10.3). Next steps would be to try to improve the π^0 efficiency, particularly at low momentum, while maintaining the current level of high purity. For this purpose it could be beneficial to employ machine learning techniques.

10.2.1 Selection validation

The main goal of this optimization is to develop a new π^0 selection which would give the best results for τ lepton analyses, and will become the default π^0 selection used within the Belle II Tau Physics Group.

The Tab. 10.2 show the efficiency and purity of the new selections measured within the 3x1-prong τ-pair events study. The selection "OptLoose" has already been used in an independent measurement of the τ electric dipole moment (EDM) in 1x1-prong τ decays, and the improvement compared to using the "Nom" selection was also significant.

The next step in the validation process would be to measure the π^0 reconstruction efficiency correction for these new considered selections.

Many physics analyses need to veto rather than select the π^0s. Another possible continuation of this study would be to optimize a π^0 selection that performs the best for a π^0 veto.

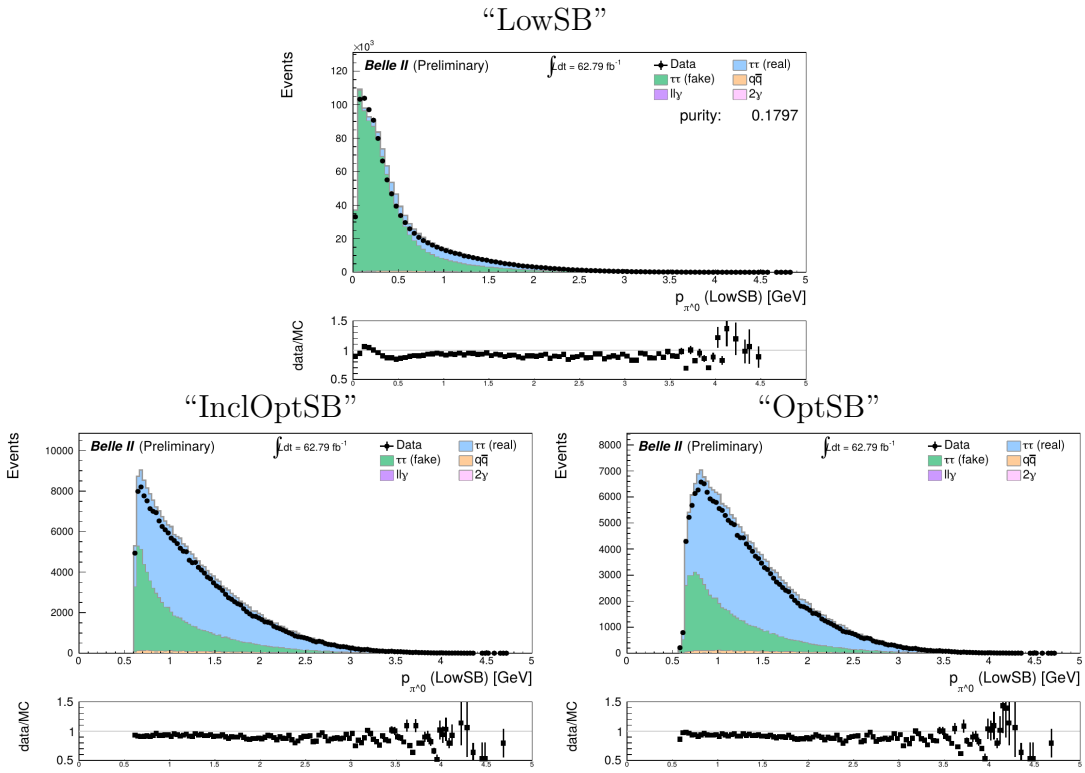

Figure 10.3: p_{π^0} *after optimized selections.* The plots show the π^0 momentum distribution for "LowSB", "InclOptSB" and "OptSB" π^0 selections.

10.3 Photon timing recommendations

The photon timing selection presented in Section 9.2.4 were determined for photons detected anywhere in the ECL. The different detector regions (defined in Chapter 9) were examined as well but there was not enough statistics in some regions, and so it was not possible to perform the fit of the π^0 mass distribution. This study was finalized before being granted the permission to work with the full Exp12 dataset. Using the full available data will enable the optimization of the timing selections in different ECL regions and improve both the efficiency and purity of the selection.

Another improvement could be achieved by fitting the π^0 mass peak with double Gaussian in the same way as it was done in the π^0 efficiency correction study.

10.3.1 New software release

As was mentioned in Chapter 9, the modelling of the photon cluster timing will improve in the upcoming release of the simulation software. The simulation of the photon cluster timing error will improve as well. The photon timing study can be then repeated with the newly simulated MC samples and the recommendations may be improved without introducing data/MC discrepancy.

Conclusion

This thesis presented a study of τ lepton decays measured at the Belle II experiment, and the main goal was to determine the π^0 reconstruction efficiency correction.

The review part of this thesis gave an overview of the SM and the Belle II experiment, its detector and the simulation software. The next sections described the τ-pair events at Belle II and explained the method used for measuring the π^0 reconstruction efficiency correction.

The central part presented the analysis procedure, describing the signal event selection, defining important variables, comparing the measured and simulated data and showing the extracted signal yields.

The results comprised the measured values of the π^0 efficiency corrections and their uncertainties. These efficiency corrections are essential for many Belle II physics analyses. Eight different π^0 selections were studied and the measurement was performed for each of the working points. The efficiency correction was also measured as a function of the π^0 momentum and the results were compared with an independent measurement from B and D decays. The momentum dependent results allow for using the correction in other Belle II physics analyses where the energy spectrum of reconstructed π^0 is different than in the samples studies in this analysis.

Another result of this study was the development of a new set of π^0 selections that were optimized for π^0s produced in τ decays. A set of variables with a discrimination power in separating the signal from background was identified and imposing additional requirements on these variables yielded a π^0 sample with significantly higher purity. This π^0 selection is currently being used in several τ physics analyses, and is expected to become the default selection of the Tau Physics Group within Belle II.

A dedicated study was conducted on the photon timing selection requirements. The photon timing modelling will improve in the next release of the simulation software, and it will be even more important to reject the out-of-time ECL photon clusters. Based on the results of this analysis, the photon timing selection recommendations were proposed to reject the fake photon candidates, and the selections are now commonly used within the Belle II collaboration.

The progress and the results of these studies were regularly presented at the Belle II Tau Physics and Neutrals Performance Group meetings as well as at the Belle II General Meeting (B2GM) which took place in January/February 2021.

The continuation of this study will focus on measuring the dependence of the π^0 correction on the polar angle (θ) which will enable a deeper understanding of the detector performance, and provide Belle II analysts with an even more precise correction to the π^0 efficiency.

The new π^0 selection will be further improved, the corresponding correction factors will be measured, and then introduced to the Belle II Tau Physics Group. An alternative selection criteria may be optimized in order to veto the π^0s, which

would benefit τ physics analyses where the signal has no π^0s in the final state.

The photon timing study will be redone with the new MC samples where the simulation of the photon timing variables will improve. The analysis should confirm the usefulness of the recommended selection, and further improvements to the fake photon suppression may be developed.

Bibliography

[1] Kobayashi, Makoto. *CP violation and flavour mixing.* Nobel Lecture. https://www.nobelprize.org/uploads/2018/06/kobayashi_lecture.pdf.

[2] Maskawa, Toshihide. *What does CP violation tell us?* Nobel Lecture. https://www.nobelprize.org/uploads/2018/06/maskawa_lecture.pdf.

[3] The BaBar Collaboration. *The* BaBar *Detector: Upgrades, Operation and Performance.* π^0 efficiency correction (pages 94-96). arXiv:1305.3560 [physics.ins-det].

[4] Glashow, S. L. *Partial-symmetries of weak interactions.* Nucl. Phys., vol. 22, issue 4 (1961).

[5] Weinberg, S. *A Model of Leptons.* Phys. Rev. Lett. 19, 1264 (1967).

[6] Salam, A. *Elementary Particle Theory.* Almquist and Wiksell, 1968.

[7] Glashow, S. L., Iliopoulos, J., Maiani, L. *Weak Interactions with Lepton-Hadron Symmetry.* Phys. Rev. D 2, 1285 (1970).

[8] MissMJ, *Standard model of elementary particles* [online]. [cit. 23/04/21]. https://commons.wikimedia.org/wiki/File:Standard_Model_of_Elementary_Particles.svg.

[9] Drexler, Eric. *Elementary particle interactions in the Standard Model* [online]. [cit. 23/04/21]. https://commons.wikimedia.org/wiki/File:Elementary_particle_interactions_in_the_Standard_Model.png.

[10] Tanabashi, M. et al. (Particle Data Group) *Review of particle physics.* (pages 36, 41). Phys. Rev. D 98, 030001 (2018).

[11] Authors own work.

[12] Doležal, Z., Uno, S. et al. *Belle II Technical Design Report.* arXiv:1011.0352 [physics.ins-det].

[13] Belle II. *Super KEKB and Belle II* [online]. [cit. 22/04/21]. https://www.belle2.org/project/super_kekb_and_belle_ii.

[14] Brodzicka, Jolanta, et al. *Physics achievements from the Belle experiment.* https://doi.org/10.1093/ptep/pts072.

[15] Akai, Kazunori, Furukawa, Kazuro, Koiso, Haruyo *SuperKEKB Collider.* arXiv:1809.01958 [physics.ins-det].

[16] High Energy Accelerator Research Organization (KEK). *SuperKEKB collider achieves the world's highest luminosity* [online]. [cit. 26/04/21]. https://www.kek.jp/en/newsroom/2020/06/26/1400/.

[17] Kou, E., Urquijo, P. *The Belle II Physics Book*. arXiv:1808.10567 [physics.ins-det].

[18] Joint Institute for Nuclear Research (JINR). *Electrons and Positrons Collide for the first time in the SuperKEKB Accelerator* [online]. [cit. 22/04/21]. http://www.jinr.ru/posts/electrons-and-positrons-collide-for-the-first-time-in-the-superkekb-accelerator/.

[19] Lippmann, Christian. *Particle Identification*. arXiv:1101.3276 [hep-ex].

[20] Yoshihito, I. et al. *Level 1 trigger system for the Belle II experiment*. IEEE Transactions on Nuclear Science, vol. 58, no. 4, doi: 10.1109/TNS.2011.2119329.

[21] Lee, S. et al. *Particle Identification*. 2011 J. Phys.: Conf. Ser. 331 022015.

[22] The Belle II Collaboration. *Belle II Luminosity*. https://confluence.desy.de/display/BI/Belle+II+Luminosity.

[23] The Geant4 collaboration. Geant4 – *a simulation toolkit*. https://inspirehep.net/files/6c9c0b62bbc8dc0401fca11a5fe5c87c.

[24] Kuhr, T., Ritter, M., Hauth, T., Braun, N. *The Belle II Core Software*. https://link.springer.com/content/pdf/10.1007/s41781-018-0017-9.pdf.

[25] The ROOT Team. *ROOT - Data Analysis Framework*. (official website). https://root.cern.

[26] Verkerke, W., Kirkby, D. *RooFit Users Manual v2.91*. https://root.cern.ch/download/doc/RooFit_Users_Manual_2.91-33.pdf.

[27] Barlow, Roger. *Extended maximum likelihood*. Nucl. Instr. and Methods in Phys. Res. Sec. A, vol. 297, issue 3 (1990).

[28] Bevan, Adrian, Wilson, Fergus. *AFit User Guide*. http://pprc.qmul.ac.uk/~bevan/afit/afit.pdf.

[29] The Belle II Collaboration. *Measurement of the integrated luminosity of the Phase 2 data of the Belle II experiment.* arXiv:1910.05365.

[30] The Belle II Collaboration. *Muon and electron identification efficiencies and hadron-lepton mis-identification rates at Belle II for Moriond 2021.* BELLE2-CONF-PH-2021-002.

[31] The Belle II Collaboration. *Measurement of the tracking efficiency and fake rate with $e^+e^- \to \tau^+\tau^-$ events.* BELLE2-NOTE-PL-2020-014.

List of Figures

List of Tables

A. References

A.1 BaBar study

The use of a double ratio method was inspired by a study on the π^0 efficiency correction which was done by the BaBar collaboration. The most important aspects of the analysis are summarized below, the original description can be found in [3].

In the BaBar study they used the following formula for the efficiency correction,

$$\eta_{\pi^0} = \frac{N^{data}(\tau \to t\pi^0\nu_\tau)}{N^{MC}(\tau \to t\pi^0\nu_\tau)} \div \frac{N^{data}(\tau \to t\nu_\tau)}{N^{MC}(\tau \to t\nu_\tau)}, \tag{A.1}$$

where t denotes a charged particle that fails the identification criteria for an electron. The study was done with 1x1-prong τ-pair events, with the tag τ lepton reconstructed $\tau \to e\nu_\tau\bar{\nu}_e$ decay mode. The $\tau \to t\pi^0\nu_\tau$ and $\tau \to t\nu_\tau$ event samples were selected with a purity of about 94 % and about 95 %, respectively, where $t = \pi, \mu, K$.

The π^0s are reconstructed from photon candidate pairs. Apart from π^0 decays themselves, photons can be produced via bremsstrahlung of charged particles. ECL energy clusters mimicking photons can also come from neutral hadrons. Showers in the electromagnetic calorimeter initiated by hadrons can contain neutral particles, such as neutrons or K^0 mesons, which can travel larger distances in the crystals before possibly producing a new shower. These so-called split-offs may be subsequently reconstructed as extra photon candidates near. The BaBar study states that the simulation underestimates the number of split-offs found in data, and that a correction for this effect was applied.

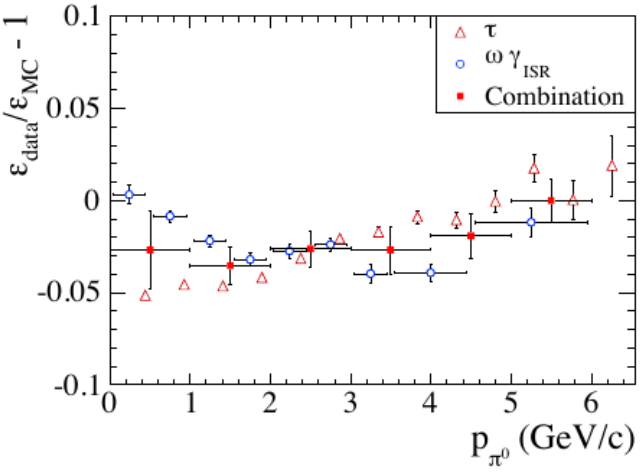

Figure A.1: *Momentum dependent efficiency correction.* The plot shows the $\eta_{\pi^0} - 1$ quantity as a function of π^0 momentum. The red triangles represent the results obtained from the study with τ leptons. Shown uncertainties are statistical only. [3]

The momentum-averaged π^0 reconstruction efficiency correction for BaBar was

$0.960 \pm 0.001(stat) \pm 0.008(syst)$. The main sources of systematic uncertainty were the τ branching fractions and the split-off correction, neither of which can cancel in the double ratio.

For use in other analyses, where the momentum spectrum of the π^0s is different than in τ events, the π^0 efficiency correction was also measured as a function of the π^0 momentum. The momentum-dependent weights are shown as the red triangles in Fig. A.1. The BABAR results show non-negligible momentum dependence of the π^0 efficiency correction measured in τ decays.

A.2 Recommended π^0 selections

The "Eff60", "Eff50", "Eff40", "Eff30", "Eff20", "Eff10" π^0 selections were developed by T. Koga, A. Selce and S. Stengel and their study is summarized in an internal Belle II note *Optimization of π^0 reconstruction selection and first systematic uncertainty evaluation of the efficiencies*. These selections were optimized for π^0s coming from B meson decays and they differ by the overall reconstruction efficiency which is 60 % for "Eff60", 50 % for "Eff50" etc.

As a reference for this τ analysis, the recommended π^0 selection cuts are summarized in Tab. A.1.

The selections use different photon energy cuts depending on the ECL region where the energy cluster was detected - forward endcap (FWD), barrel section (BRL) or backward endcap (BWD).

The $E1E9$ variable returns ratio of energies of the central crystal of the ECL energy cluster, $E1$, and 3x3 crystals, $E9$, around the central crystal. Since $E1 \leq E9$, the ratio $E1/E9 \leq 1$ and tends towards larger values for photons and smaller values for hadrons.

The φ difference is the difference in φ angles between the two photons, while the 3D angle difference returns the angle between the two photons in 3D space.

Table A.1: Recommended π^0 selections derived from B decays.

	"Eff60"	**"Eff50"**	**"Eff40"**
E_γ [MeV] (FWD)	> 22.5	> 25	> 80
E_γ [MeV] (BRL)	> 20.0	> 25	> 30
E_γ [MeV] (BWD)	> 20.0	> 40	> 60
θ	[0.2967, 2.6180]	[0.2967, 2.6180]	[0.2967, 2.6180]
clusterNHits	> 1.5	> 1.5	> 1.5
$M_{\gamma\gamma}$ [MeV]	> 30	[105,150]	[120,145]

	"Eff30"	**"Eff20"**	**"Eff10"**
E_γ [MeV] (FWD)	> 80	> 120	> 200
E_γ [MeV] (BRL)	> 30	> 30	> 100
E_γ [MeV] (BWD)	> 80	> 80	> 180
θ	[0.2967, 2.6180]	[0.2967, 2.6180]	[0.2967, 2.6180]
clusterNHits	> 1.5	> 1.5	> 1.5
$M_{\gamma\gamma}$ [MeV]	[120,145]	[121,142]	[127,139]
φ difference	< 1.5	< 1.0	< 0.9
3D angle difference	< 1.5	< 0.9	< 0.8

Tab. A.2 lists the efficiencies and purities of the π^0 selections described above.

Table A.2: Purity and efficiency of the recommended π^0 selections.

	"Eff60"	"Eff50"	"Eff40"	"Eff30"	"Eff20"	"Eff10"
efficiency (%)	59.82	49.82	39.93	29.84	19.81	9.81
purity (%)	2.49	10.87	18.82	29.78	50.03	69.25

The note also list the measured π^0 reconstruction efficiency corrections for "Eff50", "Eff40", "Eff30", "Eff20", "Eff10" π^0 selections, these results are summarized in Attachment A.3.

A.3 The π^0 reconstruction efficiency study with B decays

A similar measurement of the π^0 reconstruction efficiency correction was performed by T. Koga, A. Selce and S. Stengel. Their study is summarized in an internal Belle II note *Optimization of π^0 reconstruction selection and first systematic uncertainty evaluation of the efficiencies* in which the recommended π^0 selections "Eff60", "Eff50", "Eff40", "Eff30", "Eff20" and "Eff10" were also presented (see Attachment A.2).

The π^0 reconstruction efficiency correction was measured using $\eta \to 3\pi^0$ and $\eta \to \gamma\gamma$ decays where the η mesons are produced in B-meson decays. Assuming $\epsilon_{data}(\pi^0 \to \gamma\gamma)/\epsilon_{MC}(\pi^0 \to \gamma\gamma) = \epsilon_{data}(\eta \to \gamma\gamma)/\epsilon_{MC}(\eta \to \gamma\gamma)$, the π^0 efficiency correction is extracted as follows:

$$\begin{aligned} \frac{\epsilon_{\text{Data}}(2\pi^0)}{\epsilon_{\text{MC}}(2\pi^0)} &= \frac{N_{\text{Data}}(\eta \to 3\pi^0)/N_{\text{MC}}(\eta \to 3\pi^0)}{N_{\text{Data}}(\eta \to \gamma\gamma)/N_{\text{MC}}(\eta \to \gamma\gamma)} \\ \frac{\epsilon_{\text{Data}}(\pi^0)}{\epsilon_{\text{MC}}(\pi^0)} &= \sqrt{\frac{\epsilon_{\text{Data}}(2\pi^0)}{\epsilon_{\text{MC}}(2\pi^0)}} \end{aligned} \tag{A.2}$$

The used data sample was Exp7 and Exp8 (5.023 fb^{-1}), the MC sample was MC12 produced with software release-03-02-04.

The π^0 efficiecny correction was measured for "Eff50", "Eff40", "Eff30", "Eff20" and "Eff10" π^0 selections:

$$\begin{aligned} \text{eff50}: &\frac{\epsilon_{\text{Data}}(\pi^0)}{\epsilon_{\text{MC}}(\pi^0)} = 0.945 \pm 0.004(\text{stat.}) \pm 0.071(\text{syst.}) \\ \text{eff40}: &\frac{\epsilon_{\text{Data}}(\pi^0)}{\epsilon_{\text{MC}}(\pi^0)} = 0.945 \pm 0.004(\text{stat.}) \pm 0.041(\text{syst.}) \\ \text{eff30}: &\frac{\epsilon_{\text{Data}}(\pi^0)}{\epsilon_{\text{MC}}(\pi^0)} = 0.932 \pm 0.005(\text{stat.}) \pm 0.034(\text{syst.}) \\ \text{eff20}: &\frac{\epsilon_{\text{Data}}(\pi^0)}{\epsilon_{\text{MC}}(\pi^0)} = 0.925 \pm 0.006(\text{stat.}) \pm 0.045(\text{syst.}) \\ \text{eff10}: &\frac{\epsilon_{\text{Data}}(\pi^0)}{\epsilon_{\text{MC}}(\pi^0)} = 0.903 \pm 0.013(\text{stat.}) \pm 0.062(\text{syst.}) \end{aligned} \tag{A.3}$$

A.4 Momentum dependent π^0 reconstruction efficiency measurement with B decays

This section gives a brief summary of an internal Belle II note *Measurement of momentum dependent π^0 reconstruction efficiency with D decays* by Taichiro Koga, focusing on the results which are relevant to our τ lepton study.

In this π^0 reconstruction study, the correction was measured using two methods, either from D^0 decays $D^0 \to K^-\pi^+\pi^0$ and $D^0 \to K^-\pi^+$ or using charged B-meson decay $B^+ \to \pi^+ D^{*0}(D^{*0} \to \pi^0 D^0, D^0 \to K^-\pi^+)$.

The π^0 momentum dependence was measured in eight momentum bins: [0.2, 0.4, 0.6, 0.8, 1.0, 1.5, 2.0, 3.0] GeV.

The first measurement uses D-meson decays for the π^0 momentum of [0.2,3.0] GeV:

$$\begin{aligned}
&\frac{N_{\rm Data}(D^0 \to K^-\pi^+\pi^0)/N_{\rm MC}(D^0 \to K^-\pi^+\pi^0)}{N_{\rm Data}(D^0 \to K^-\pi^+)/N_{\rm MC}(D^0 \to K^-\pi^+)} \\
&= \frac{\mathrm{BR}_{\rm Data}(\mathrm{D}^0 \to \mathrm{K}^-\pi^+\pi^0)/\mathrm{BR}_{\rm MC}(\mathrm{D}^0 \to \mathrm{K}^-\pi^+\pi^0)}{\mathrm{BR}_{\rm Data}(\mathrm{D}^0 \to \mathrm{K}^-\pi^+)/\mathrm{BR}_{\rm MC}(\mathrm{D}^0 \to \mathrm{K}^-\pi^+)} \\
&\quad \times \frac{\epsilon_{\rm Data}(K^-,\pi^+)_{D^0\to K^-\pi^+\pi^0}/\epsilon_{\rm MC}(K^-,\pi^+)_{D^0\to K^-\pi^+\pi^0}}{\epsilon_{\rm Data}(K^-,\pi^+)_{D^0\to K^-\pi^+}/\epsilon_{\rm MC}(K^-,\pi^+)_{D^0\to K^-\pi^+}} \times \frac{\epsilon_{\rm Data}(\pi^0)}{\epsilon_{\rm MC}(\pi^0)} \\
&\simeq \frac{\epsilon_{\rm Data}(\pi^0)}{\epsilon_{\rm MC}(\pi^0)}
\end{aligned} \tag{A.4}$$

The efficiency for π^0s in [0.05,0.2] GeV momentum range was measured using the B-meson decays. The relative efficiency of the π^0 in [0.05,0.2] GeV respect to [0.2,0.4] GeV is extracted as follows

$$\begin{aligned}
&\frac{N_{\rm Data}(B^+ \to \pi^+ D^{*0})_{p_{\pi^0}=[0.05,0.2]\ \rm GeV}/N_{\rm MC}(B^+ \to \pi^+ D^{*0})_{p_{\pi^0}=[0.05,0.2]\ \rm GeV}}{N_{\rm Data}(B^+ \to \pi^+ D^{*0})_{p_{\pi^0}=[0.2,0.4]\ \rm GeV}/N_{\rm MC}(B^+ \to \pi^+ D^{*0})_{p_{\pi^0}=[0.2,0.4]\ \rm GeV}} \\
&= \frac{\mathrm{BR}_{\rm Data}(\mathrm{B}^+ \to \pi^+\mathrm{D}^{*0})_{\mathrm{p}_{\pi^0}=[0.05,0.2]\ \rm GeV}/\mathrm{BR}_{\rm MC}(\mathrm{B}^+ \to \pi^+\mathrm{D}^{*0})_{\mathrm{p}_{\pi^0}=[0.05,0.2]\ \rm GeV}}{\mathrm{BR}_{\rm Data}(\mathrm{B}^+ \to \pi^+\mathrm{D}^{*0})_{\mathrm{p}_{\pi^0}=[0.2,0.4]\ \rm GeV}/\mathrm{BR}_{\rm MC}(\mathrm{B}^+ \to \pi^+\mathrm{D}^{*0})_{\mathrm{p}_{\pi^0}=[0.2,0.4]\ \rm GeV}} \\
&\quad \times \frac{\epsilon_{\rm Data}(K^-,\pi^+)_{p_{\pi^0}=[0.05,0.2]\ \rm GeV}/\epsilon_{\rm MC}(K^-,\pi^+)_{p_{\pi^0}=[0.05,0.2]\ \rm GeV}}{\epsilon_{\rm Data}(K^-,\pi^+)_{p_{\pi^0}=[0.2,0.4]\ \rm GeV}/\epsilon_{\rm MC}(K^-,\pi^+)_{p_{\pi^0}=[0.2,0.4]\ \rm GeV}} \\
&\quad \times \frac{\epsilon_{\rm Data}(\pi^0)_{p_{\pi^0}=[0.05,0.2]\ \rm GeV}/\epsilon_{\rm MC}(\pi^0)_{p_{\pi^0}=[0.05,0.2]\ \rm GeV}}{\epsilon_{\rm Data}(\pi^0)_{p_{\pi^0}=[0.2,0.4]\ \rm GeV}/\epsilon_{\rm MC}(\pi^0)_{p_{\pi^0}=[0.2,0.4]\ \rm GeV}} \\
&\simeq \frac{\epsilon_{\rm Data}(\pi^0)_{p_{\pi^0}=[0.05,0.2]\ \rm GeV}/\epsilon_{\rm MC}(\pi^0)_{p_{\pi^0}=[0.05,0.2]\ \rm GeV}}{\epsilon_{\rm Data}(\pi^0)_{p_{\pi^0}=[0.2,0.4]\ \rm GeV}/\epsilon_{\rm MC}(\pi^0)_{p_{\pi^0}=[0.2,0.4]\ \rm GeV}}
\end{aligned} \tag{A.5}$$

By combining the Eq. A.4 and Eq. A.5, the π^0 efficiency correction for the momentum range of [0.05,0.2] GeV can be determined as

$$\frac{\epsilon_{\text{Data}}(\pi^0)_{p_{\pi^0}=[0.05,0.2]\ \text{GeV}}}{\epsilon_{\text{MC}}(\pi^0)_{p_{\pi^0}=[0.05,0.2]\ \text{GeV}}}$$
$$= \frac{\epsilon_{\text{Data}}(\pi^0)_{p_{\pi^0}=[0.05,0.2]\ \text{GeV}}/\epsilon_{\text{MC}}(\pi^0)_{p_{\pi^0}=[0.05,0.2]\ \text{GeV}}}{\epsilon_{\text{Data}}(\pi^0)_{p_{\pi^0}=[0.2,0.4]\ \text{GeV}}/\epsilon_{\text{MC}}(\pi^0)_{p_{\pi^0}=[0.2,0.4]\ \text{GeV}}} \times \frac{\epsilon_{\text{Data}}(\pi^0)_{p_{\pi^0}=[0.2,0.4]\ \text{GeV}}}{\epsilon_{\text{MC}}(\pi^0)_{p_{\pi^0}=[0.2,0.4]\ \text{GeV}}} \tag{A.6}$$

The used data samples were Exp7, Exp8, Exp10 and buckets 9, 10 and 11 from Exp12 (34.5 fb^{-1} in total). The used MC samples were MC13 produced with release-04-02-08.

The result for the "Eff50" π^0 selection is shown in Fig. A.2.

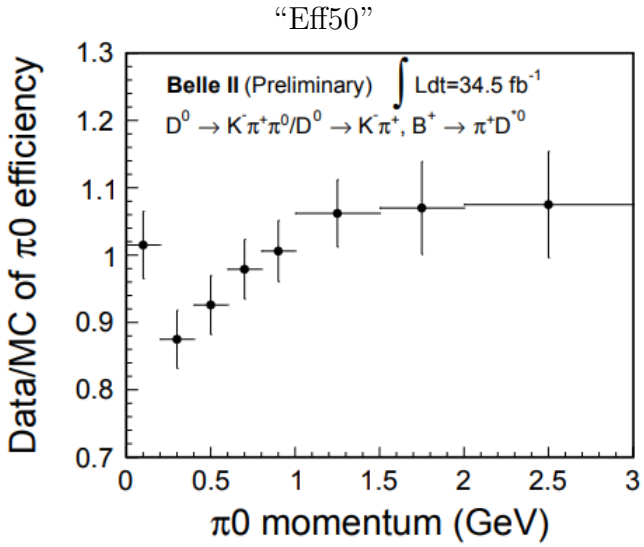

Figure A.2: *Momentum dependent efficiency correction from B decays.* This plot shows the π^0 efficiency correction as a function of the π^0 momentum. The measurement in the first momentum bin was done using the B-decays method, in the rest of the bins the D-decays method was used. For this measurement with B decays, the π^0 selection "Eff50" was used, see Attachment A.2.

B. Additional material

B.1 Various fit functions

Apart from the double Gaussian and CB function we tried several other model functions for the signal peak of $M_{\gamma\gamma}$. The definition of the used functions can be found in [28].

- Gaussian (Fig. B.1) – not able to model properly the shoulders of the signal peak.
- CB (Fig. B.2) – slightly larger χ^2 than double Gaussian, and sometimes struggles to accurately capture either of the peak shoulders.
- CB + CB (Fig. B.2) – unstable behaviour, CB functions may extend to the tails of the $M_{\gamma\gamma}$ distributions which leads to an overestimation of the signal yield.
- double-sided CB (Fig. B.2) – unstable behaviour, inaccurate description of the shape (large χ^2), possible overestimation of signal.
- Gaussian + CB (Fig. B.3) – unstable behaviour, possible overestimation of the signal.
- Gaussian + Breit-Wigner distribution (BW) (Fig. B.3) – possible overestimation of the signal.
- Gaussian + Landau distribution (Fig. B.3) – unstable behaviour, larger χ^2.

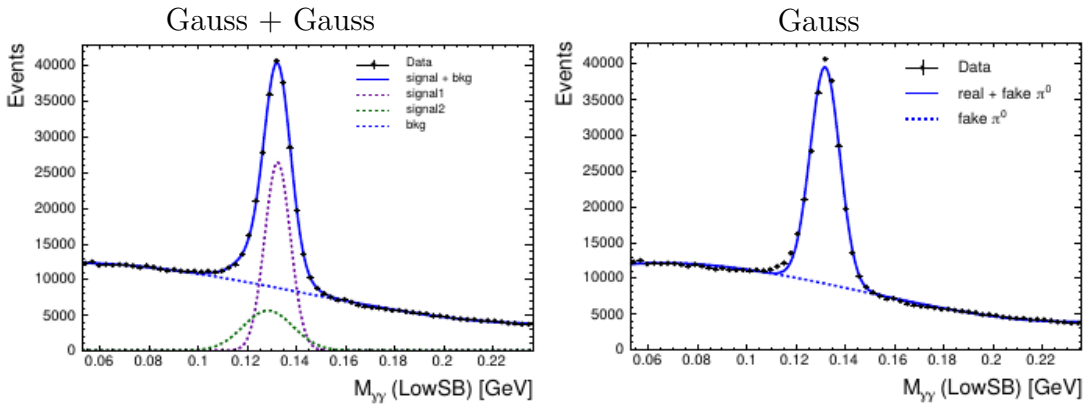

Figure B.1: *Single Gaussian.* Comparison of double Gaussian peak fit with a single Gaussian.

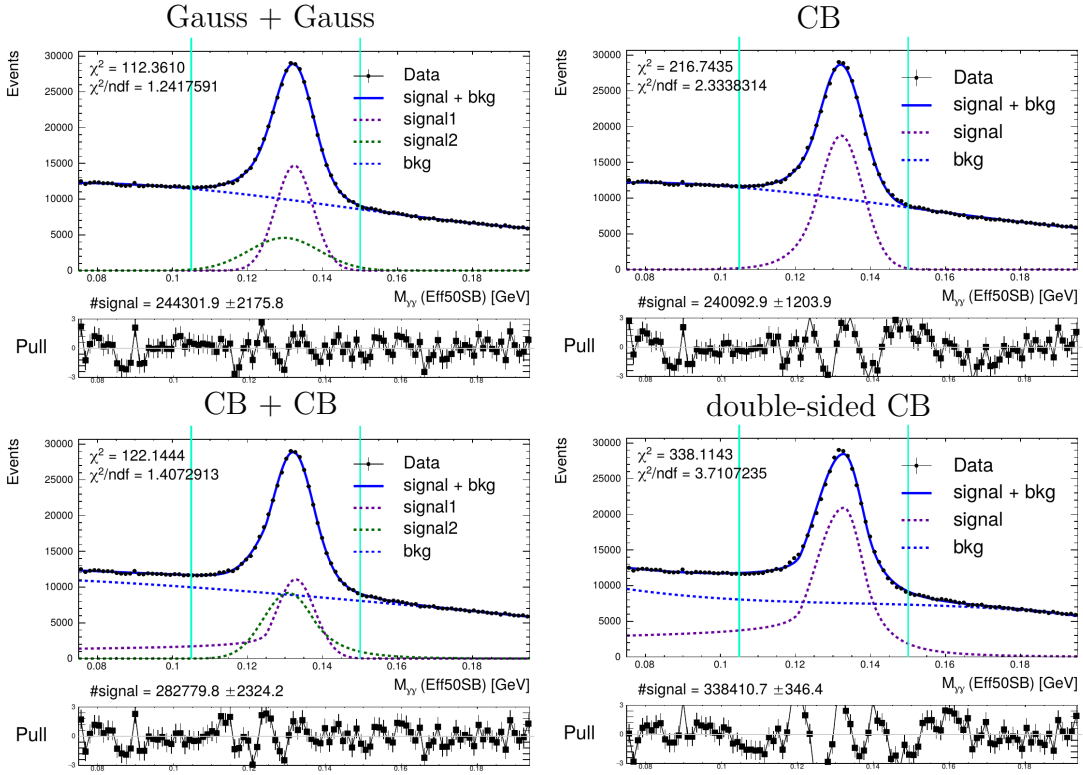

Figure B.2: *Different CB fits.* Comparison of double Gaussian peak fit with a single CB, CB + CB and double-sided CB.

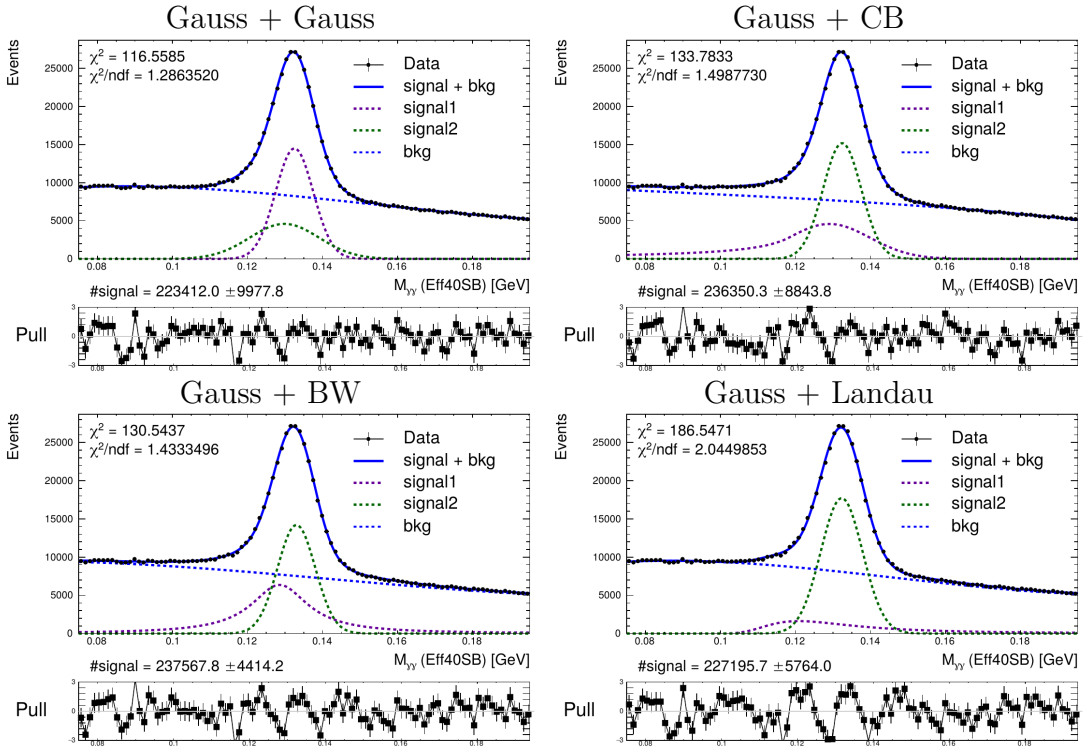

Figure B.3: *Combinations with Gaussian.* Comparison of double Gaussian peak fit and a Gaussian combined with CB, BW or Landau distribution.

B.2 $M_{\gamma\gamma}$ CB fits

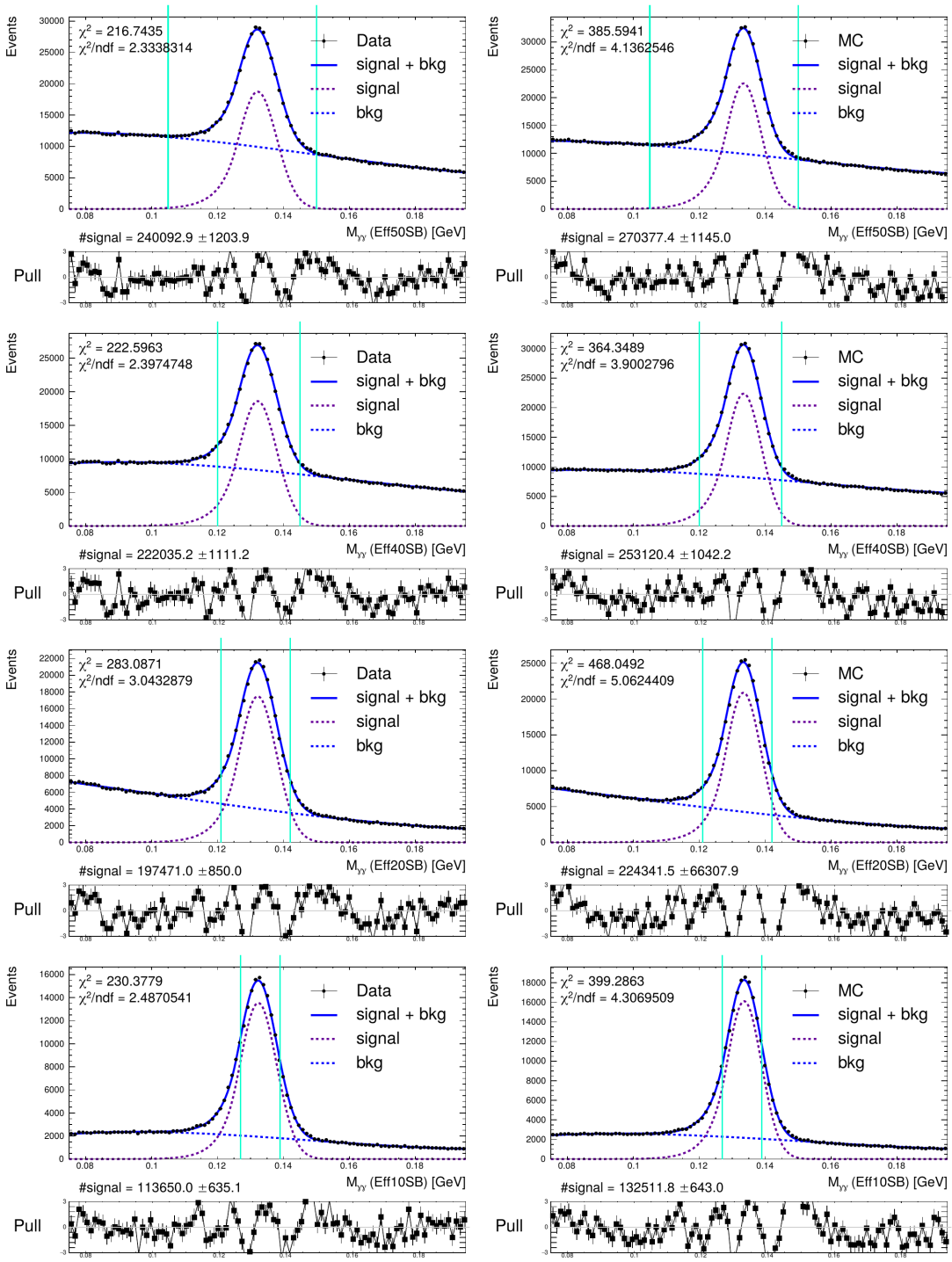

Figure B.4: *$M_{\gamma\gamma}$ CB fits (completion).* The plots show examples of the CB fits of the π^0 mass distributions in data and MC for "Eff50SB", "Eff40SB", "Eff20SB" and "Eff10SB" π^0 types.

B.3 π^0 multiplicity plots

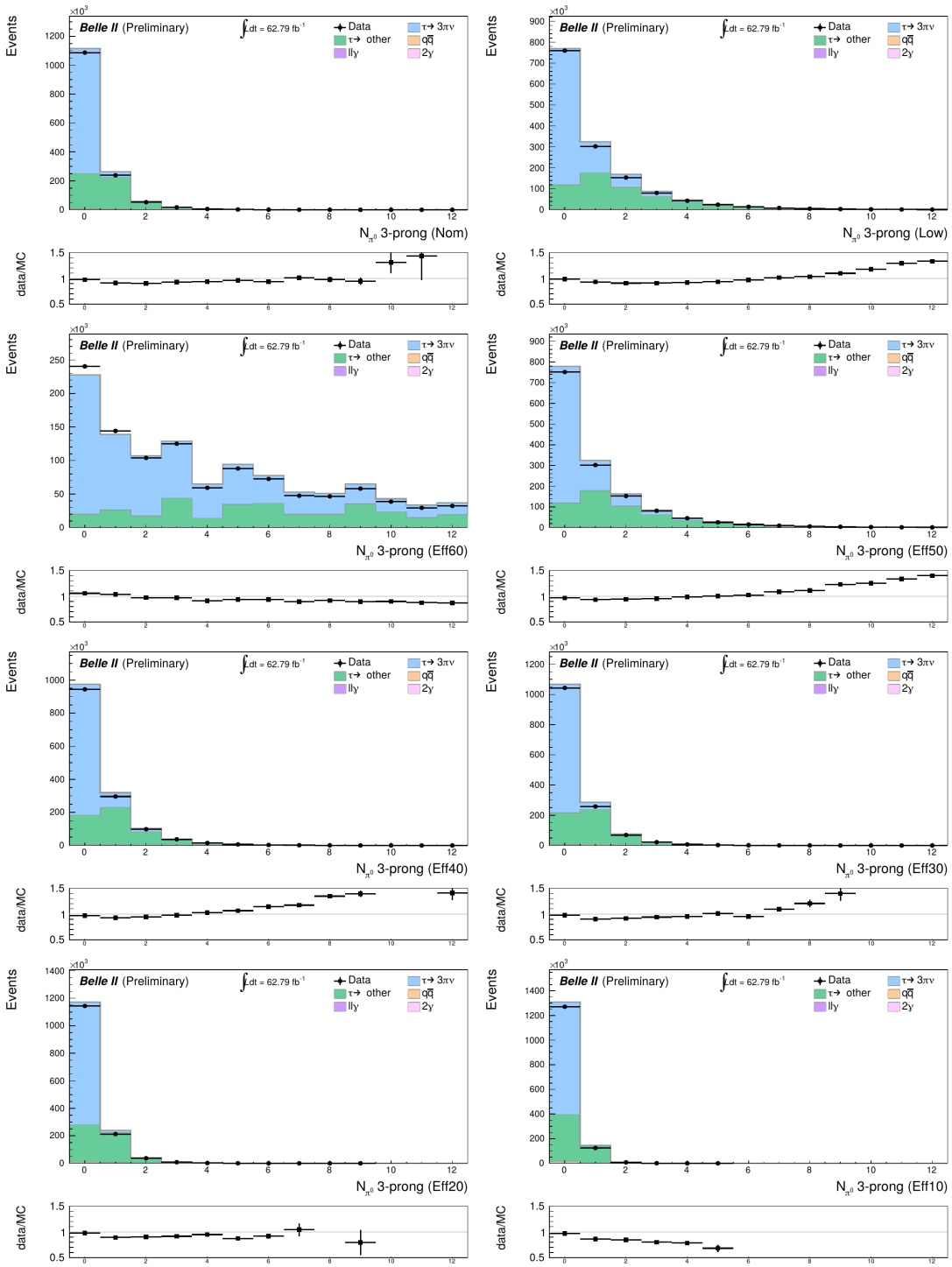

Figure B.5: π^0 *multiplicity.* The plots show number of π^0s on the 3-prong side for all of the considered π^0 selections. The "$\tau\tau$ (real)" MC components in these plots mark the truth-matched $\tau \to 3\pi\nu$ decay mode, "$\tau\tau$ (fake)" component comprises all other τ decays.

B.4 $M_{\gamma\gamma}$ fits in different momentum bins

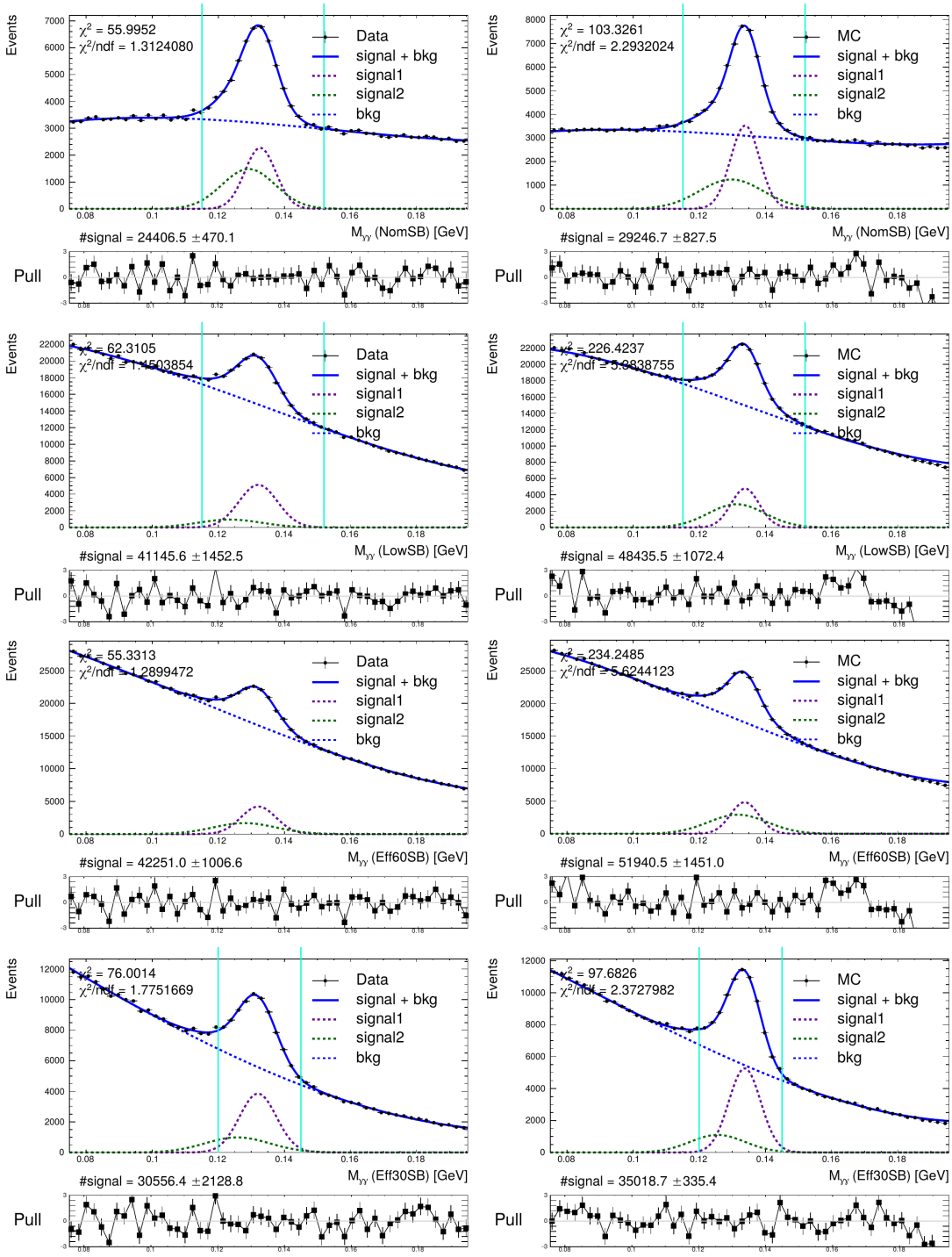

Figure B.6: *$M_{\gamma\gamma}$ fits in momentum bin p_1 (examples).* $M_{\gamma\gamma}$ distribution fits of data and MC are shown for π^0 selections "NomSB", "LowSB", "Eff60SB" and "Eff30SB".

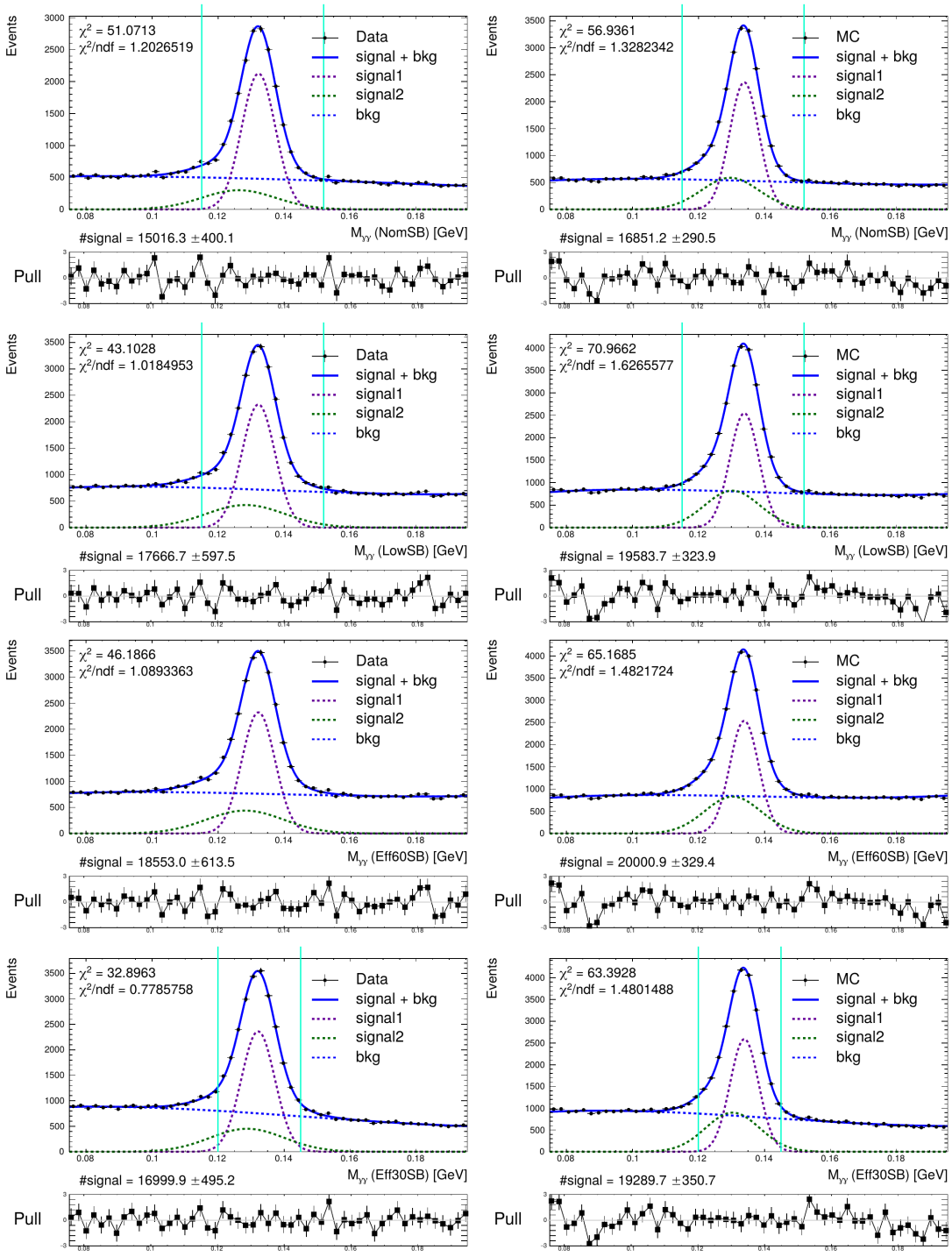

Figure B.7: *$M_{\gamma\gamma}$ fits in momentum bin p_2 (examples).* $M_{\gamma\gamma}$ distribution fits of data and MC are shown for π^0 selections "NomSB", "LowSB", "Eff60SB" and "Eff30SB".

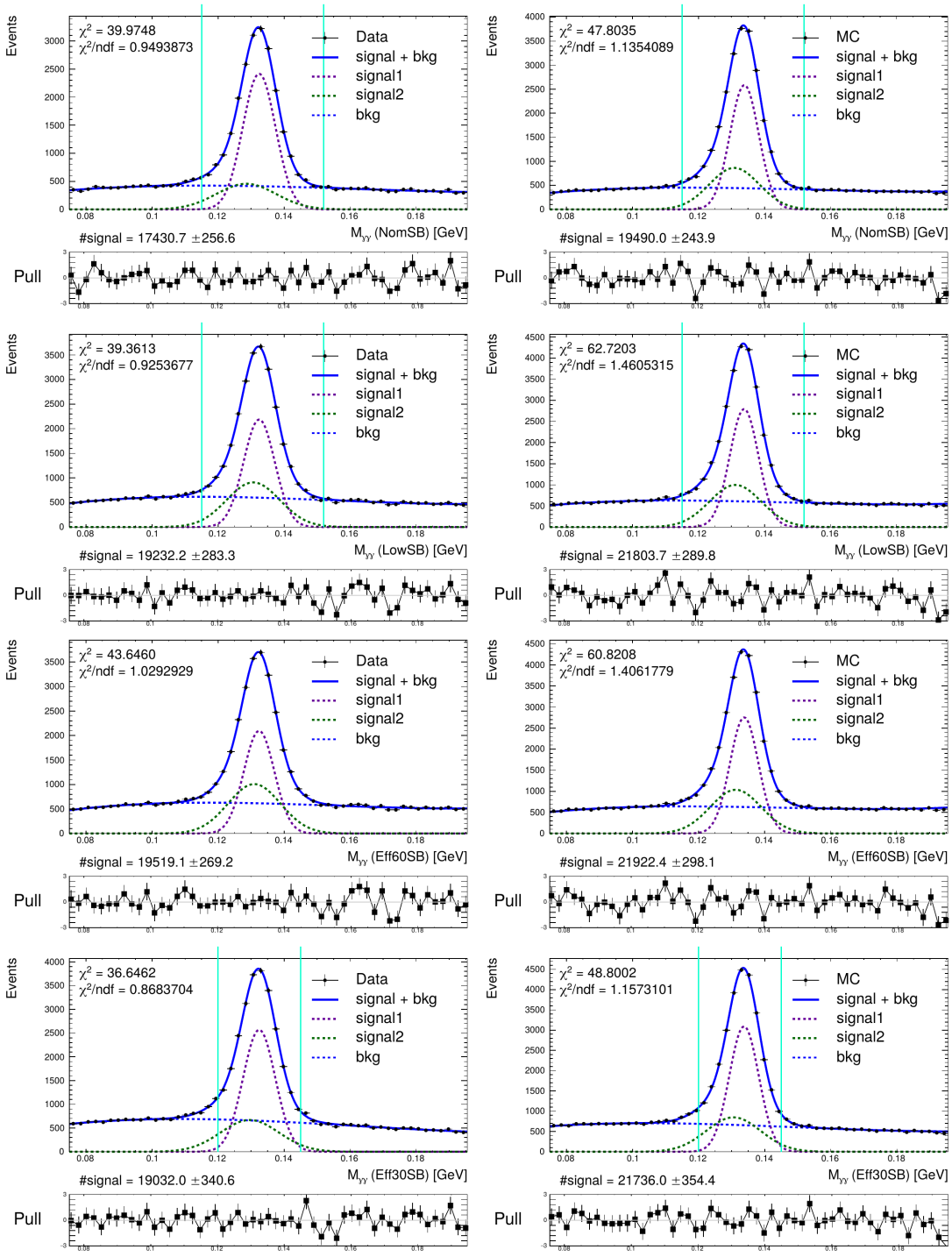

Figure B.8: *$M_{\gamma\gamma}$ fits in momentum bin p_4 (examples).* $M_{\gamma\gamma}$ distribution fits of data and MC are shown for π^0 selections "NomSB", "LowSB", "Eff60SB" and "Eff30SB".

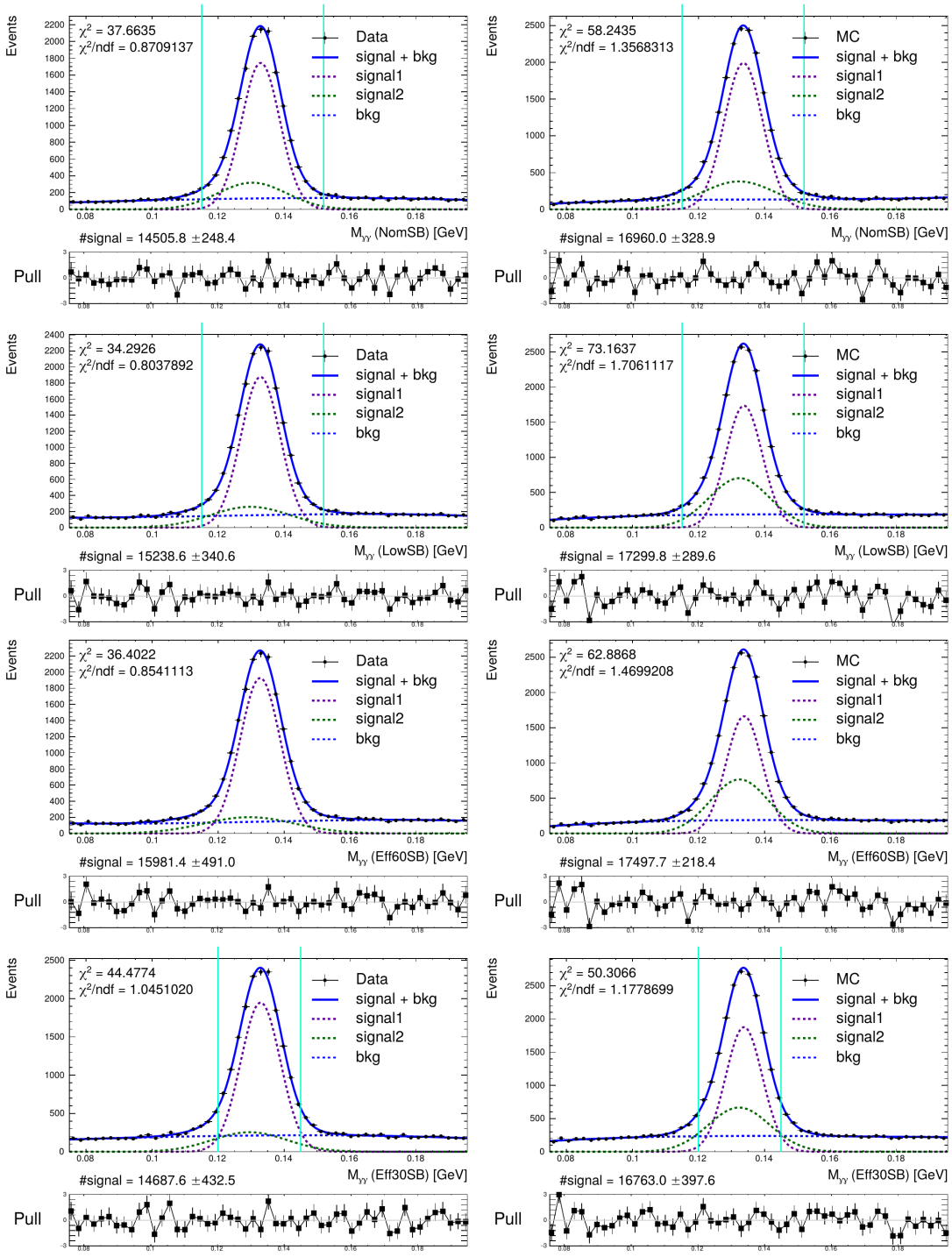

Figure B.9: *$M_{\gamma\gamma}$ fits in momentum bin p_{11} (examples).* $M_{\gamma\gamma}$ distribution fits of data and MC are shown for π^0 selections "NomSB", "LowSB", "Eff60SB" and "Eff30SB".

B.5 $M_{\gamma\gamma}$ fits for photon timing study

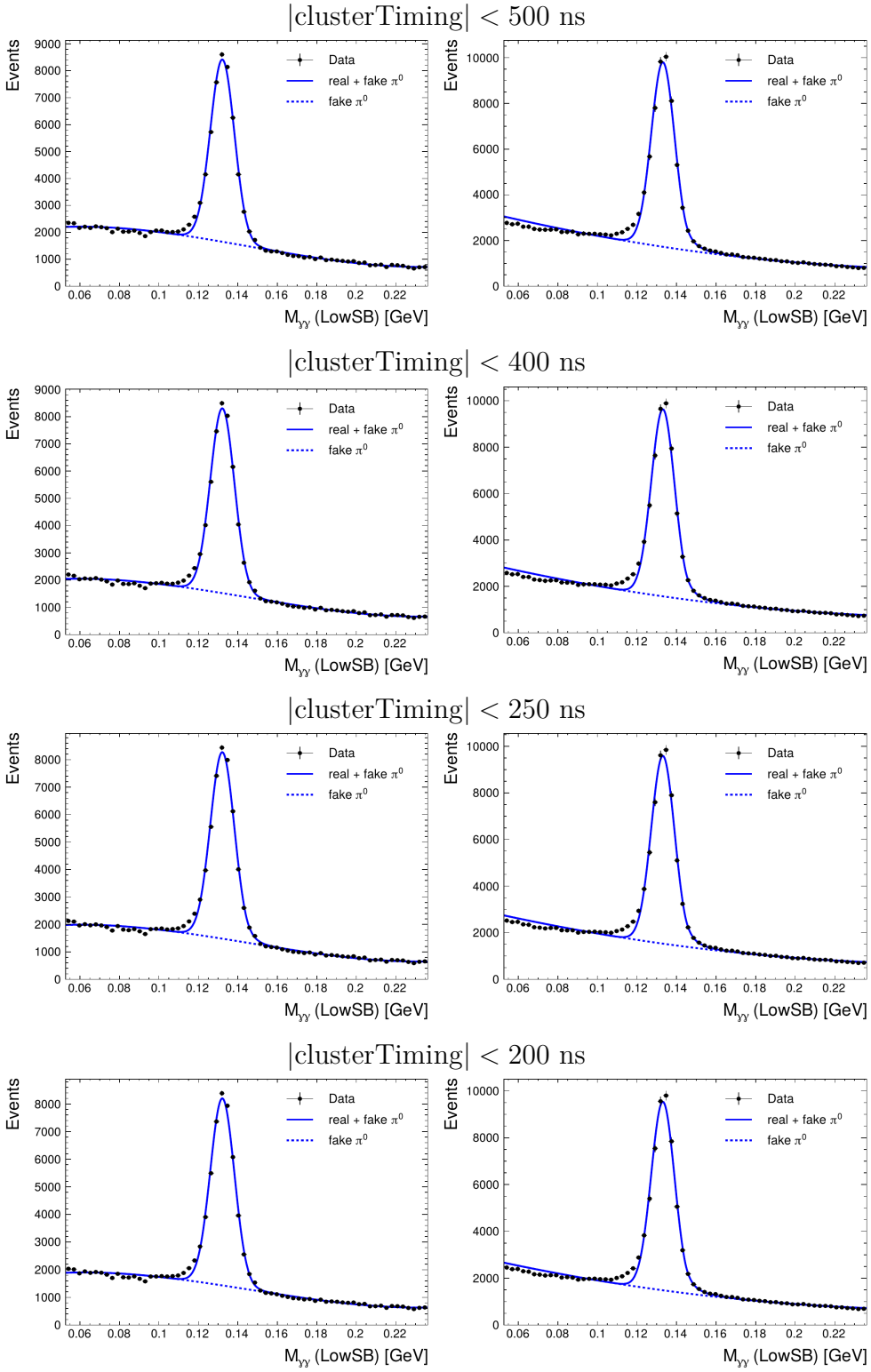

Figure B.10: *$M_{\gamma\gamma}$ fits after timing selection (examples i).* $M_{\gamma\gamma}$ distribution fits of data and MC are shown for "LowSB" π^0 selections after applying selections $|\text{clusterTiming}| < \{500, 300, 250, 200\}$ ns.

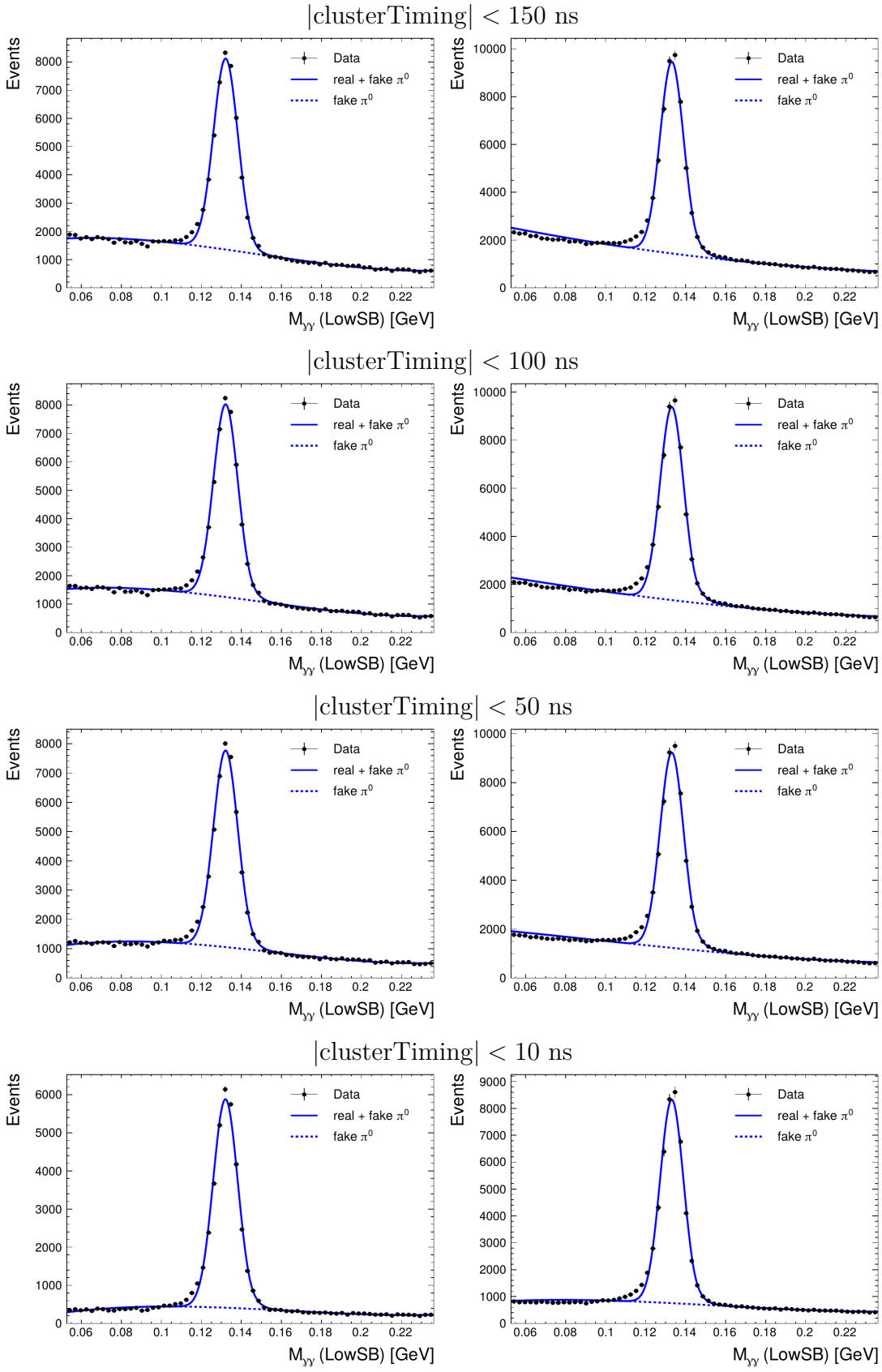

Figure B.11: *$M_{\gamma\gamma}$ fits after timing selection (examples ii).* $M_{\gamma\gamma}$ distribution fits of data and MC are shown for "LowSB" π^0 selections after applying selections $|\text{clusterTiming}| < \{150, 100, 50, 10\}$ ns.

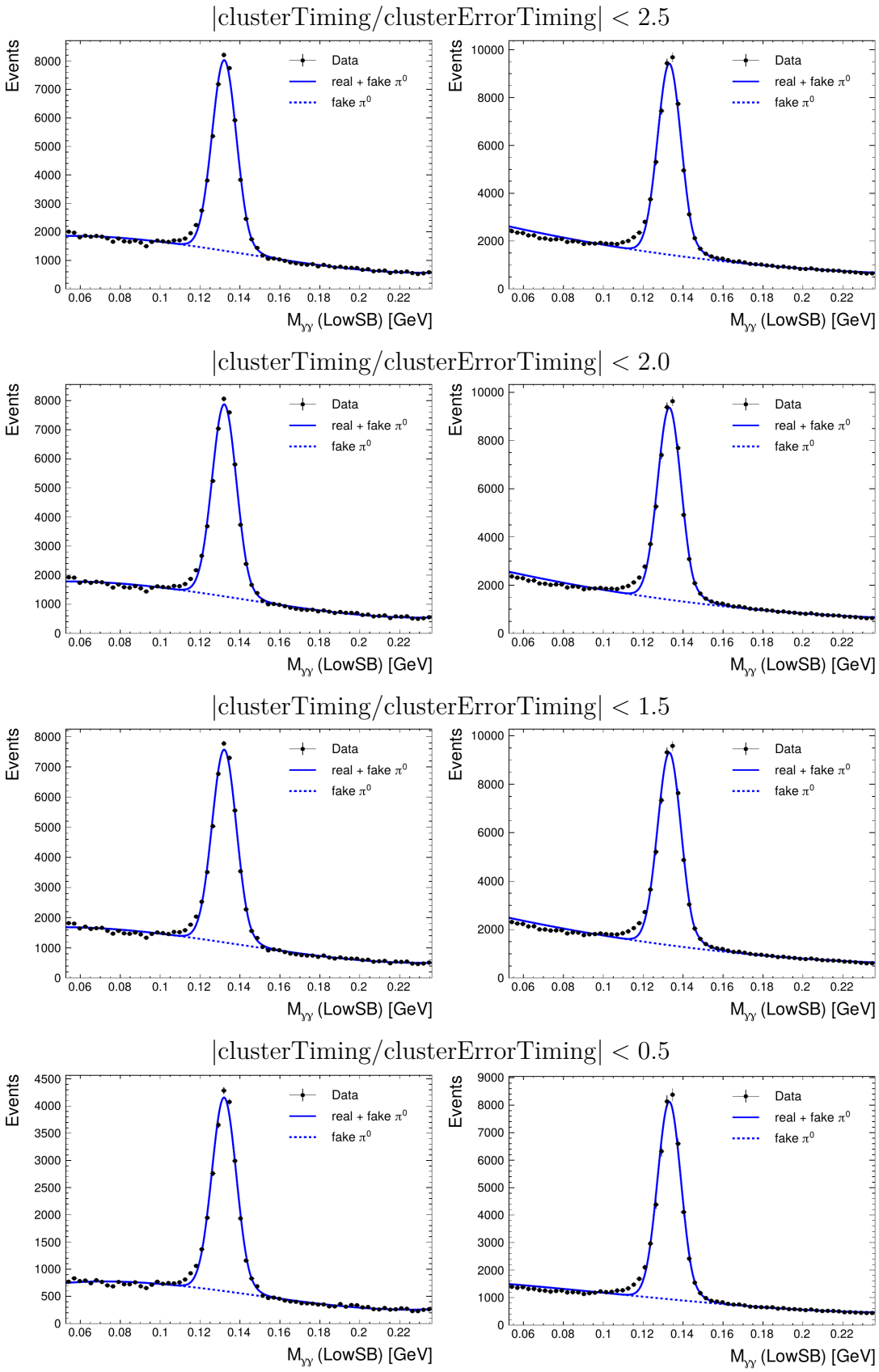

Figure B.12: *$M_{\gamma\gamma}$ fits after timing ratio selection (examples).* $M_{\gamma\gamma}$ distribution fits of data and MC are shown for "LowSB" π^0 selections after applying selections $|\text{clusterTiming/clusterErrorTiming}| < \{2.5, 2.0, 1.5, 0.5\}$.